論文 / 著書情報
Article / Book Information

題目(和文)	
Title(English)	Study of Se-free Cu(In,Ga)S2 Solar Cells with KCN-free Process
著者(和文)	廣井誉
Author(English)	Homare Hiroi
出典(和文)	学位:博士(工学), 学位授与機関:東京工業大学, 報告番号:甲第10641号, 授与年月日:2017年9月20日, 学位の種別:課程博士, 審査員:山田 明,中川 茂樹,間中 孝彰,宮島 晋介,PHAM NAM HAI
Citation(English)	Degree:Doctor (Engineering), Conferring organization: Tokyo Institute of Technology, Report number:甲第10641号, Conferred date:2017/9/20, Degree Type:Course doctor, Examiner:,,,,
学位種別(和文)	博士論文
Type(English)	Doctoral Thesis

DOCTORAL THESIS

Study of Se-free Cu(In,Ga)S_2 Solar Cells with KCN-free Process

Presented by Homare Hiroi

Department of Physical Electronics

Tokyo Institute of Technology

Supervisor: Prof. Akira Yamada

2017

Contents

1 Introduction 5

1.1 World energy consumption 5

1.2 Environmental issues 9

1.3 Renewable energy 10

1.4 Current status of photovoltaics 11

1.5 Roadmap “NEDO PV Challenges” in Japan 13

1.6 Se-free Cu(In,Ga)S_2 solar cells with KCN-free process 16

1.7 Objective and outline of this thesis 16

References 19

2 Fundamental properties of Se-free Cu(In,Ga)S_2 solar cells 21

2.1 Introduction 21

2.2 Properties of Se-free Cu(In,Ga)S_2 thin-films 22

2.2.1 Crystal structure 22

2.2.2 Phase relations 23

2.2.3 Relation between the lattice constant and the bandgap 25

2.2.4 Absorption coefficient 26

2.2.5 Defect structure 27

2.3 Structure of Se-free Cu(In,Ga)S_2 solar cells 29

2.3.1 Device structure 29

2.3.2 Band structure 31

2.4 Chapter summary 32

References 33

3 Se-free Cu(In,Ga)S_2 absorber layer via KCN-free process 36

3.1 Introduction 36

3.2 Cu-poor composition 37

3.3 Crystal growth 40

3.4 Ga depth profile 42

3.4.1 Ga/(Ga+In) ratio 42

3.4.2 Numerical simulation 44

3.4.3 Effects of Ga grading 46

3.4.4 Optimization of Ga depth profile 52

3.5 Minority carrier lifetime 56

3.6 Chapter summary 57

References 58

4 $Zn_{1-x}Mg_xO$ as a Cd-free buffer layer material 60

4.1 Introduction 60

4.2 CdS buffer layer 61
4.2.1 Chemical bath deposition 61
4.2.2 Dependence of electrical parameters on thickness 62
4.3 $Zn_{1-x}Mg_xO$ buffer layer 67
4.3.1 Atomic layer deposition 67
4.3.2 Effects of a wide bandgap 68
4.3.3 Dependence of electrical parameters on the Mg content 70
4.4 Chapter summary 75
References 76
5 Investigation of the impact of interfaces 77
5.1 Introduction 77
5.2 Interface between back electrode and p-type absorber 78
5.2.1 MoS_2 layer 78
5.2.2 Effect of MoS_2 interlayer 78
5.3 Interface between n-type buffer and front electrode 82
5.3.1 i-ZnO layer 82
5.3.2 Dependence of fill factor on i-ZnO thickness 83
5.4 Chapter summary 85
References 86

6 New world record conversion efficiency 88

6.1 Introduction 88

6.2 Single cell 89

6.2.1 15.5% efficiency cell (certified) 89

6.2.2 16.9% efficiency cell (in-house) 91

6.3 Highest open-circuit voltage 97

6.4 Chapter summary 103

References 104

7 General summary and future prospects 106

7.1 General summary 106

7.2 Future prospects 108

References 114

Appendix (Single-junction solar cells) 115

Acknowledgements 119

List of publications 121

1

Introduction

Currently, the global energy landscape is significantly changing. Specifically, from the viewpoint of measures to promote a low-carbon society, the research and development (R&D) of renewable energy are being actively pursued by many companies, universities, and institutions all over the world. Many citizens in developed nations live affluent lives and their affluence is increasing from year to year. However, such affluent lifestyle are being supported by the mass consumption of energy. To maintain a high standard of living, we, as a society, must understand the history, current issues, efforts, and future prospects of energy generation and consumption. In this chapter, current issues related to energy are discussed in terms of the evolution of energy consumption to the present point. Furthermore, renewable energy, especially solar energy, is discussed as one of the promising energy resources to resolve current issues and maintain society's high standard of living.

1.1 World energy consumption

The world population has increased every year since 1950, as shown in Fig. 1-1 [1], reaching 7.5 billion in 2017; in addition, the United Nations estimates that the world population will increase to 11.2 billion by 2100 [1,2], which means that world energy consumption will also increase. Figure 1-2(a) shows the transition of primary energy consumption in the world from 1965 to 2015 [3]. The world energy consumption

increased from 3700 million tons of oil equivalent (MTOE) in 1965 to 13,000 MTOE in 2015. As shown in Fig. 1-2(b), such an increase in energy consumption is mainly attributable to countries that are not members of the Organization for Economic Cooperation and Development (OECD). In Fig. 1-2(b), the inversion of MTOE between OECD and non-OECD countries in 2007 is notable. This transition indicates that energy consumption will continue to increase in response to increasing energy demand in non-OECD countries.

The increase in energy consumption due to rapid population growth has raised concerns over the depletion of natural energy resources and global warming in recent years. In particular, consciousness of environment preservation has been heightened and efforts focused on environmental protection are being promoted. The United Nations Climate Change Conference (COP 21) was held in Paris, France from 30 November to 12 December 2015. COP 21 negotiated the “Paris Agreement,” which is a global agreement on the reduction of climate change. This agreement requires all of the participating countries to reduce CO_2 emissions with the goal transitioning to a low-carbon society.

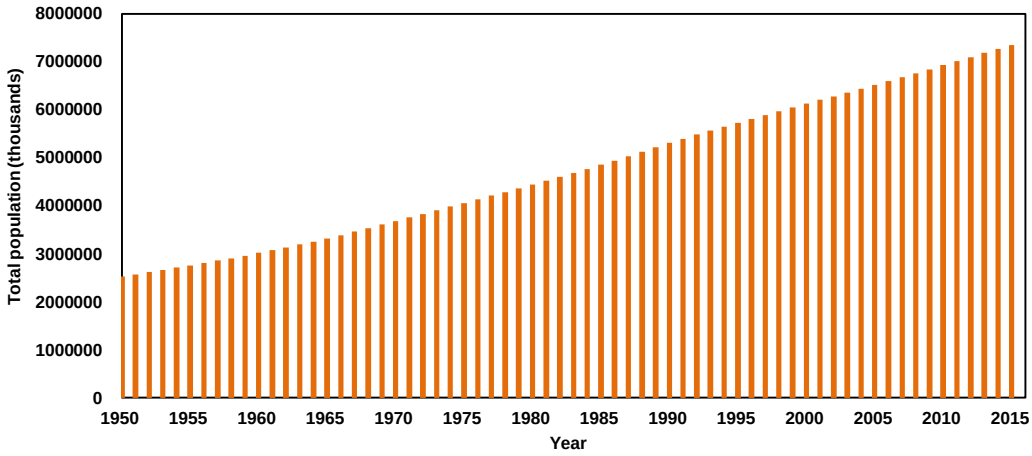

Fig. 1-1. Total population (both sexes combined) by major area, region and country, annually for 1950–2015 (thousands), as estimated by the United Nations, Department of Economic and Social Affairs, Population Division (2015). (Referenced from "World Population Prospects: The 2015 Revision.")

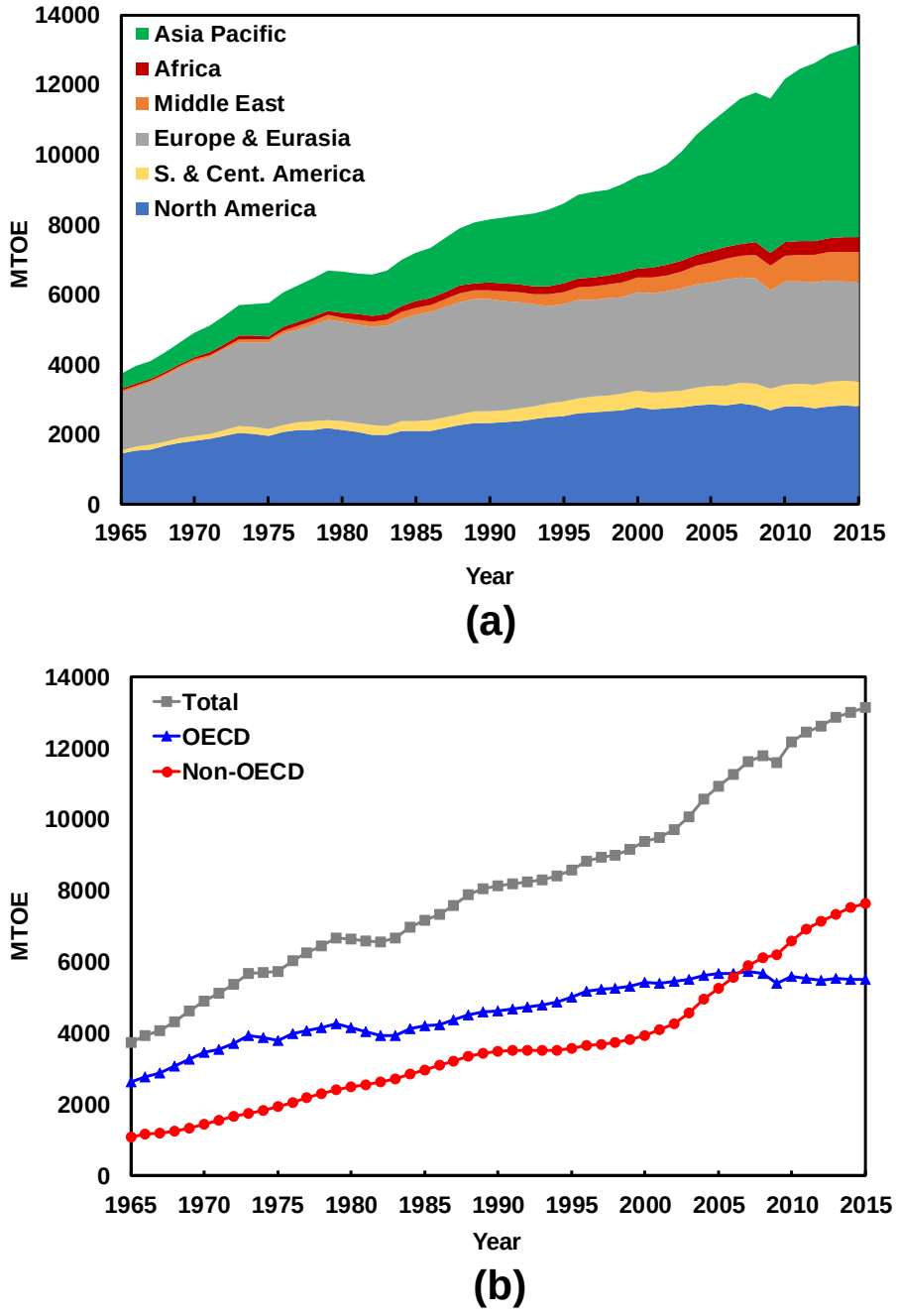

Fig. 1-2. (a) Transition of primary energy consumption in the world from 1965 to 2015 and (b) comparison of the energy consumption trend between OECD and non-OECD countries, as reported by BP. (Referenced from "BP Statistical Review of World Energy 2016 - data workbook.")

1.2 Environmental issues

CO_2, which is one of the greenhouse gasses, enters the atmosphere through consumption of fossil fuels, such as oil and coal. Greenhouse gases absorb and emit radiation within the thermal infrared range; this process is called the “greenhouse effect.” Increasing the quantity of greenhouse gases results in an increase in the global mean surface temperature because greenhouse gases radiate energy in all directions; the result is global warming. According to the Intergovernmental Panel on Climate Change (IPCC), warming of the climate system is unequivocal; the global average CO_2 concentration has increased since the 1900s. IPCC has also mentioned that the atmosphere and ocean have warmed. Consequently, the IPCC has stated that the amounts of snow and ice have diminished and that sea levels have risen [4]. IPCC’s survey and prospects indicate that CO_2 emissions have certainly damaged the global environment and that this issue cannot be resolved without reducing CO_2 emissions. Thus, reducing global CO_2 emissions through the use of non-fossil fuels is paramount.

From the viewpoint of reducing in CO_2 emissions, nuclear energy is promising technology to satisfy increasing energy demand. However, despite their zero emission of CO_2, nuclear power plants pose a serious risk. In fact, the huge earthquake that occurred in the northeast provinces (Tohoku region) of Japan on April 11, 2011 severely damaged the Fukushima nuclear plants, resulting in the leakage of radioactivity into the atmosphere and sea. Because of this tragedy, the development of not only clean but also low-risk energy resources is currently being discussed all over the world, especially in Japan. To circumvent the environmental issues posed by nuclear energy, renewable energy has become an attractive alternative.

1.3 Renewable energy

"Renewable energy" refers to energy collected from renewable sources, such as solar, wind, biomass, geothermal, hydrogen, and waves. Such sources provide a permanent energy supply and can be utilized on a continuous basis without depletion. In addition, these resources do not emit greenhouse gases such as CO_2, which can lead to global warming. Therefore, renewable energy sources have attracted great attention as alternatives to fossil fuels and nuclear power. Given the aforementioned circumstances, solar energy is a promising renewable energy source that is both widespread and universal. In fact, the German Advisory Council on Global Change (WBGU) concluded that solar energy, especially photovoltaics, will be the dominant energy resource in the future [5]. The WBGU has stated that the growth of installed solar energy capacity has far exceeded expectations (12600% growth since 2010), while costs have rapidly decreased (86% decrease since 2000.) Moreover, they have predicted that the ratio of solar power, including that generated by photovoltaics and solar thermal plants, to global primary energy use will reach 23% in 2050 and 63% in 2100 [6].

With respect to the methods for converting solar energy into electricity, photovoltaic cells are promising because they represent an unlimited energy source. Sunlight continuously irradiates the Earth with an energy of 120,000 TW, which is a vast resource compared to other renewable energy sources such as geothermal heat (12 TW), wind power (2–4 TW), and hydroelectric resources (0.5 TW) [7]. Moreover, photovoltaics can generate electricity everywhere because sunlight irradiates the Earth's entire surface. In addition, a photovoltaic cell has no moving parts. A solar cell contains neither turbines nor motors, whereas other renewable energies such as wind power

require moving parts to generate electricity. Therefore, a solar cell generates no noise during operation, resulting in easy installation in residential areas. From these advantages, photovoltaics have great potential to become a main part of world energy resources in the future. However, solar power generation has several issues that must be resolved. For example, power generation capacity fluctuates with weather, the energy density of sunlight is inherently low, and the cost per kilowatt of power generated is high compared with that of other technologies. The high power generation cost is the most serious issue impeding the widespread installation of photovoltaics. The details of this problem are explained in the next section.

1.4 Current status of photovoltaics

The widespread implementation of photovoltaics requires that the cost of power generation be reduced to levels that are comparable with those of other power generation systems that use fossil fuels such as coal and oil. Two approaches have been developed for reducing the generation costs of photovoltaics. One approach is to improve the conversion efficiency (*Eff*) of solar cells. An increase in the *Eff* results in an increase in the electric power generated per unit area. The other approach is to reduce manufacturing costs. If the manufacturing cost is reduced, the price of solar panels also decreases. From the viewpoint of these approaches, several types of solar cells have been studied using various materials and fabrication methods, as shown in Fig. 1-3 [8]. The most popular solar cell is the crystalline silicon-based solar cell, especially those based on single-crystalline or poly-crystalline silicon. Silicon is an elemental semiconductor with good stability and a well-balanced set of electrical, physical, and

chemical properties. Additionally, the study of silicon-based solar cells has a long history, resulting in relatively higher *Eff* compared with those of other solar cells except specialty solar cells. However, reducing the power generation cost of silicon-based solar cells is different because both the materials and fabrication are expensive. Reducing the thickness of absorber layer for cost savings is difficult, which is why hardly any room remains for reducing the power generation cost of crystalline silicon solar cells [8]. A similar situation exists for multi-junction III–V group solar cells, which offer exceptionally high *Eff*s but are also very expensive.

To reduce the material costs, many researchers are focusing on thin-film solar cells made from chemical compounds because their fabrication consumes fewer raw materials. In addition, this type of solar cell can be consistently fabricated on low-cost substrates such as glass, thus enabling the fabrication of solar cells with low power generation costs. Among the chemical compound thin-film solar cells; CdTe-based solar cells are remarkable. An efficiency of 22.1% has been achieved with a single cell [9]. This unexpected improvement in cell performance demonstrates the potential of CdTe-based solar cells. However, CdTe-based cells may become subject to regulation under the Restricting the Use of Hazardous Substances (RoHS) rule because they contain Cd. Devices with Cd are particularly disfavored in Japan because of previous instances of Cd poisoning, known in Japan as itai-itai disease [10]. $Cu(In,Ga)(Se,S)_2$ (CIGSeS)-based solar cells also demonstrate remarkable performance. An efficiency of 22.6% was reported by ZSW [11]. This *Eff* is higher than that of polycrystalline silicon solar cells. The aforementioned *Eff* of 22.6% was demonstrated with a CIGSe cell with a CdS buffer layer; however, Solar Frontier K.K. reported an *Eff* of 22.0% for a CIGSeS cell with a Zn-based (Cd-free) buffer layer [12]. Moreover, the generation cost can be

reduced because of the high-throughput fabrication process. Thus, CIGSeS-based solar cells clearly have strong potential for future implementation. As a newcomer, a perovskite solar cell demonstrated a drastically enhanced *Eff* of 22.1%, as reported by KRICT/UNIST [13]. Perovskite solar cells have great potential because a wet process can be used to fabricate them. However, this material contains lead, which, like Cd, is regulated by the RoHS rule. Additionally, the long-term stability of perovskite solar cells, like that of organic solar cells, is uncertain.

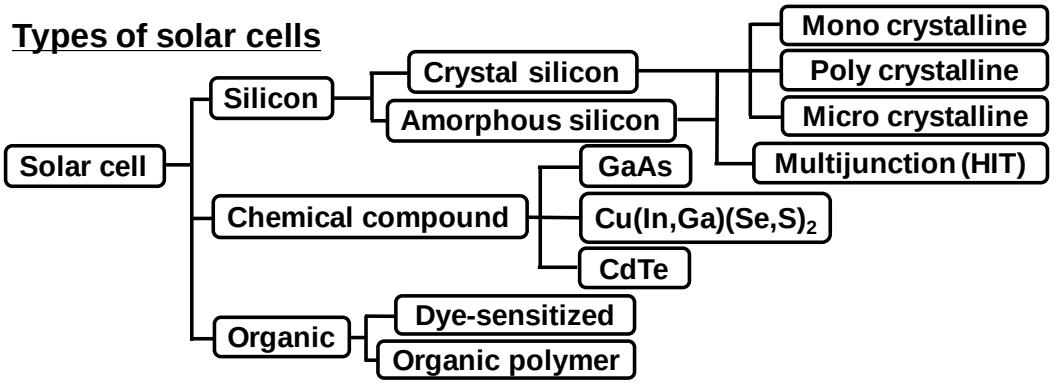

Fig. 1-3. Types of solar cells. (Referenced from "Various solar cells" summarized by Advanced Industrial Science and Technology (AIST).)

1.5 Roadmap "NEDO PV Challenges" in Japan

Many benchmarks and roadmaps concerning photovoltaics have been developed all over the world, especially in the United States of America and in European countries. In Japan, as a new technology development policy, the New Energy and Industrial Technology Development Organization (NEDO) has developed a roadmap as a long-term strategy to expand the proportion of power generated by photovoltaics

(NEDO PV Challenge), as given in Fig. 1-5 [14]. Expanding the power generation share of photovoltaics is quite important from the viewpoint of increasing the self-sufficiency ratio in the primary power supply. It also enables photovoltaics to compete with other energy resources, including both renewable energy and fossil fuel resources.

Currently, the cost of power generation by photovoltaics has reached 17.9 JPY(¥)/kWh for residential and 16.2 ¥/kWh for Non-residential, as shown in Fig. 1-5 [15]. To further increase the share of photovoltaic-generated power, the power generation costs for residential and nonresidential photovoltaic power must be gradually reduced to 14 and 7 ¥/kWh, respectively, which would represent prices equivalent to those of commercial electricity and general power resources. In this roadmap, power generation costs of 14 and 7 ¥/kWh are planned by 2020 and 2030, respectively. In order to achieve these targets, photovoltaic cell performance must be improved and photovoltaic costs must be reduced. The target of 14 ¥/kWh can be accomplished by optimizing existing solar cell designs. However, achieving a power generation cost of 7 ¥/kWh will require a breakthrough in the fabrication of new materials or in the structural design of solar cells. Therefore, CIGSeS-based chalcogenide solar cells, which are relatively inexpensive, have become a focal point. Among them, the Se-free CIGS solar cell is researched in this thesis.

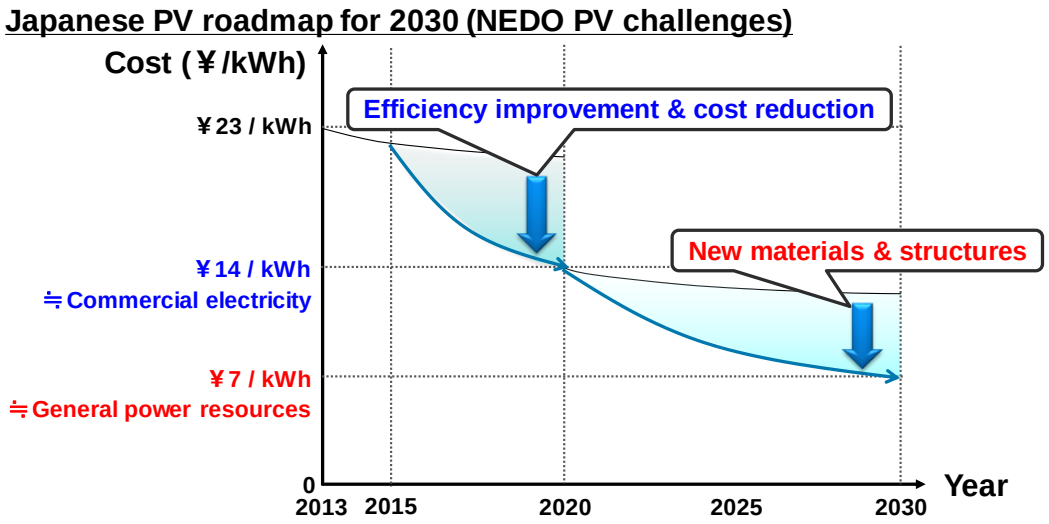

Fig. 1-4. Roadmap of Photovoltaics for 2030 in Japan. (Referenced from "NEDO PV challenges" reported by NEDO.)

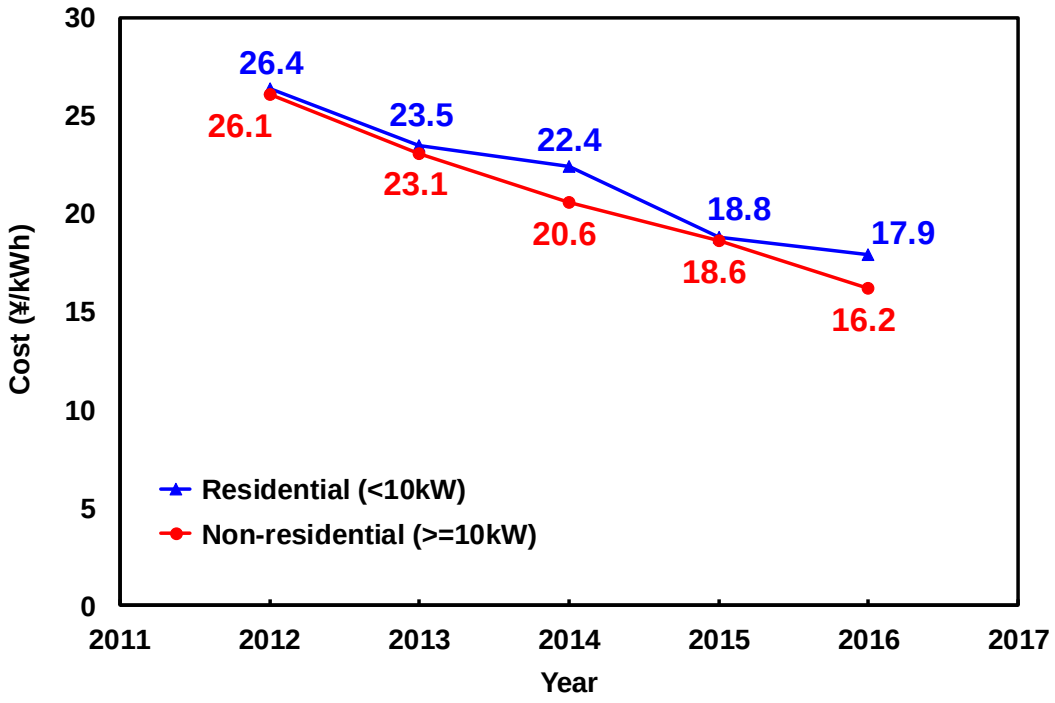

Fig. 1-5. Transition of power generation cost by photovoltaics in Japan. (Referenced from "Transition of power generation cost and system price." reported by NEDO.)

1.6 Se-free Cu(In,Ga)S_2 solar cells with KCN-free process

From the perspective of low-cost production, the Se-free CIGS solar cell is a promising candidate among chalcogenide solar cells because H_2Se gas is not required. However, the *Eff* of Se-free CIGS cells is still lower than that of CIGSe cells, and no remarkable progress has recently been reported in the Se-free CIGS field [12,16]. In addition, Se-free CIGS cells have two further shortcomings that impede their large-scale production. One is the toxic KCN-etching process for absorbers; the other is CdS deposition for buffer layers. The purpose of this study is to enhance the *Eff* of Se-free CIGS cells. Furthermore, KCN-free and Cd-free processes are developed for fabricating Se-free CIGS solar cells with low production costs.

1.7 Objective and outline of this thesis

The main object of this thesis is to develop high-*Eff* Se-free CIGS solar cells with KCN-free and Cd-free processes. Two primary motivations underlie this study. One motivation is to develop a fabrication process free of both KCN and Cd to avoid environmental concerns. The other motivation is to improve the cell performance to satisfy technical requirements. This research was thus conducted to enable the future development of photovoltaic products based on environmentally friendly and higher-*Eff* photovoltaics on Se-free CIGS.

Figure 1-8 shows the outline of this thesis, which comprises seven chapters. Brief descriptions of the chapters are provided as follows:

- Chapter 1 (this chapter)

  This chapter includes background information and a description of the motivation for the study of solar cells.

- Chapter 2

  This chapter explains the history and characteristics of CIGSeS-based thin-films and solar cells, with particular focus on the details of the fabrication processes of Se-free CIGS-based thin-films and solar cells.

- Chapter 3

  This chapter describes the fabrication of a Se-free CIGS absorber layer via a KCN-free process. Special methods to improve the *Eff*, such as high-temperature sulfurization and Ga depth-profile control are also described.

- Chapter 4

  This chapter explains the application of a $Zn_{1-x}Mg_xO$ buffer layer as a Cd-free buffer layer. The effects of the $Zn_{1-x}Mg_xO$ buffer layer—specifically, a wide and controllable bandgap energy—are presented.

- Chapter 5

  This chapter investigates the impact of two interlayers. One interlayer is the MoS_2 layer at the interface between the Mo back electrode and the Se-free CIGS absorber layers. The other interlayer is an intrinsic ZnO (i-ZnO) layer at the interface between $Zn_{1-x}Mg_xO$ buffer and transparent conductive oxide (TCO) layers.

- Chapter 6

  This chapter presents the best results obtained in this work. A new world-record *Eff* for a Se-free CIGS solar cell was achieved; details of this achievement are discussed.

- Chapter 7

  This chapter concludes this thesis and gives future prospects for Se-free CIGS solar cells; in particular, the prospects for the development of future products is described in the context of the Se-free CIGS solar cells developed in the course of this work.

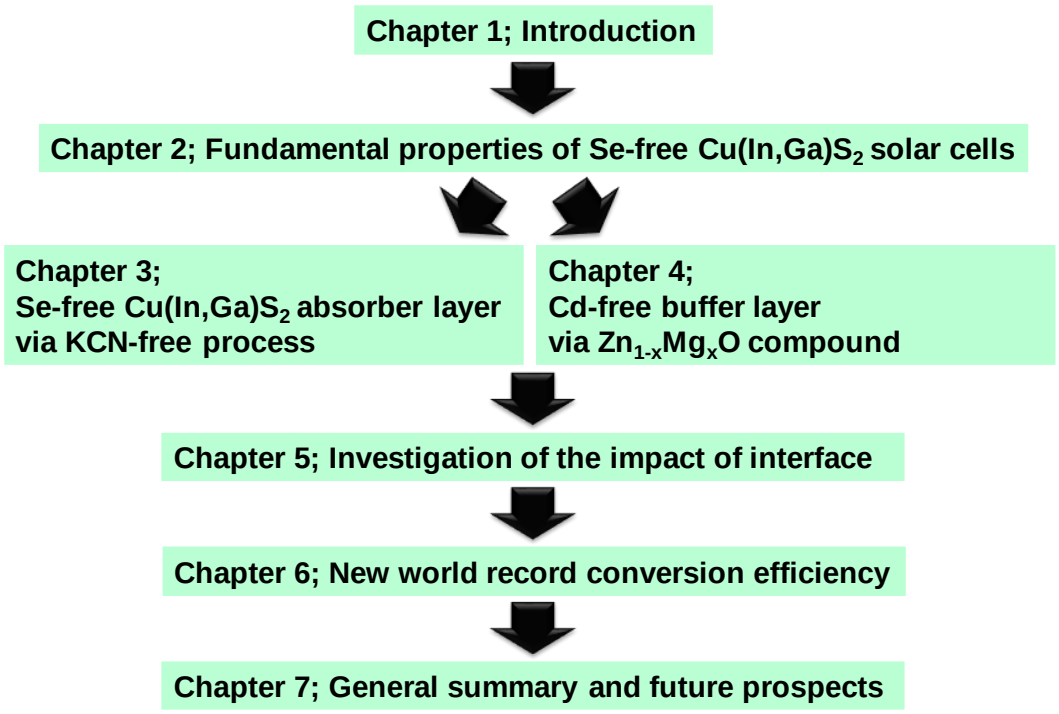

Fig. 1-6. Outline of this thesis.

References

[1] "*World Population Prospects - Population Division - United Nations*". (https://esa.un.org/unpd/wpp/DataQuery/)

[2] *"World Population Clock: 7.5 Billion People (2017) - Worldometers"*. (www.worldometers.info.)

[3] BP Statistical Review of World Energy 2016 - data workbook. (http://www.bp.com/en/global/corporate/energy-economics/statistical-review-of-world-energy.html)

[4] IPCC, 2014, *"Climate Change 2014," Synthesis Report, Contribution of Working Groups I, II and III to the Fifth Assessment Report of the Intergovernmental Panel to Climate Change"* [Core Writing Team, R. K. Pachauri and L. A. Meyer (eds.)]. IPCC, Geneva, Switzerland, 151 pp. in IPCC AR5 Synthesis Report website.

[5] German Advisory Council on Global Change (WBGU), Special Report 2016, *"Development and justice through transformation: The Four Big 'I's."*

[6] German Advisory Council on Global Change (WBGU), Flagship Report 2003, *"World in Transition - Towards Sustainable Energy Systems."*

[7] P. V. Kamat, *J. Phys. Chem. C* **111** (2007) 2834-2860.

[8] Advanced Industrial Science and Technology (AIST), updated in 2010, *"Various solar cells."* (https://unit.aist.go.jp/rcpv/ci/about_pv/types/groups.html).

[9] First solar press release. First Solar Achieves yet another cell conversion efficiency world record, 24 February (2016).

[10] International Center for Environmental Technology Transfer (ICETT), updated in 2010, *"Discover of the itai-itai disease."*

[11] P. Jackson, R. Wuerz, D. Hariskos, E. Lotter, W. Witte, M. Powalla, *Phys. Status*

Solidi RRL **10** (2016) 8, 583-586.

[12] R. Kamada, T. Yagioka, S. Adachi, A. Handa, K. F. Tai, T. Kato, H. Sugimoto, *Proc., 43rd IEEE Photovoltaic Specialists Conference*, Portland, USA (2016).

[13] W. S. Yang, J. H. Noh, N. J. Jeon, Y. C. Kim, S. Ryu, J. Seo, S. I. Seok, *Science* **348** (2015) 6240, 1234–1237.

[14] New Energy and Industrial Technology Development Organization (NEDO), released in 2014, *"NEDO PV Challenges."*

[15] New Energy and Industrial Technology Development Organization (NEDO), *"Transition of power generation cost and system price on photovoltaics in Japan."* (http://www.nedo.go.jp/content/100780914.pdf)

[16] S. Merdes, D. Abou-Ras, R. Mainz, R. Klenk, M. C. Lux-Steiner, A. Meeder, H. W. Schock, J. Klaer, *Prog. Photovolt: Res. Appl.* **21** (2013) 88-93.

2

Fundamental properties of Se-free $Cu(In,Ga)S_2$ solar cells

2.1 Introduction

Thin-film solar cells based on chalcogenide semiconductors are considered to be next-generation photovoltaics because of their strong potential for cost reduction compared with conventional Si-based solar cells. In particular, $Cu(In,Ga)(Se,S)_2$ (CIGSeS)-based thin-film solar cells represent one of the most promising solar cells because of their high conversion efficiency (*Eff*) compared with those of other thin-film solar cells [1,2]. In the area of CIGSeS-based solar cells, they are roughly divided into two groups, $Cu(In,Ga)Se_2$ (CIGSe) and Se-free $Cu(In,Ga)S_2$ (CIGS), as shown in Fig. 2-1[1-8]. Both of these solar cells have been steadily developed for several decades, resulting in substantial advancements in solar cell technology. Recently, the *Eff* of CIGSe and Se-free $Cu(In,Ga)S_2$ (CIGS) solar cells reached 22.6% and 15.5%[1,4]. In comparison to CIGSe, Se-free CIGS showed lower performance; however, Se-free CIGS is a very important material for future chalcogenide solar cells. In this chapter, to demonstrate the potential of Se-free CIGS solar cells, the properties and historical notes of Se-free CIGS solar cells are explained from the viewpoint of comparison with CIGSe solar cells.

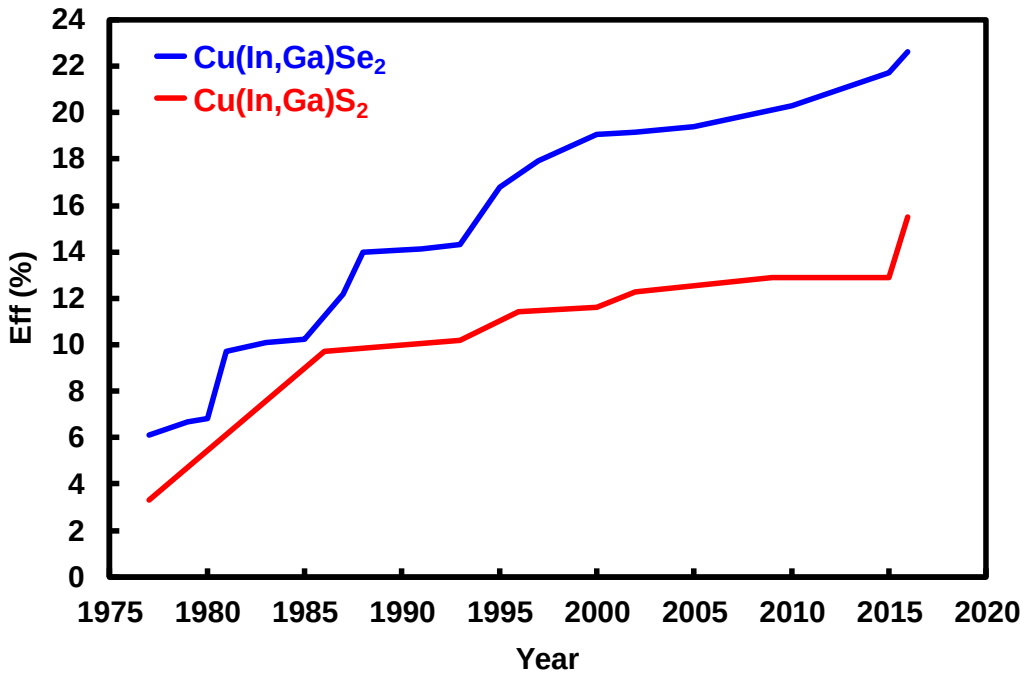

Fig. 2-1. Conversion efficiency trend of CIGSe and Se-free CIGS solar cells.

2.2 Properties of Se-free Cu(In,Ga)S_2 thin-films

2.2.1 Crystal structure

Se-free CIGS belong to the group of I–III–VI_2 semiconductor compounds that crystallize in chalcopyrite form. The chalcopyrite lattice can be developed from a superlattice structure of the zincblende or sphalerite structure, as shown in Fig. 2-2 [9,10]. The Se-free CIGS lattice is referred to as the roquesite structure; its typical lattice constants are a = 5.523 Å and c = 11.13 Å for $CuInS_2$ and a = 5.347 Å and c = 10.47 Å for $CuGaS_2$ [11].

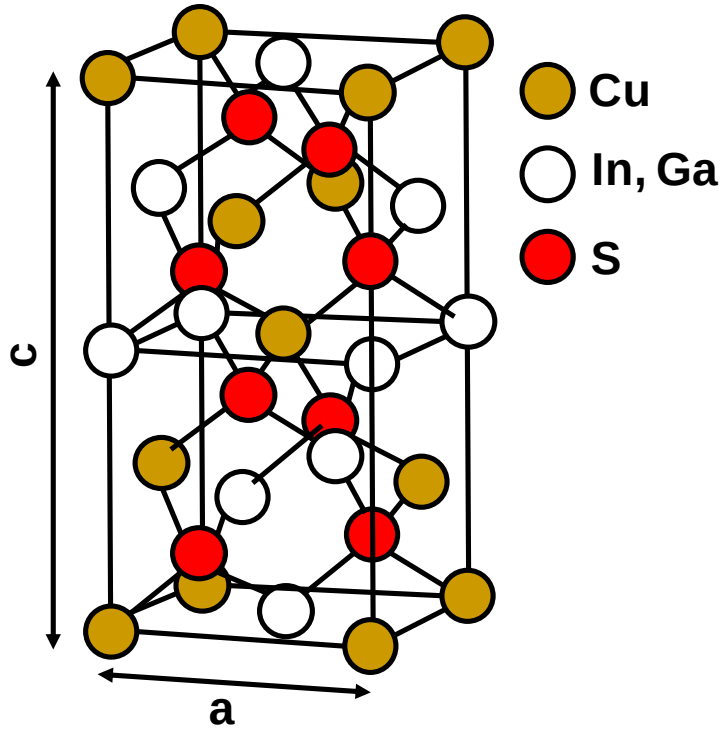

Fig. 2-2. Schematic of the chalcopyrite crystal lattice of Se-free CIGS.

2.2.2 Phase relations

In the phase relations, the interface of the solid–liquid line is important to crystal growth. The phase relations of ternary compounds are represented in pseudo-binary phase diagrams; for example, I–III–VI_2 ($CuInS_2$) compounds are represented in the I_2VI–III_2VI_3 (Cu_2S–In_2S_3) pseudo-binary phase diagram. Figure 2-3 shows the pseudo-binary diagram of Cu_2S-In_2S_3 at moderate pressure; this diagram was published by Fearheiley in 1986 [12]. The γ and δ homogeneity regions represent chalcopyrite and zincblende $CuInS_2$, respectively. The crystal structure of the ζ phase is not known; however, the possibility of wurtzite is high in view of a further expansion of the lattice and increase of the ionicity. In addition, the ε region represents a distinct phase

associated with the compound $CuIn_5S_8$. As evident in the figure, the interaction between the binary sulfide compounds (Cu_2S and In_2S_3) produce two ternary sulfide compounds ($CuInS_2$ and $CuIn_5S_8$). Furthermore, the existence range of single-phase $CuInS_2$ is exceedingly narrow in this pseudo-binary phase diagram. The α_1, α_2, and α regions represent tetragonal, hexagonal, and cubic Cu_2S, respectively. Cu_2S exists on the Cu-rich (In-poor) side. By contrast, the η_1, η_2, and η regions represent a defect-spinel superstructure, a defect-spinel structure, and a layered In_2S_3 structure. In_2S_3 is known to exists on the Cu-poor (In-rich) side.

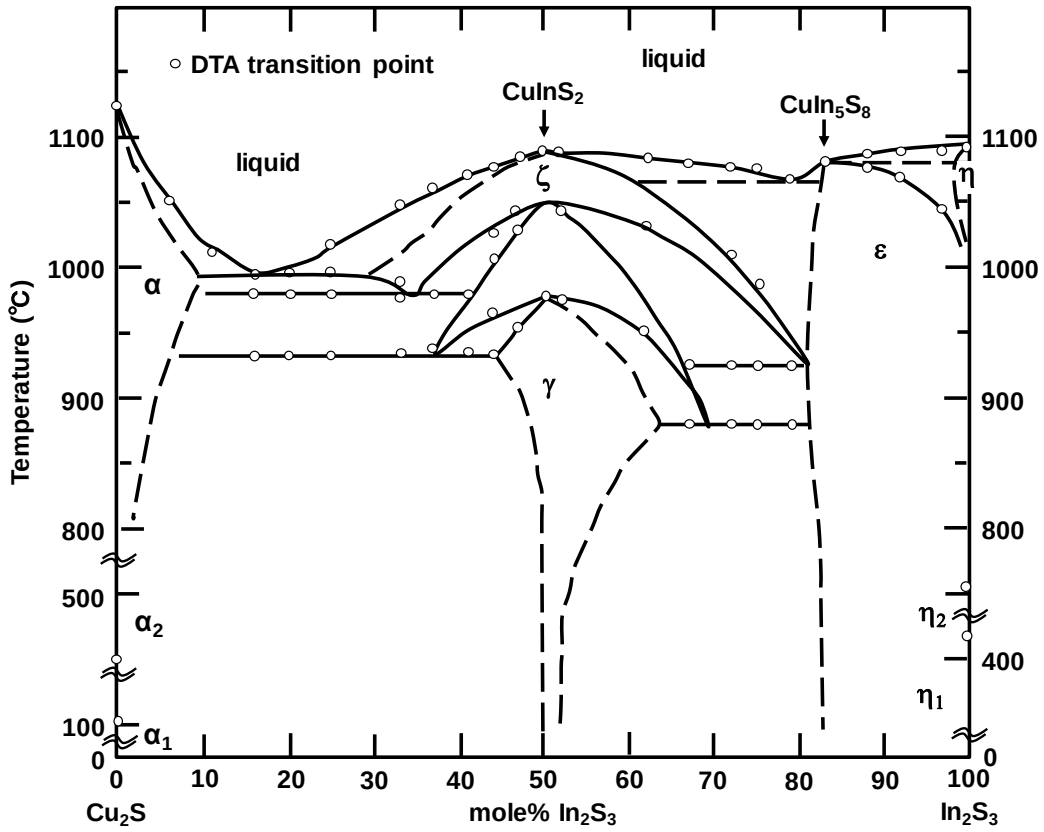

Fig. 2-3. Pseudo-binary phase diagram of Cu_2S–In_2S_3 at moderate pressure. (Referenced from M. L. Fearheiley, *Solar cells* **16** (1986) 91-100.)

2.2.3 Relation between the lattice constant and the bandgap

The relationship between the lattice constant and the bandgap of chalcopyrite materials is shown in Fig. 2-4[13, 14]. The polycrystalline Cu(In,Ga)(Se,S)-based ($CuInS_2$, $CuGaS_2$, $CuIneS_2$, and $CuGaSe_2$) materials are p-type $I–III–VI_2$ compound semiconductors that crystallize in the chalcopyrite lattice, as mentioned in the previous section. According to this figure, the bandgap of CIGSeS-based chalcopyrite compounds increases with the addition of S and Ga. This increase in bandgap is attributed to a decrease of the lattice constant due to a decrease in the atomic radius of the composed elements, and this feature reflects the change in bandgap. The adjustable bandgap also introduces extensive flexibility in the design of photovoltaics such as multi-junction solar cells. The bandgap change due to the addition of S atoms is caused by a decrease of the valence-band minimum dominantly (the conduction-band minimum changes narrowly)[15, 16]. Meanwhile, a bandgap change due to the addition of Ga atoms is known to be caused by an increase of the conduction-band minimum superiorly (the valence-band maximum changes slightly) [17, 18]. These features are important in controlling the bandgap profile in CIGSeS-based solar cells and are quite effective for enhancing the *Eff*. In this thesis, bandgap modification by the addition of Ga is the main focus because of the absence of Se in Se-free CIGS.

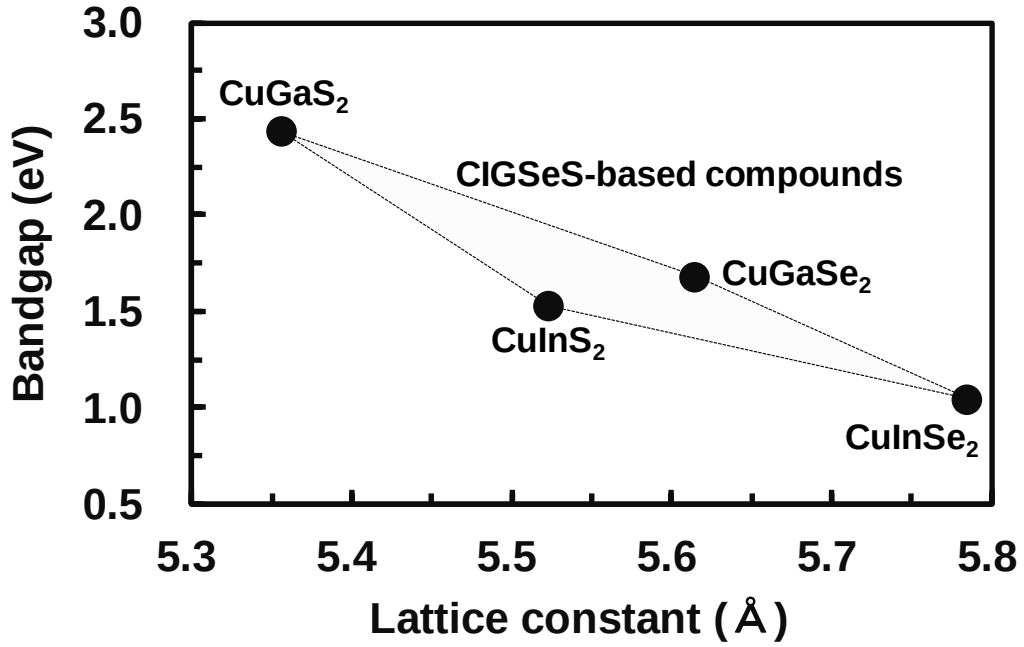

Fig. 2-4. Relationship between the lattice constant and the bandgap of ternary chalcopyrite compounds.

2.2.4 Absorption coefficient

The absorption coefficient (α) can be defined as

$$\alpha(h\nu) \propto A / (h\nu)(h\nu - Eg)^{1/2} \qquad (2\text{-}1)$$

$$\alpha(h\nu) \propto B / (h\nu)(h\nu - Eg)^{2} \qquad (2\text{-}2)$$

where h and Eg are Planck's constant and the bandgap, respectively, and A and B constants. Equations 2-1 and 2-2 represent the absorption coefficient for direct (square root dependence on photon energy) and indirect (quadratic dependence on the photon energy) semiconductors, respectively.

Figure 2-5 shows the absorption coefficients of different materials, as reported by Mertens in 2014 [19]. The absorption coefficient of $CuInS_2$ is higher than those of other semiconductors because $CuInS_2$ has a direct bandgap of approximately 1.53 eV [20].

Because of this feature, the thickness of $CuInS_2$ as an absorber layer can be reduced, which is an important feature for the low-cost fabrication of solar cells because a thinner absorber layer reduces material costs.

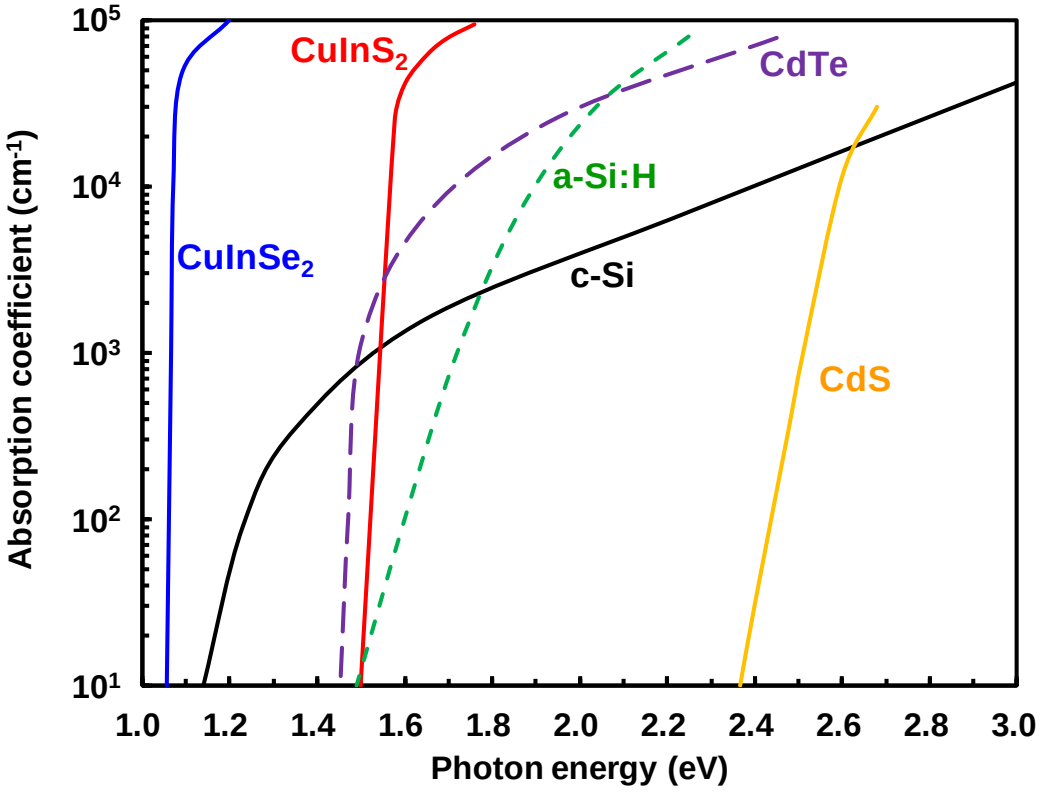

Fig. 2-5. Relationship between optical absorption coefficient and photon energy for different semiconductors. (Referenced from K. Mertens, "*PHOTOVOLTAICS FUNDAMENTALS, TECHNOLOGY AND PRACTICE," Wiley,* (2014) 63.)

2.2.5 Defect structure

Figure 2-6 shows a defect diagram of $CuInS_2$. In addition, Table 2-I summarizes the type, level, and nature of defects in $CuInS_2$, as reported by Liu *et al.* [21]. Here, V_{Cu}, V_{In}, and V_S represent Cu, In, and S vacancies, respectively. Cu_{In}, In_{Cu}, S_{In}, and S_{Cu} represent

the antisite defects of Cu atoms on In sites, In atoms on Cu sites, S atoms on In sites, and S atoms on Cu sites, respectively. Cu_i, In_i, and S_i represent interstitial defects of Cu, In, and S atoms. As shown in Figure 2-5, V_{Cu}, V_{In}, S_i, Cu_{In}, and S_{In} are acceptor levels located at 0.1 eV, 0.15 eV, 0.17 eV, 0.22 eV, and 0.39 eV above the valence-band maximum. By contrast, Cu_i, S_{Cu}, V_s, In_{Cu}, and In_i are donor levels located 0.45 eV, 0.30 eV, 0.15 eV, 0.125 eV, and 0.066 eV below the conduction-band minimum, respectively. These investigations related to defect structures are useful in the development of fabrication processes for solar cells.

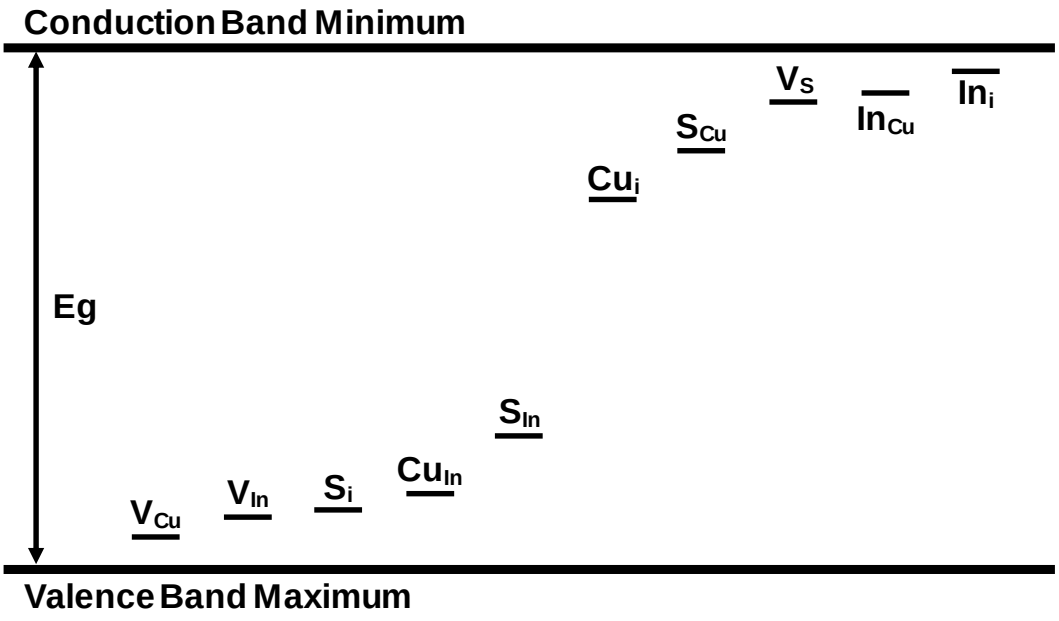

Fig. 2-6. Defect level diagram of $CuInS_2$.

Table 2-I. Defect type, level, and nature in $CuInS_2$.

Defect type	Defect level (eV)	Defect nature
V_{Cu}	E_V + 0.100	Acceptor
V_{In}	E_V + 0.150	Acceptor
S_i	E_V + 0.170	Acceptor
Cu_{In}	E_V + 0.220	Acceptor
S_{In}	E_V + 0.390	Acceptor
Cu_i	E_C - 0.450	Donor
S_{Cu}	E_C - 0.300	Donor
V_S	E_C - 0.150	Donor
In_{Cu}	E_C - 0.125	Donor
In_i	E_C - 0.066	Donor

E_V+ means above valence band maximum
E_C- means below conduction band minimum

2.3 Structure of Se-free $Cu(In,Ga)S_2$ solar cells

2.3.1 Device structure

A schematic of the Se-free CIGS solar cell structure is shown in Fig. 2-7. First, the Mo back electrode layer and the Cu, Ga, and In metal-stack precursor layers are deposited by DC sputtering onto a glass substrate. The precursor layers are annealed under H_2S gas in a furnace to form a p-type Se-free CIGS absorber layer; this process is called sulfurization. As the next step, an n-type CdS or $Zn_{1-x}Mg_xO$ buffer layer is deposited onto the absorber layer by chemical bath deposition (CBD) or atomic layer deposition (ALD) to form a p-n junction at an interface between the p-type absorber and n-type

buffer layers. The intrinsic ZnO (i-ZnO) buffer and In_2O_3:Sn transparent conductive oxide (TCO) layers are then deposited by ALD and ion evaporation, respectively. (The i-ZnO layer with high resistivity is incorporated into n-type buffer/TCO to prevent leakage current at the p-type absorber/TCO interface, which may form because of insufficient thickness of the n-type buffer layer.) Finally, Ni/Al front electrode and MgF_2 anti-reflection layers are deposited via electron-beam evaporation.

Several methods to fabricate p-type Se-free CIGS absorbers have been developed, including a solution process using chemical ink, a co-evaporation process by molecular beam epitaxy, and a sulfurization process via H_2S gas annealing in a furnace [22-24]. Likewise, several methods to deposit n-type buffer layers on p-type absorbers have been developed, including evaporation, sputtering, CBD, and ALD [25-28]. In this thesis, a sulfurization process is used to form the absorber; in addition, CBD and ALD are adopted for deposition of CdS and $Zn_{1-x}Mg_xO$ buffer layers, respectively. The details of these processes will be discussed later.

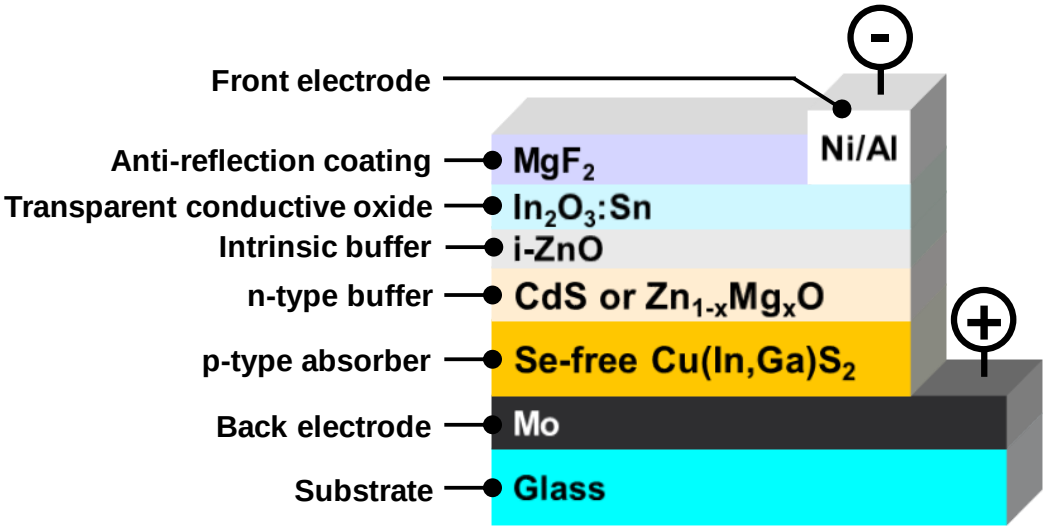

Fig. 2-7. Structure of a Se-free CIGS solar cell.

2.3.2 Band structure

Schematic band structures of Se-free CIGS solar cells are shown in Fig 2-8. Figure 2-8 (a) shows the negative value of the conduction band offset (CBO), referred to as the "cliff," and Fig. 2-8(b) shows the positive value of the CBO, referred to as the "spike." [29]. For hetero-junction solar cells, controlling the CBO at the interface between the p-type absorber and n-type buffer layers is important because the cliff induces recombination at the interface; by contrast, the spike reduces recombination at the interface. Specifically, Minemoto *et al*. mentioned that a high efficiency was obtained with CIGSeS-based solar cells when the value of CBO is spike, where the preferred CBO range is between 0.0 and 0.4 eV [30]. However, a typical Se-free CIGS solar cell demonstrates the cliff structure because of bandgap mismatch between the p-type absorber (Eg > 1.5 eV) and n-type buffer (Eg = 2.4 eV) layers. Thus, in this thesis, a $Zn_{1-x}Mg_xO$ buffer (Eg > 3.2 eV) layer is applied as an alternative buffer layer to modify the CBO from cliff to spike. Details of the CBO modification will be presented later.

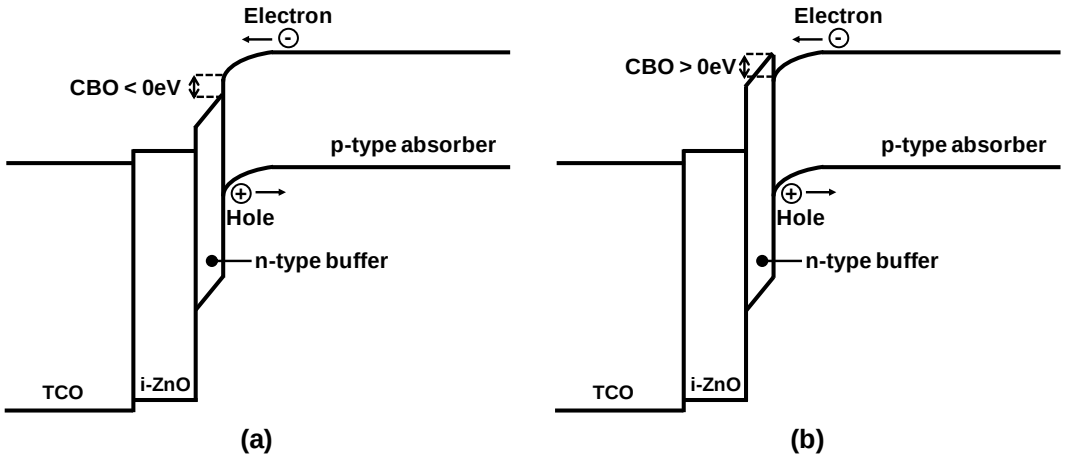

Fig. 2-8. Schematic band structures in the case of (a) a CBO < 0 eV "spike" and (b) a CBO > 0 eV "cliff" in Se-free CIGS solar cells.

2.4 Chapter summary

This chapter gave the history and fundamental properties of Se-free CIGS semiconductors based on CIGSeS-based compounds. Se-free CIGS semiconductors have several features that are beneficial to the absorber of solar cells, such as, a controllable bandgap and a high absorption coefficient. In addition, the *Eff* has been drastically improved in recent years. Details of how the *Eff* is enhanced on Se-free CIGS solar cells are revealed and discussed in the next chapter.

References

[1] P. Jackson, R. Wuerz, D. Hariskos, E. Lotter, W. Witte, M. Powalla, *Phys. Status Solidi RRL* **10** (2016) 8, 583-586.

[2] R. Kamada, T. Yagioka, S. Adachi, A. Handa, K. F. Tai, T. Kato, H. Sugimoto, *Proc., 43rd IEEE Photovoltaic Specialists Conference*, Portland, USA (2016) 1287-1291.

[3] P. Jackson, D. Hariskos, R. Wuerz, O. Kiowski, A. Bauer, T. M. Friedlmeier, M. Powalla, *Phys. Status Solidi RRL* **9** (2015) 1, 28-31.

[4] H. Hiroi, Y. Iwata, S. Adachi, H. Sugimoto, A. Yamada, *IEEE Journal of Photovoltaics* **6** (2016) 3, 760-763.

[5] L. L. Kazmerski, G. A. Sanborn, *J. Appl. Phys.* **48** (1977) 3178.

[6] H.W. Schock, R. Noufi, *Prog. Photovolt. Res. Appl.* **8** (2000) 151-161.

[7] R. Klenk, J. Klaer, R. Scheer, M.Ch. Lux-Steiner, I. Luck, N. Meyer, U. Ruhle, *Thin Solid Films* **480-481** (2005) 509-514.

[8] R. Scheer, *Prog. Photovolt. Res. Appl.* **20** (2012) 507-511.

[9] B. R. Pamplin, *Prog. Crystal Growth Charact*. **1** (1979) 331-387.

[10] B. E. Johnson, “The Role of Cd and Ga in the Cu(In,Ga)S_2/CdS Heterojunction Studied with X-Ray Spectroscopic Methods,” (Dissertation, Berlin, Helmholtz Centre Berlin (HZB-Berichte), 2010) 41.

[11] S. C. Abrahams, J. L. Bernstein, *J. Chem. Phys.* **59** (1973) 5415.

[12] M. L. Fearheiley, *Solar cells* **16** (1986) 91-100.

[13] J. E. Jaffe, A. Zunger, *Phys. Rev. B* **29** (1983) 4, 1882-1906.

[14] H. W. Spiess, U. Haeberlen, G. Brandt, A. Rauber, J. Schneider, *Phys. Status Solidi B* **62** (1974) 183.

[15] M. Turcu, I. M. Kotschau, U. Rau, *J. Appl. Phys.* **91** (2002) 1391.

[16] M. Turcu, U. Rau, *Thin Solid Films* **431-432** (2003) 158-162.

[17] S. H. Wei, S. B. Zhang, A. Zunger, *Appl. Phys. Lett.* **72** (1998) 3199.

[18] S. H. Han, F. S. Hasoon, J. W. Pankow, A. M. Hermann, D. H. Levi, *Appl. Phys. Lett.* **87** (2005) 151904.

[19] K. Mertens, "*PHOTOVOLTAICS FUNDAMENTALS, TECHNOLOGY AND PRACTICE," Wiley,* (2014) 63.

[20] H. Neumann, W. Horig, V. Savelev, J. Lagzdonis, B. Schumann, G. Kuhn, *Phys. Rev. B* **79** (1981) 167-171.

[21] X. Liu, X. Dou, M. Sugiyama, *Jpn. J. Appl. Phys.* **51** (2012) 122403.

[22] S. J. Park, J. W. Cho, J. K. Lee, K. Shin, J. H. Kim, B. K. Min, *Prog. Photovolt: Res. Appl.* **22** (2014) 122-128.

[23] R. Scheer, I. Luck, M. Kanis, M. Matsui, T. Watanabe, T. Yamamoto, *Thin Solid Films* **392** (2001) 1-10.

[24] T. Watanabe, M. Matsui, *Jpn. J. Appl. Phys.* **35** (1996) 1681-1684.

[25] Y. Ohtake, T. Okamoto, A. Yamada, M. Konagai, K. Saito, *Sol. Energy Mater. Sol. Cells* **49** (1997) 269-275.

[26] D. Hariskos, B. Fuchs, R. Menner, N. Naghavi, C. Hubert, D. Lincot, M. Powalla, *Prog. Photovolt: Res. Appl.* **17** (2009) 479-488.

[27] Y. Hashimoto, N. Kohara, T. Negami, N. Nishitani, T. Wada, *Sol. Energy Mater. Sol. Cells* **50** (1998) 71-77.

[28] T. Torndahl, C. Platzer-Bjorkman, J. Kessler, M. Edoff, *Prog. Photovolt: Res. Appl.* **15** (2007) 225-235.

[29] S. Siebentritt, *Solar Energy* **77** (2004) 767-775.

[30] T. Negami, T. Minemoto, Y. Hashimoto, T. Satoh, *28th IEEE Photovoltaic Specialists Conf*. (2000) 636.

3

Se-free $Cu(In,Ga)S_2$ absorber layer via KCN-free process

3.1 Introduction

Research into Se-free $Cu(In,Ga)S_2$ (CIGS) solar cells has been carried out by numerous groups all over the world [1-4]. Generally, high-performance Se-free CIGS absorbers are fabricated with a Cu-rich composition, where the Cu/(Ga+In) (CGI) ratio is greater than 1.0 (CGI > 1.0) because a Cu-rich composition facilitates the grain growth of crystals compared with Cu-poor compositions whose CGI ratio is less than 1.0 (CGI < 1.0) [5,6]. However, a CuS layer segregates on the surface of Cu-rich absorbers as a second layer and degrades the cell performance by creating a shunt-pass. Thus, a KCN-etching treatment is well known to be an effective method for removing the deleterious CuS layer from Se-free CIGS absorbers to improve the cell performance. However, KCN is highly toxic; moreover, the KCN-etching treatment has been predicted to increase the production-line manufacturing cost of solar cells [7,8]. As such, in this thesis, a KCN-free process was used in the fabrication of Se-free CIGS absorbers from the viewpoint of environmental friendliness and cost minimization while simultaneously boosting the conversion efficiency (*Eff*). A Cu-poor composition was used to prepare Se-free CIGS solar cells using a KCN-free process.

3.2 Cu-poor composition

Figure 3-1 shows a schematic of the fabrication process for Cu-poor absorbers. As a precursor layer, Cu, Ga, and In metals were stacked on a glass substrate by DC sputtering. The precursor layer was then annealed with H_2S gas (sulfurization) in a furnace to form a Se-free CIGS absorber layer. In this process, the deposition of a precursor layer with a CGI ratio less than 1.0 is important for achieving a Cu-poor absorber without a CuS secondary layer. After sulfurization, the elemental composition and depth-profile of the absorber were measured by inductively coupled plasma atomic emission spectroscopy (ICP-AES) to determine the CGI ratio. Furthermore, X-ray diffraction (XRD) analysis was conducted to identify the components of absorbers (e.g., $Cu(In,Ga)S_2$ and CuS) after sulfurization. Consequently, Cu-poor absorbers of Se-free CIGS were stably obtained in this study.

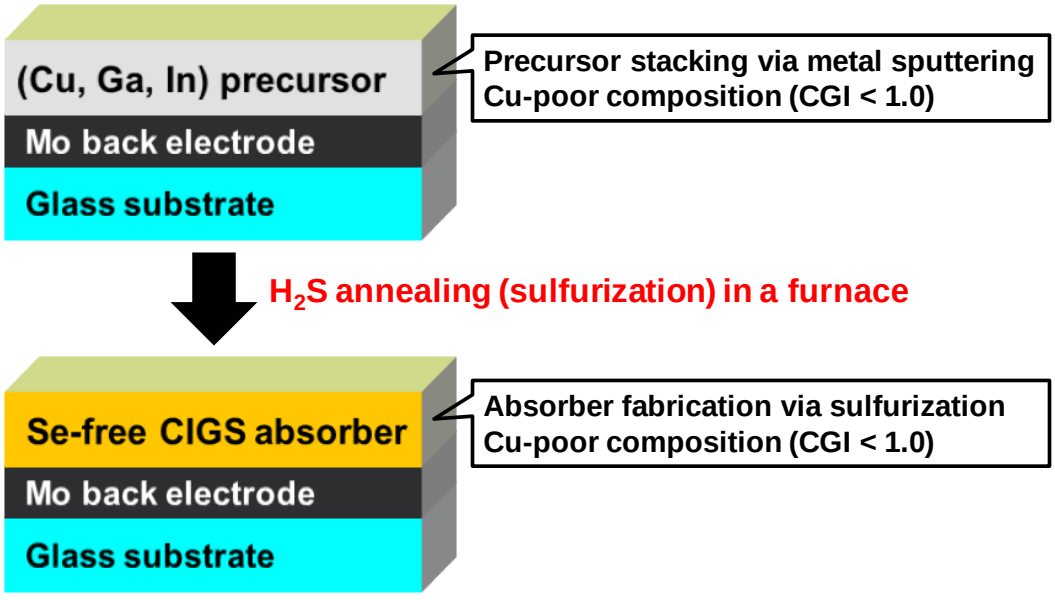

Fig. 3-1. Fabrication process of Cu-poor absorber for Se-free CIGS solar cells.

The metal contents in a Se-free CIGS absorber measured by ICP-AES analysis are shown in Table 3-I. The CGI is clearly less than 1.0. In addition, Fig. 3-2 shows that no CuS layer is present in either the surface or the bulk. These results demonstrate that a Cu-poor absorber is obtained from a Cu-poor precursor and that the absorber does not contain a CuS layer.

Table 3-I. Metal contents in a Se-free CIGS absorber.

Cu ($\mu mol/cm^2$)	In ($\mu mol/cm^2$)	Ga ($\mu mol/cm^2$)	S ($\mu mol/cm^2$)	Cu/(Ga+In) (a.u.)
2.19	2.11	0.252	4.79	0.928

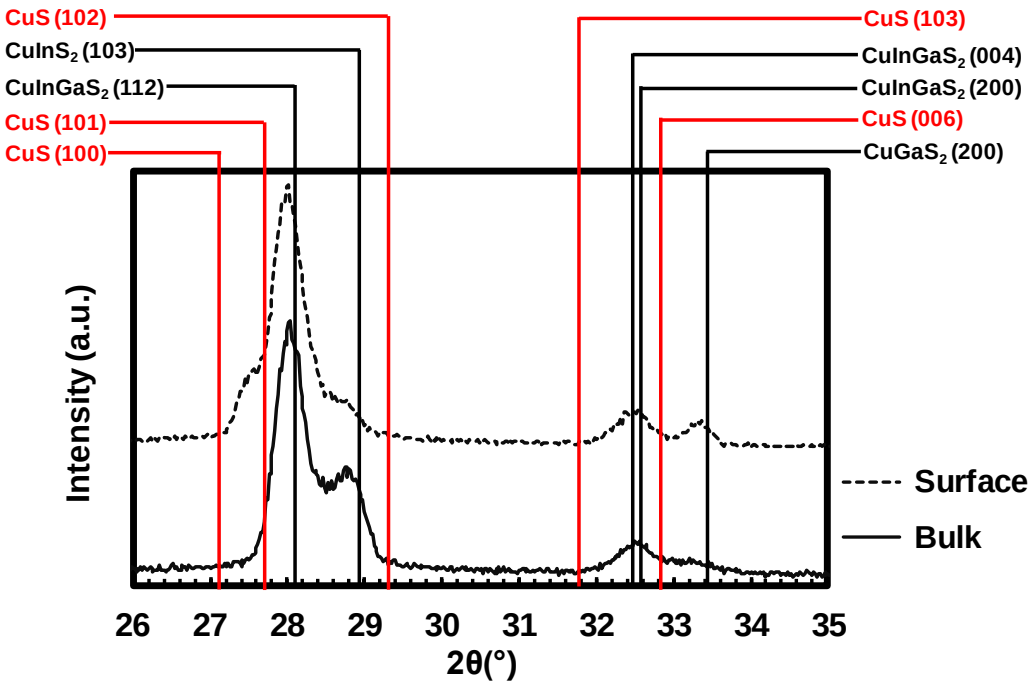

Fig. 3-2. X-ray diffraction pattern of a Se-free CIGS absorber with a Cu-poor composition (CGI = 0.928). References peak positions for CuS, $CuInS_2$, $CuGaS_2$, and $Cu(In,Ga)S_2$ were taken from JCPDS patterns.

Figure 3-3 shows the results of the (a) current–voltage (*J*–*V*) measurement and (b) external quantum efficiency (EQE) characteristics for the first trial cell. The results indicate an *Eff* of 3.97% and a bandgap (*Eg*) of 1.53 eV. A scanning electron microscopy (SEM) image of the absorber from the first trial is shown in Fig. 3-4. The SEM image of the absorber indicates that the crystal grain of the bulk material is small and that the surface morphology is very rough. It is assumed that one of the reasons for the low *Eff* is the small grain-size and rough surface of the absorber. Thus, to promote the crystal growth was attempted as the first step toward improving of cell performance.

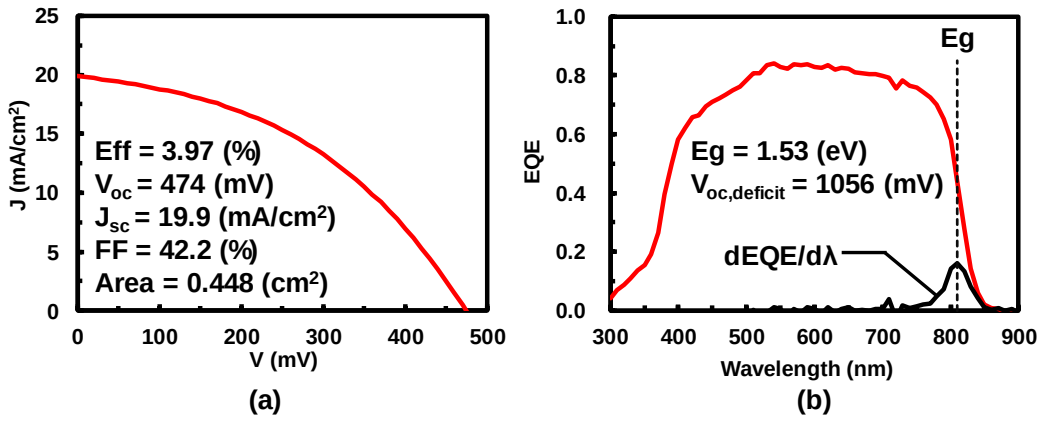

Fig. 3-3. (a) *J*–*V* and (b) EQE characteristics of the first trial Se-free CIGS solar cell. The *Eg* was calculated from dEQE/d λ . (© 2015 IEEE.)

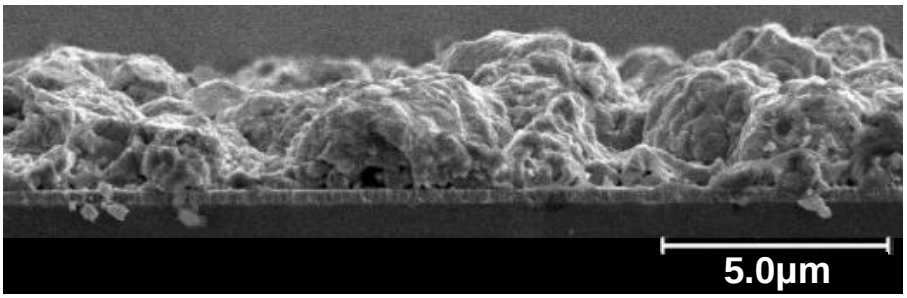

Fig. 3-4. SEM cross-section image of the first trial Se-free CIGS absorber. (© 2015 IEEE.)

3.3 Crystal growth

Figure 3-5 shows microstructure and morphological observations of the temperature dependence of the Se-free CIGS crystal growth during sulfurization. The SEM images indicate that the grain size increases as the sulfurization temperature is increased (for the same metal composition). The lowest temperature (570°C) used in the experiments resulted in a poorly crystalline absorber with a rough surface (Fig. 3-5 (a)). A higher temperature (625°C) improved the roughness of the absorber (Fig. 3-5 (b)). However, the grain-sizes of both absorbers were still very small. A relatively high temperature (650°C) resulted in improved grain size, and the highest investigated temperature (675°C) eventually resulted in large grains (Fig. 6(c) and (d)). Compared with typical CIGSeS-based absorber fabrication, higher temperature is needed for the crystal growth of Se-free CIGS absorber. As a result, a large grain size of Se-free CIGS was obtained via sulfurization at 675°C despite the Cu-poor composition. The cell performance of this Se-free CIGS solar cell with a large grain size will be discussed later.

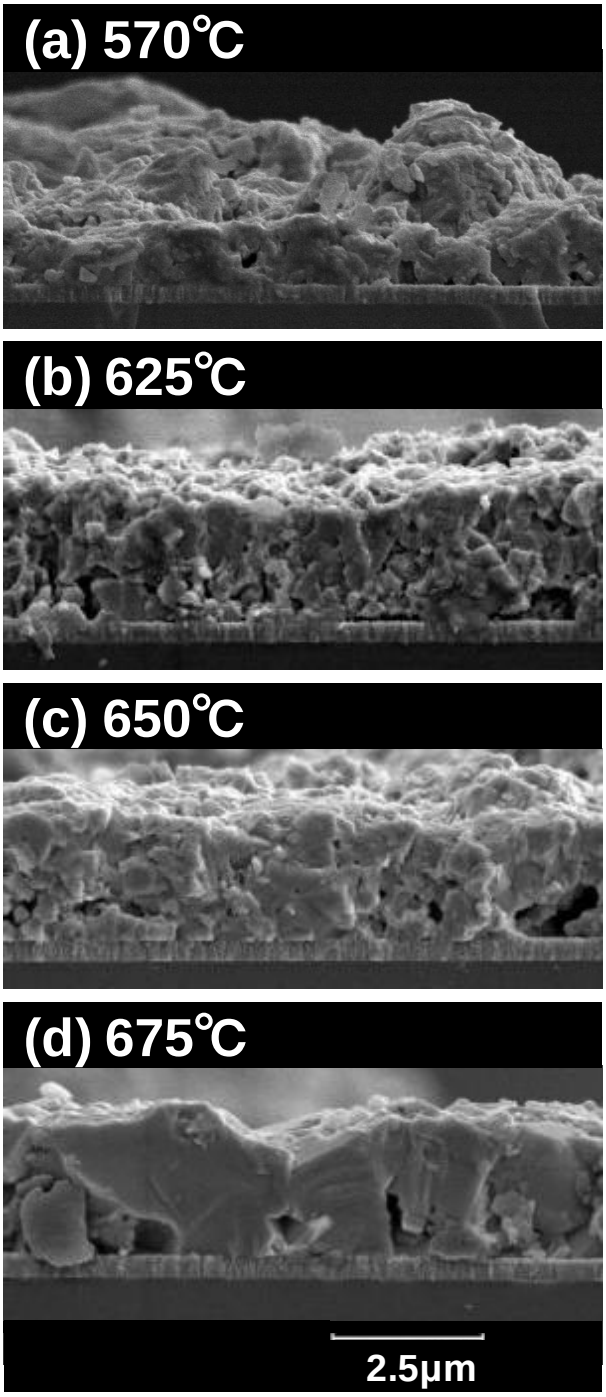

Fig. 3-5. Morphology of a Se-free CIGS crystal grown during sulfurization at (a) 570°C, (b) 625°C, (c) 650°C, (d) 675°C. (These temperatures are the setup temperatures, not the substrate temperatures. The actual temperature of the substrate under each condition is likely lower.) (© 2015 IEEE.)

3.4 Ga depth profile

3.4.1 Ga/(Ga+In) ratio

The previous experiments revealed that high-temperature (>650°C) sulfurization enabled the fabrication of a large-grain absorber. However, compared to the cell performance achieved with the absorber used in the first trial (see Fig. 3-4.), that achieved with the absorber with larger grain size was not improved, as shown in Fig. 3-6. It is assumed that this lack of improvement was caused by the depth profiles of the metals in the absorber—specifically, the Ga and Ga/(Ga+In) (GGI) ratio. Generally, a high Ga content on the surface of an absorber degrades the cell performance because of defects at the p-n junction. However, the benefits of Ga grading on CIGSeS-based solar cells are well known, and many research groups have reported that the overall performance of CIGSeS-based cells can be improved by implementing optimized Ga grading depth profiles instead of ungraded profiles [6, 9-11]. In this section, the benefits of Ga grading on the performance of Se-free CIGS cells are investigated. The Ga depth profiles were formed by adjusting the Ga contents of precursor layers and the sulfurization process for absorber layers. The GGI ratio of the absorber was calculated from the resulted of glow discharge optical emission spectrometry (GD-OES) and ICP-AES analyses. Figure 3-7 shows the Ga depth profile of the absorber used in the device whose characteristics are shown in Fig. 3-6. A high GGI ratio of 15% was observed at the surface; in addition, its depth-profile gradient is gentle. On the basis of these results, to develop an absorber with a low GGI ratio on its surface and GGI grading in its depth profile was attempted.

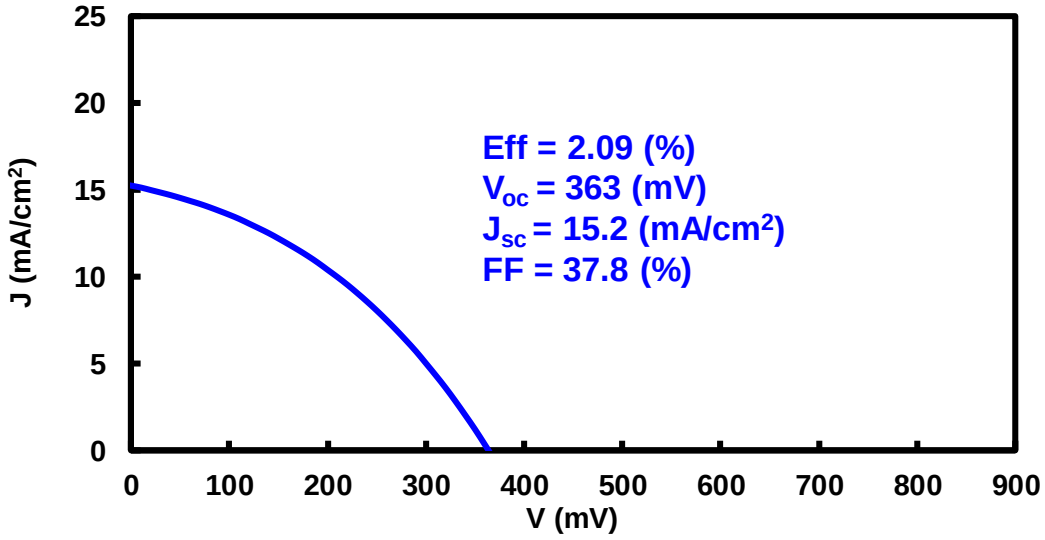

Fig. 3-6. *J–V* characteristics of a Se-free CIGS cell fabricated with 675°C sulfurization.

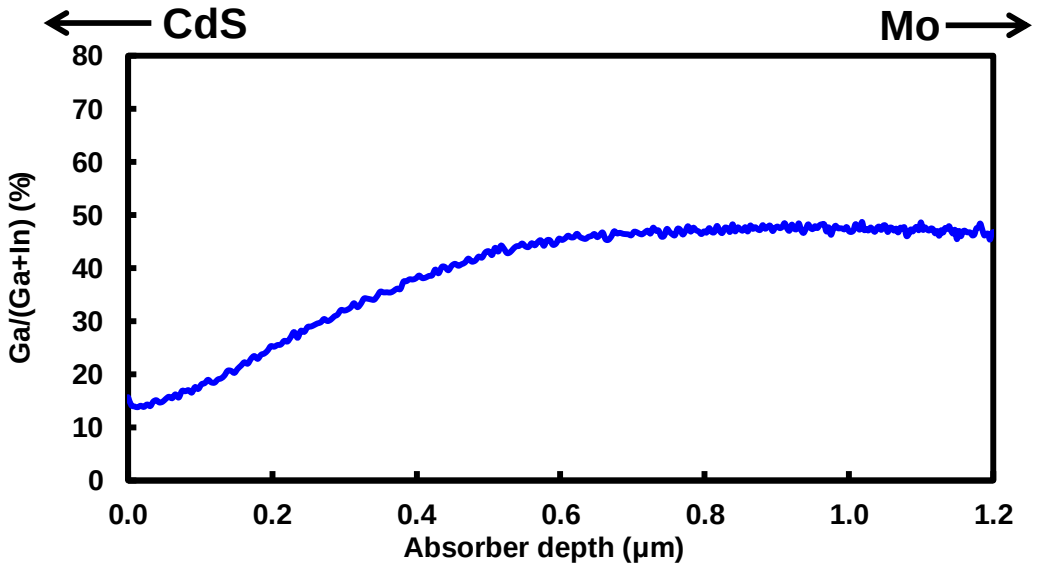

Fig. 3-7. GGI ratio as a function of film depth of a Se-free CIGS absorber fabricated with 675°C sulfurization.

3.4.2 Numerical simulation

First, a numerical simulation was conducted on the basis of the experimental results shown in Fig. 3-6. In this thesis, a solar cell capacitance simulator (SCAPS) developed by Prof. M. Burgelman in the University of Gent, Belgium was used for one-dimensional device simulation [12]. Figure 3-8 compares the of *J*–*V* curves between the experimental and simulated results. In addition, a comparison of the GGI depth profiles is presented in Fig. 3-9. The main parameters for the simulation are shown in Table 3-II. In the table, *W*, *Eg*, χ and ε_r are the thickness, bandgap, electron affinity and relative permittivity, respectively. N_A, N_D, N_C, N_V, and Defect express a shallow acceptor, a shallow donor, the effective conduction band, the effective valence band, and defect densities, respectively. Furthermore, μ_e and μ_h are the electron and hole mobilities. The parameters of the Se-free CIGS vary because the depth-directional distribution of the GGI ratio in the absorber is not uniform as shown in Fig. 3-7. The relationship between the *Eg* and the GGI ratio is defined by the following formula:

$$Eg(x) = \alpha(1-x) + \beta x \qquad (3\text{-}1)$$

where *x*, α, and β are the GGI ratio and the bandgaps of $CuInS_2$ and $CuGaS_2$, respectively. In this section, *x* was calculated via GD-OES and ICP-AES analyses; the values for α and β are cited from the literature [13].

The results of the simulations agree very well with experimental measurements with respect to both the *J*–*V* curve and the GGI depth-profile. On the basis of these simulations, the effects of Ga grading in the Se-free CIGS absorber will be clarified in the next section.

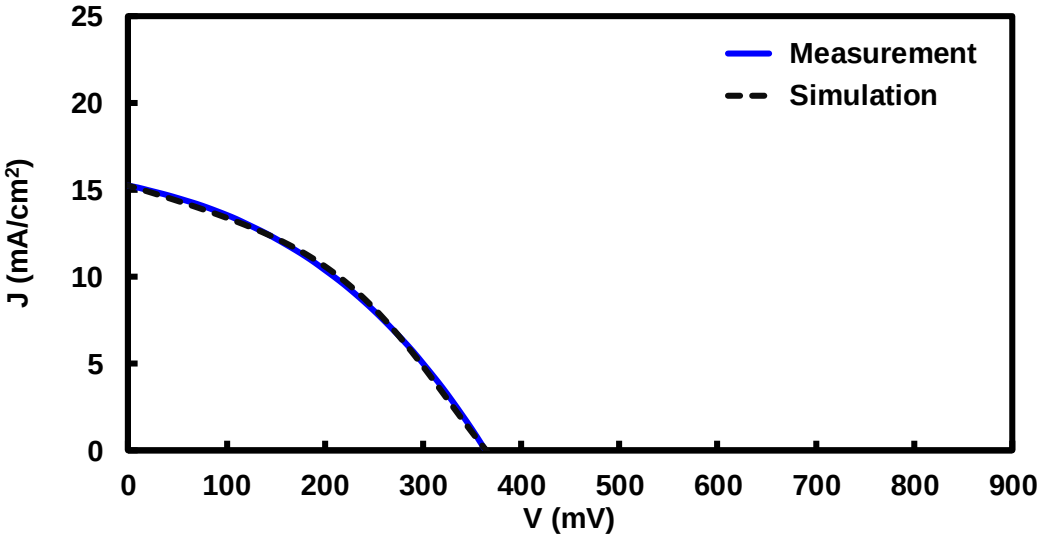

Fig. 3-8. Comparison of the measured and simulated *J*–*V* curves.

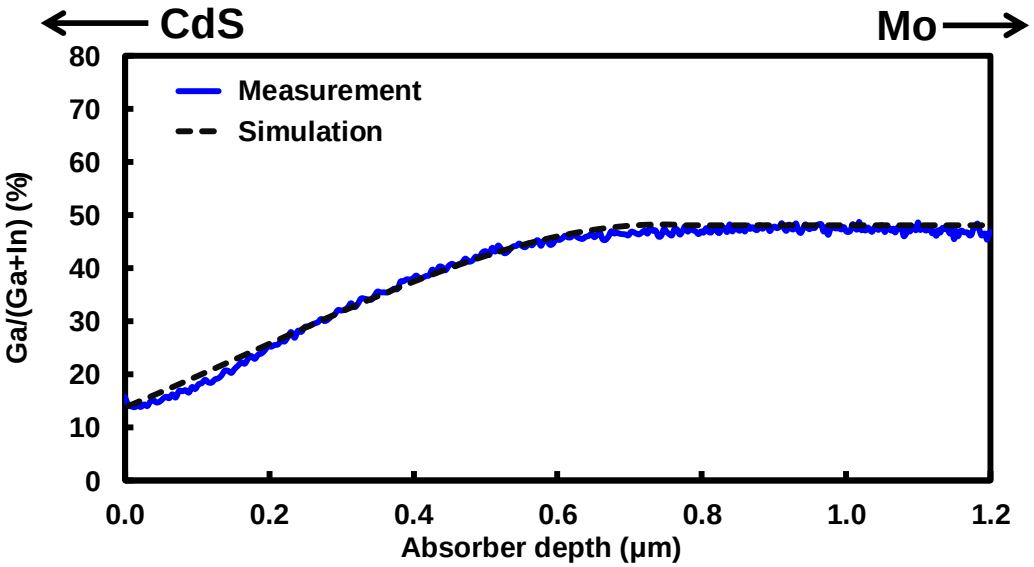

Fig. 3-9. Comparison of GGI the measured and simulated GGI depth profiles.

Table 3-II. Physical parameters for numerical simulation of Se-free CIGS solar cells.

Parameter	i-ZnO	CdS	Se-free CIGS
W (μm)	0.2	0.04	1.78
Eg (eV)	3.37	2.42	1.53-2.05
χ (eV)	4.50	4.20	4.27-4.55
ε_r	8.49	10.0	10.35-10.95
N_A (cm^{-3})	-	-	$1.6x10^{16}$
N_D (cm^{-3})	$5.0x10^{18}$	$9.0x10^{17}$	-
N_c (cm^{-3})	$2.95x10^{18}$	$2.24x10^{18}$	$1.41x10^{18}$-$1.59x10^{18}$
N_v (cm^{-3})	$1.14x10^{19}$	$1.80x10^{19}$	$2.16x10^{19}$-$3.58x10^{19}$
Defect (cm^{-3})	-	-	$1.0x10^{12}$-$5x10^{17}$
μ_e ($cm^2/V*s$)	100	100	100
μ_h ($cm^2/V*s$)	25	25	25

3.4.3 Effects of Ga grading

Figure 3-10 shows a comparison between two simulated GGI depth profiles for an absorber. Simulation 1 was calculated on the basis of the experimental results; it is the same GGI depth profile as that shown in Fig. 3-9. By contrast, Simulation 2 was conducted on the basis of an ideal GGI depth profile in a Se-free CIGS absorber to investigate the effects of Ga grading. Thus, Simulation 2 shows a lower GGI ratio at the surface and a steeper GGI depth-profile grading than Simulation 1.

The result of this comparison is given in Fig. 3-11. Compared with Simulation 1, all of the electric parameters are drastically improved in Simulation 2. These improvements are attributed to the benefits of a low Ga composition at the surface and to Ga grading of the bulk in the absorber. The experimental results in Fig. 3-12 and Fig. 3-13 confirm the validity of the simulations.

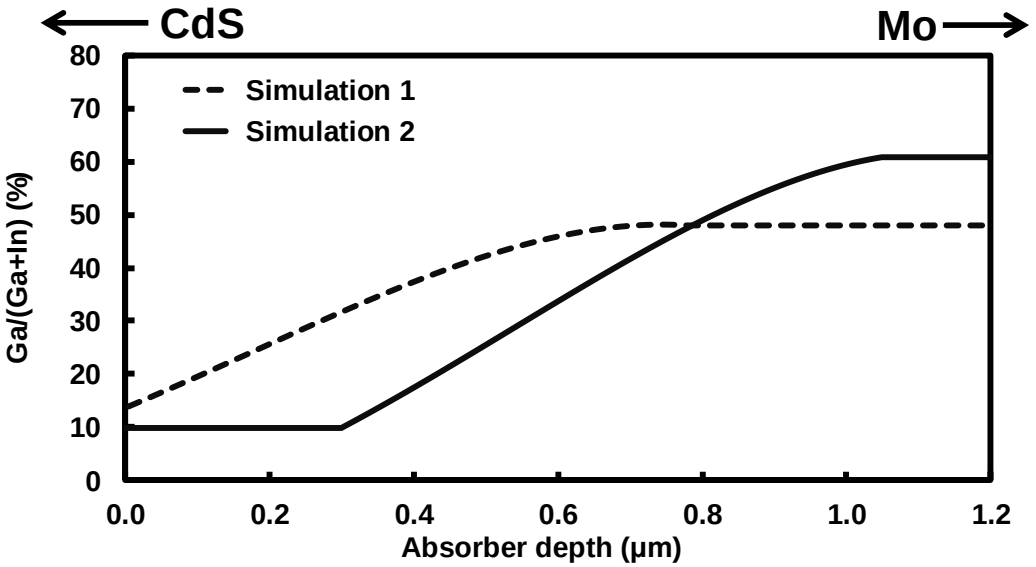

Fig. 3-10. Comparison of the GGI depth profiles between two simulations. Simulation 2 shows a lower GGI ratio at the surface and steeper GGI depth profile grading in the absorber.

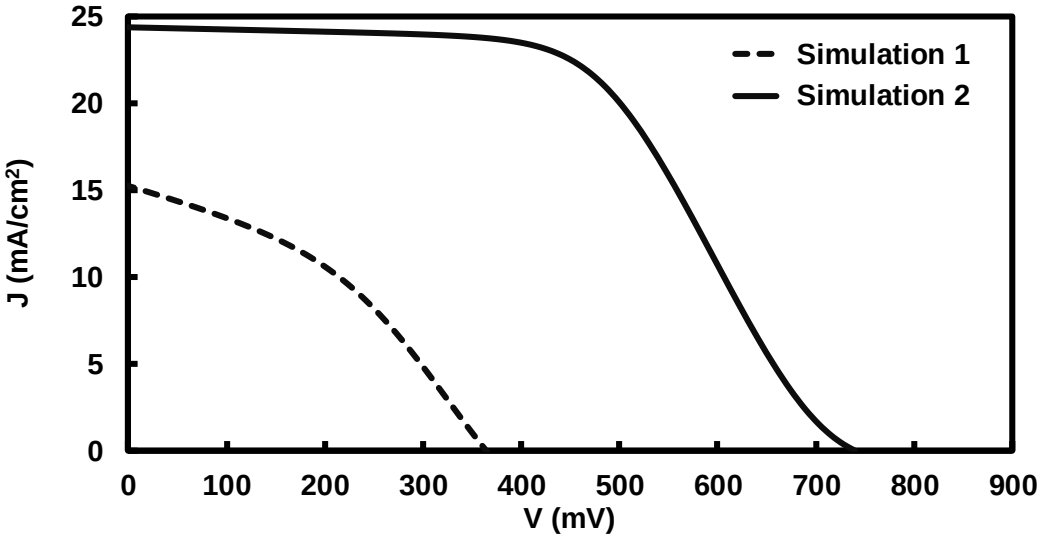

Fig. 3-11. Comparison of the *J–V* curves between two simulations. All of the electric parameters were drastically improved in Simulation 2.

In the experiments, absorbers with several different Ga depth profiles were fabricated via modification of the Ga content of the precursors and control of the sulfurization time. In Fig. 3-12, the GGI depth-profiles of four absorbers are shown. The GGI ratio was calculated from the results of GD-OES and ICP-AES analyses. Additionally, *J*–*V* and EQE characteristics of each sample are given in Fig. 3-13 and Fig. 3-14, respectively. The electrical parameters of the four cells fabricated under different conditions are also presented in Table 3-III.

The four absorbers demonstrate different Ga depth profiles. Sample A shows a high GGI ratio of 15% at the surface compared with the others ($5 \leq \mathrm{GGI} \leq 10\%$); in addition, its depth-profile gradient is gentle. Sample B shows a low GGI ratio at the surface; however, like the Ga grading in sample A, that in sample B is gentle. Sample C shows an improved GGI ratio at the surface and an improved GGI gradient. Sample D has a fine-tuned Ga depth-profile with a lower GGI ratio of 5% at the surface and a steeper Ga grading compared with the other samples.

Both Fig. 3-13 and Table 3-III show a clear dependence of the cell performance on the Ga grading scheme. The *Eff* of sample A was low, which we attributed to its poor electrical parameters. It is assumed that its poor performance was caused by a high GGI ratio at the surface and a gentle Ga grading of its absorber. For sample B, the cell performance improved to an *Eff* of 5% from 2% because of the low Ga composition at the surface. Sample C showed a further improvement in the *Eff* as a result of the V_{oc} improvement resulting from the increase of the Ga content toward the back surface (on the Mo back electrode side). Finally, sample D shows the best *Eff* of greater than 10% because of the drastic improvements of the open-circuit voltage (V_{oc}) and the short-circuit current density (J_{sc}). In the case of the J_{sc}, the long-wavelength region of

EQE was improved, as shown in Fig. 3-14. (The short-wavelength of EQE of sample D was degraded because its CdS buffer layer was accidentally made thicker than the others.) Thus, the benefits of low Ga composition at the surface and Ga grading toward the back surface from the front surface (on the CdS buffer side) have been experimentally elucidated; moreover, the simulation results shown in Fig. 3-10 and Fig. 3-11 have been validated.

On the basis of the aforementioned results regarding the Ga depth profile on Se-free CIGS solar cells, we speculated that a low GGI ratio on the surface trends to reduce Ga_{Cu} defects and that a steep Ga grading can accelerate the electrons toward the space-charge region. Hence, Ga grading is assumed to enhance the J_{sc} and the V_{oc}. However, the reason why the fill factor (*FF*) was improved because of the Ga grading is not clear. However, it is speculated that it was likely caused by a change in the conduction-band offset (CBO) at the p-n junction interface between the CdS buffer layer (n-type) and the Se-free CIGS absorber layer (p-type). The details of the CBO at the p-n junction interface are described in Chapter 4.

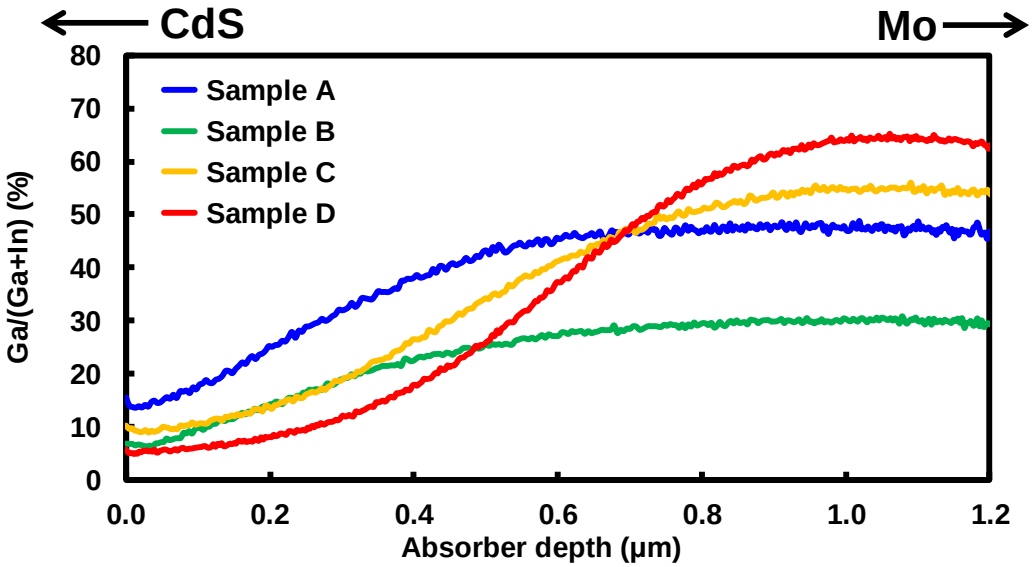

Fig. 3-12. GGI depth-profiles of four Se-free CIGS absorbers fabricated under different conditions. (© 2015 IEEE.)

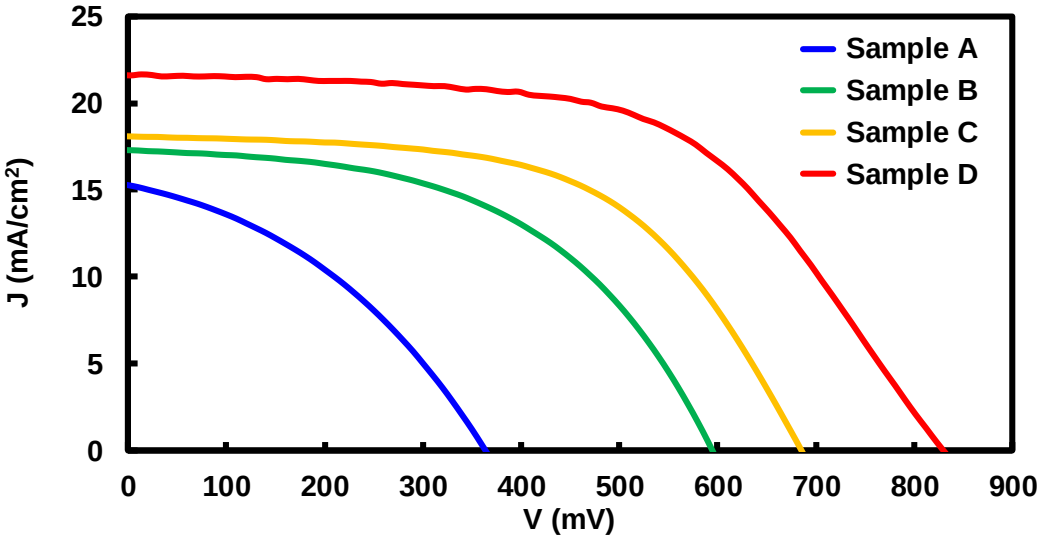

Fig. 3-13. Comparison of the *J–V* curves of four different samples fabricated with each absorber. (© 2015 IEEE.)

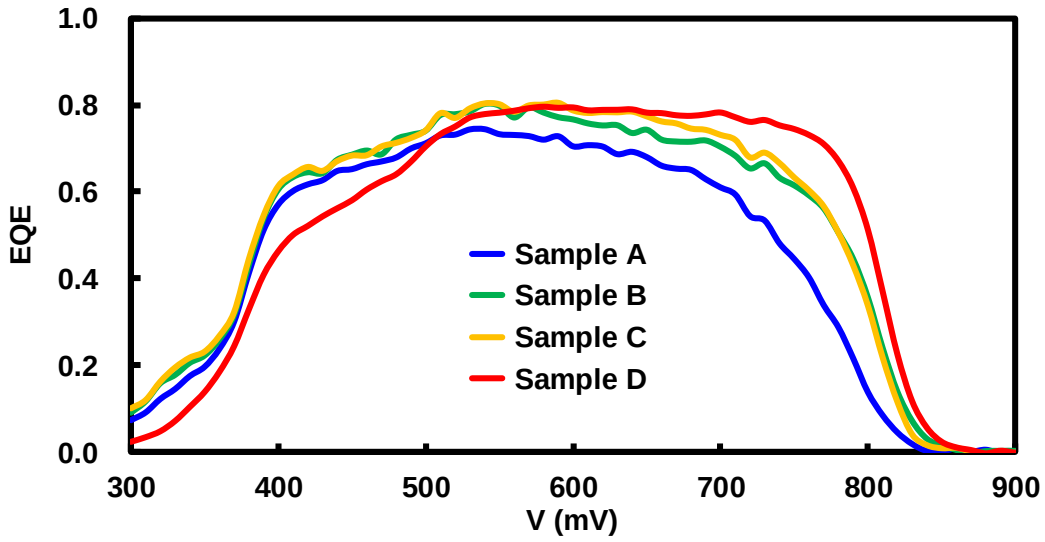

Fig. 3-14. Comparison of the EQE characteristics of four different samples fabricated with each absorber. (© 2015 IEEE.)

Table 3-III. Electric parameters of different Ga depth-profile Se-free CIGS solar cells.

Sample	Ga contents		Electrical parameters			
-	Surface	Grading	Eff (%)	V_{oc} (mV)	J_{sc} (mA/cm^2)	FF (%)
A	High	Gentle	2.09	363	15.2	37.8
B	Low	Gentle	5.22	595	17.3	50.7
C	Low	Steep	7.05	686	18.1	56.9
D	Lower	Steeper	10.2	830	21.6	56.9

3.4.4 Optimization of Ga depth profile

In this section, the benefits of sulfurization on Se-free CIGS by rapid thermal annealing (RTA) are discussed. Generally, RTA is used for sulfurization to shorten the fabrication process. However, in this thesis, RTA is found to be effective not only for shortening the process but also for controlling the Ga depth profile in Se-free CIGS absorbers. Figure 3-15 shows the dependence of the ramp rate on the electrical parameters of the Se-free CIGS solar cells. Higher ramp rates clearly contributed to the enhancement of cell performance. It is assumed that the higher ramp rate results in a low Ga content at the surface of the absorber and in superior Ga grading from the front side toward the back side.

Fig. 3-16 shows the Ga depth profile of samples prepared under various ramp rates (20, 40, and 140°C/min), as obtained from the GD-OES analysis. Absorbers with various ramp rates clearly show different Ga depth profiles. The absorber fabricated with a ramp rate of 20°C/min shows a high Ga/(Ga+In) ratio of 15% at the surface compared with the other samples. In addition, its depth profile shows a more gradual gradient. The absorber fabricated at 40°C/min shows a low Ga/(Ga+In) ratio at the surface. However, the Ga grading is less steep than that in the absorber fabricated at a ramp rate of 140°C/min. In the absorber fabricated at a ramp rate of 40°C/min, both the Ga/(Ga+In) ratio at the surface and its gradient were improved. The *Eff* of the sample fabricated at a ramp rate of 20°C/min is low because of its very poor electrical parameters. The poor electrical parameters are possibly caused by the high Ga/(Ga+In) ratio at the surface and the gradual Ga grading of the absorber. For the sample processed with a ramp rate of 40°C/min, the *Eff* improves to ~14% from ~8% because of the low Ga composition at the surface. The sample with 140°C/min boosted the *Eff* further because of the

improvements of the V_{oc} and J_{sc}, which are attributed to the increased Ga content toward the back surface from the front surface. Finally, the best cell demonstrated an *Eff* of 15.2%. Thus, the benefits of a low Ga composition at the surface and a high Ga grading at the back surface have been brought to light. According to these results, the Ga depth profile can not only be controlled via the Ga composition or sulfurization time control (as explained in section 3.4.3) but also via fine-tuning of the temperature ramp rate during sulfurization.

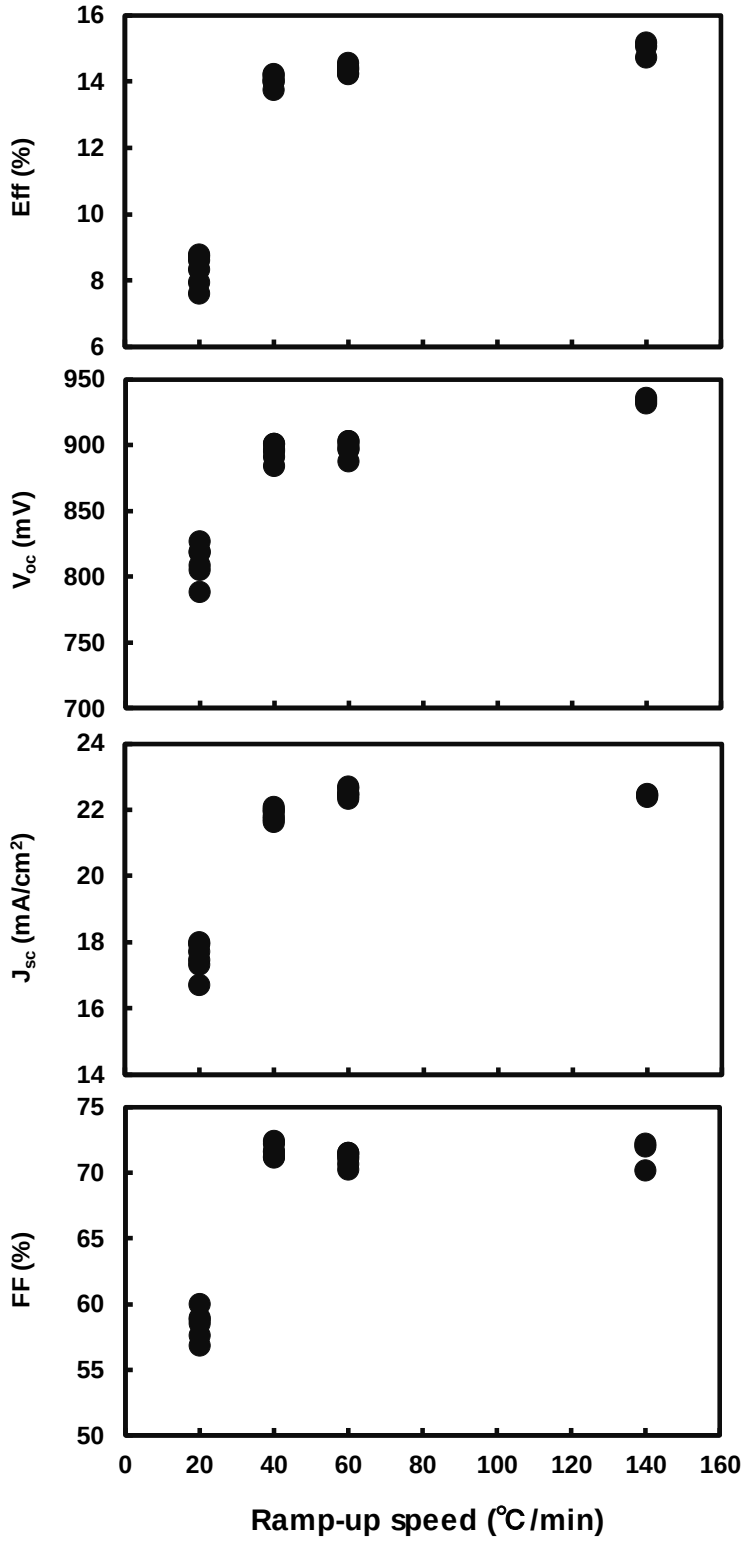

Fig. 3-15. Dependence of the temperature ramp rate during sulfurization on the electrical parameters of the Se-free CIGS solar cells.

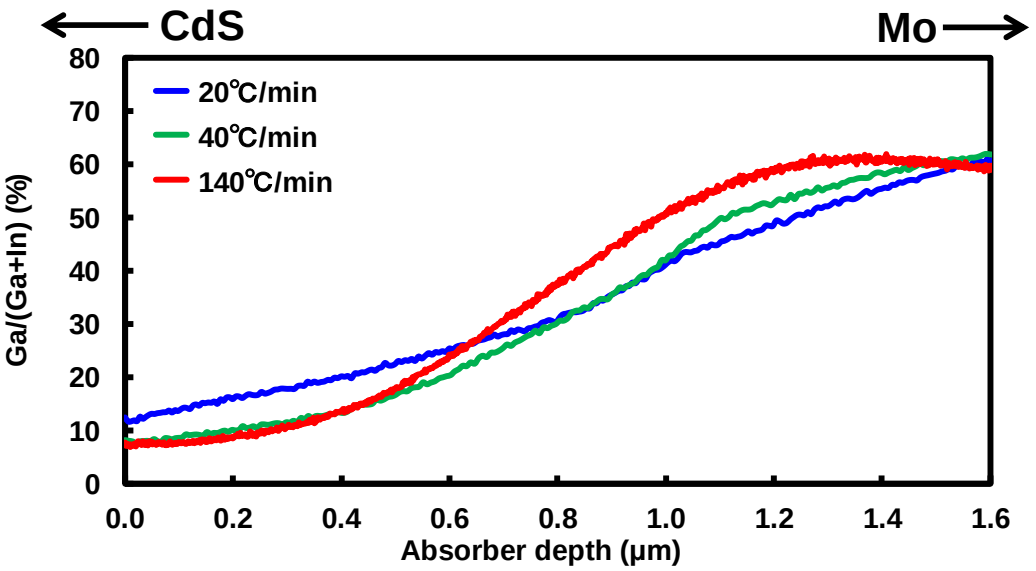

Fig. 3-16. Dependence of the temperature ramp rate during sulfurization on the GGI ratio of Se-free CIGS absorbers.

3.5 Minority carrier lifetime

As the last part of this chapter, the minority carrier lifetime of a Se-free CIGS absorber is discussed. It was measured by time-resolved photoluminescence (TRPL) as a gauge to evaluate the absorber quality. In the TRPL measurements, a fast laser pulse injects excess electrons and holes into the p-type absorber layer and the resulting luminescence is tracked as a function of time. In this thesis, the measurements were performed at room temperature, using a pulsed laser with a wavelength of 532 nm and an excitation power of 4.67 mW (excitation intensity of approximately 595 mW/cm^2). Fig. 3-17 shows the TRPL lifetime of the Se-free absorber with a large crystal size and a Ga grading, as fabricated by optimized sulfurization. Although this absorber exhibited a high *Eff*, its lifetime was merely 0.97 ns. This short lifetime indicates that further room exists for improving the Se-free CIGS absorbers.

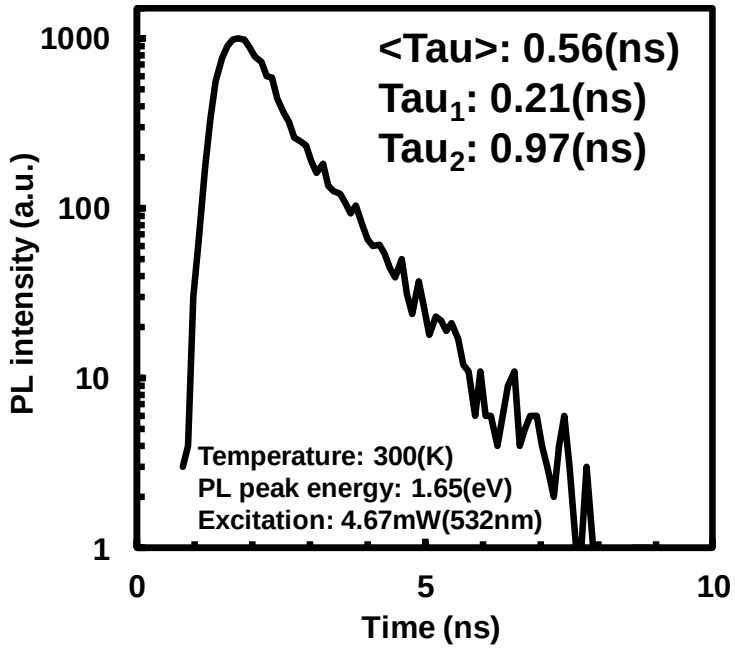

Fig. 3-17. TRPL lifetime of Se-free CIGS absorber. (© 2016 IEEE.)

3.6 Chapter summary

In this chapter, the Se-free CIGS absorber and optimization of the fabrication process were both investigated from the viewpoint of Cu-poor composition, crystal growth, Ga depth profile and minority carrier lifetime. As a result, a KCN-free process was developed using a Cu-poor absorber (without a CuS secondary layer) made from a Cu-poor precursor; in addition, crystal growth of the Cu-poor absorber was accomplished via high-temperature sulfurization. Furthermore, the impact of the Ga depth profile on the Se-free CIGS absorber was revealed from simulated and experimental results. The results also showed that RTA could control the Ga grading, and the *Eff* was increased to 15.2% through optimization of the absorber. Finally, the minority carrier lifetime of the Se-free CIGS absorber was evaluated by TRPL measurements, which indicated a short lifetime of less than 1 ns; however, this short lifetime indicated that room exists for further improving the Se-free CIGS absorbers. It indicates that an *Eff* greater than 16% is feasible on a Se-free CIGS solar cell after optimization of other layers such as the n-type buffer, i-ZnO, and transparent conductive oxide layers. Regarding the n-type buffer layer, details are presented in the next chapter.

References

[1] R. Kaigawaa, A. Neisser, R. Klenk, M.-Ch. Lux-Steiner, *Thin Solid Films.* **415** (2002) 266-271.

[2] R. Klenk, S. Bakehe, R. Kaigawa, A. Neisser, J. Reis, M. Ch. Lux-Steiner, *Thin Solid Films.* **451-452** (2004) 424-429.

[3] I. Riedel, J. Riediger, J. Ohland, J. Keller, M. Knipper, J. Parisi, R. Mainz, S. Merdes, *Sol. Energy Mater. Sol. Cells* 95 (2011) 270-273.

[4] S. J. Park, Y. Cho, S. H. Moon1, J. E. Kim, D. Lee, J. Gwak, J. Kim, D. Kim, B. K. Min, *J. Phys. D: Appl. Phys.* **47** (2014) 135105 (7pp).

[5] S. Merdes, R. Mainz, J. Klaer, A. Meeder, H. Rodriguez-Alvarez, H. W. Schock, M. C. Lux-Steiner, R. Klenk, *Sol. Energy Mater. Sol. Cells* **95** (2011) 864-869.

[6] S. Merdes, D. Abou-Ras, R. Mainz, R. Klenk, M. C. Lux-Steiner, A. Meeder, H. W. Schock, J. Klaer, *Prog. Photovolt: Res. Appl.* **21** (2013) 88-93.

[7] E. W. Hurst, *Aust. J. Exp. Biol. Med. Sci.* **20** (1942) 297-312.

[8] J. Emsley, *Oxford University Press*, "The Elements of Murder" (2005) 187.

[9] T. Dullweber, G. Hanna, W. Shams-Kolahi, A. Schwartzlander, M. A. Contreras, R. Noufi, H. W. Schock, *Thin Solid Films*, **361-362** (2000) 478-481.

[10] S. Schleussner, U. Zimmermann, T. Wätjen, K. Leifer, M. Edoff, *Sol. Energy Mater. Sol. Cells* 95 (2011) 721-726.

[11] R. Kotipalli, B. Vermang, V. Fjällström, M. Edoff, R. Delamare, D. Flandre, *Phys. Status Solidi RRL* **9** (2015) 157-160.

[12] M. Burgelman, P. Nollet, S. Degrave, *Thin Solid Films.* **361-362** (2000) 527-532.

[13] H. T. Tung, I. G. Chen, J. M. Song, M. G. Tsai, I. M. Kempson, G. Margaritondod,

Y. Hwu, *Nanoscale* **5** (2013) 4706-4710.

4

$Zn_{1-x}Mg_xO$ as a Cd-free buffer layer material

4.1 Introduction

In the previous chapter, the development of a p-type Se-free $Cu(In,Ga)S_2$ (CIGS) absorber layer without KCN etching was discussed from the viewpoint of environmental friendliness and low cost. As with KCN, Cd is also well known for its toxicity [1,2]. However, Cd-based compounds, especially CdS, are commonly used for n-type buffer layers on Se-free CIGS absorber layers to form a p-n junction because it can cover the rough surface of the absorber [3,4]. To prevent shunt passes at the interface of the p-n junction, CdS is suitable as an n-type buffer layer; moreover, a thicker CdS buffer layer enhances the conversion efficiency (*Eff*) because of the improvement of the open-circuit voltage (V_{oc}) and fill factor (*FF*). However, a thicker CdS buffer layer decreases the short-circuit current density (J_{sc}) because of its low transparency. Thus, an alternative buffer layer is needed that involves no harmful substances and that improves the trade-off relationship. In this thesis, $Zn_{1-x}Mg_xO$ is focused as an alternative buffer layer to CdS. An experimental evaluation of the CdS buffer layers on Se-free CIGS absorber layers is presented, followed by an evaluation of the ability of a $Zn_{1-x}Mg_xO$ buffer layer to boost cell performance.

4.2 CdS buffer layer

4.2.1 Chemical bath deposition

Chemical bath deposition (CBD) is one of the best known methods to deposit CdS buffer layers for Cu(In,Ga)(Se,S)$_2$ (CIGSeS)-based solar cells, although CdS can be formed by many different methods, including spray, sputtering, and evaporation [5-8]. The films of CdS are prepared via CBD by decomposition of thiourea (SC(NH$_2$)$_2$) in an aqueous ammonia solution (NH$_4$OH) containing a cadmium salt such as CdSO$_4$, CdCl$_2$, Cd(CH$_3$COO)$_2$, or Cd(NO$_3$)$_2$. In this thesis, all of the CdS buffer layers were fabricated by CBD with NH$_4$OH solution containing SC(NH$_2$)$_2$ and CdSO$_4$. The typical CdS layer grows the through reaction with sulfide ions extracted from the SC(NH$_2$)$_2$ complex in the solution by the following reactions:

$$CdSO_4 + SC(NH_2)_2 + NH_4OH + H_2O \rightarrow [Cd(NH_3)_4]^{2+} + SC(NH_2)_2 + 2OH^-. \quad (4\text{-}1)$$

$$[Cd(NH_3)_4]^{2+} + SC(NH_2)_2 + 2OH^- \rightarrow CdS\downarrow + 4NH_3 + CH_2N_2 + 2H_2O. \quad (4\text{-}2)$$

The thickness of the CdS layer is controlled by the solution temperature and the deposition time. Their ranges were approximately 45–85°C and 2–20 min in this experiment. As a result, the thickness of the CdS buffer layer could be controlled in the range from 20 to 120 nm.

4.2.2 Dependence of electrical parameters on thickness

CdS buffer layers with different thickness were deposited onto Se-free CIGS absorber layers; the dependence of the electrical parameters on the CdS thickness for Se-free CIGS solar cells is given in this section. Specifically, CdS layers with five different thicknesses (30, 40, 50, 80, and 115 nm) were compared with each other. As shown in Fig. 4-1, in the range from 30 to 50 nm, the thicker CdS buffer layer improves the *Eff* because of the enhanced V_{oc} and *FF*. It is supposed that the coverage ratio was improved. However, CdS layers thicker than 50 nm resulted in a decrease of the *Eff*. In this case, it is assumed that excessively thick buffer layers caused high series resistance (*Rs*) and that extension deposition times cause the interdiffusion of metals between the absorber and buffer layers. Thicker CdS layers also resulted in lower J_{sc} values in all of the investigated thickness ranges, without exception. To confirm the reason for the J_{sc} degradation, the external quantum efficiency (EQE) characteristics of each best *Eff* cell on five Se-free CIGS solar cells with different CdS thicknesses were measured. Fig. 4-2 shows a comparison of the normalized EQE among various CdS thickness and indicates an absorption loss at the short-wavelength region in the case of thicker CdS buffer layers. On the basis of these results, the best thickness of the CdS buffer layer for the Se-free CIGS solar cells should be 50 nm. Thus, the optimum CdS buffer layer further enhanced the *Eff* of the Se-free CIGS solar cell.

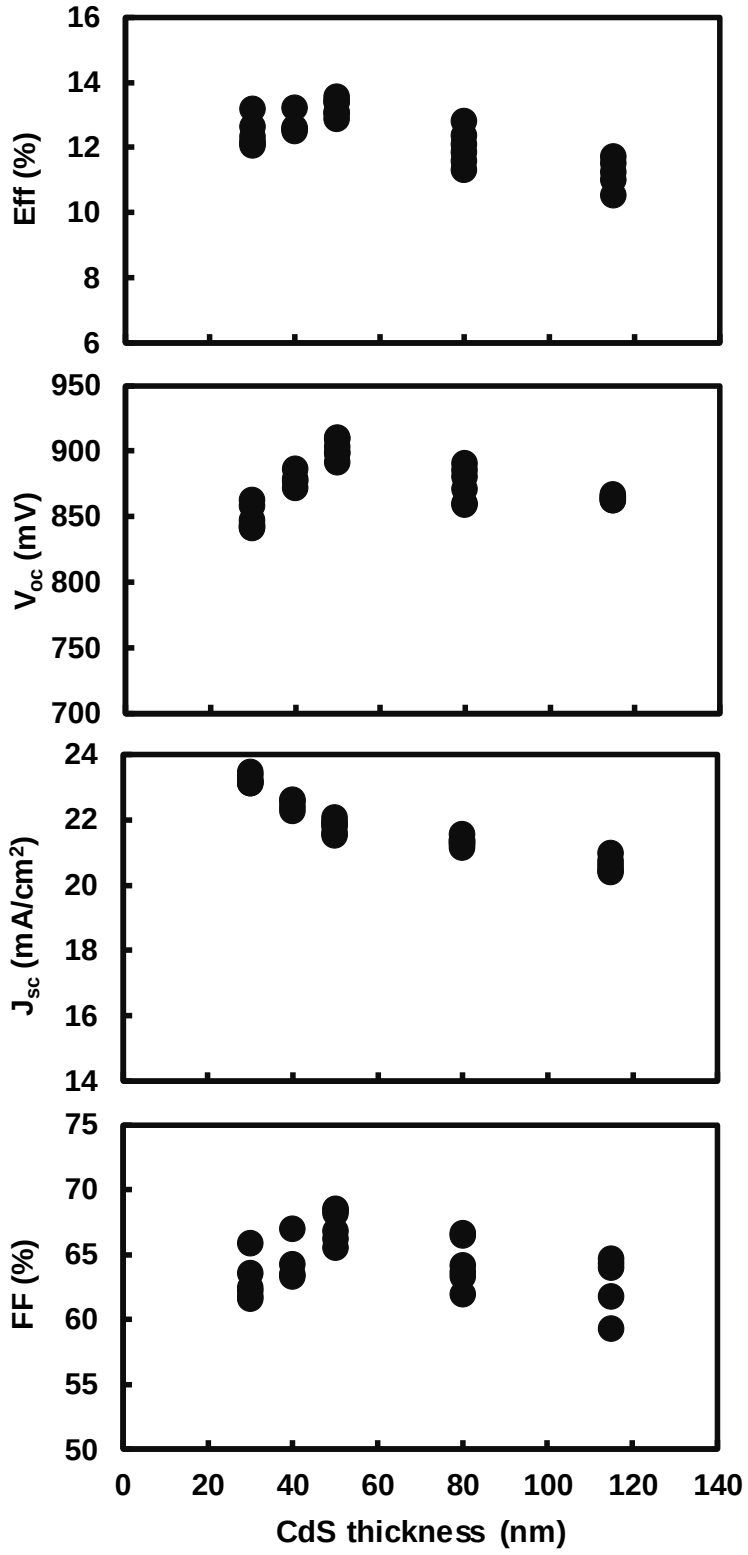

Fig. 4-1. Dependence of electrical parameters on the CdS buffer layer thickness.

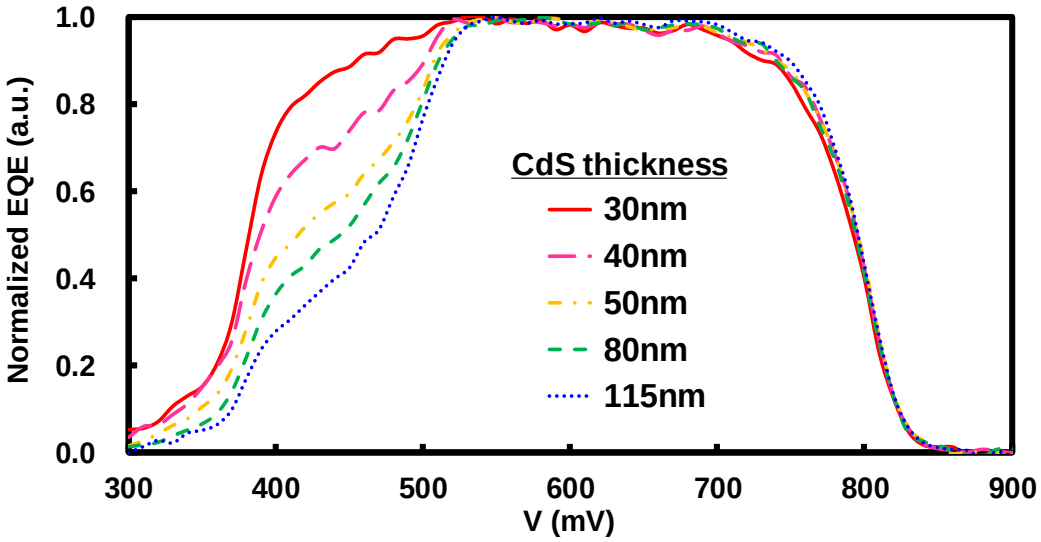

Fig. 4-2. Comparison of normalized EQE among five different CdS thicknesses.

Scanning electron microscopy (SEM) and energy-dispersive X-ray spectrometry (EDX) images of a cross-section of a Se-free CIGS solar cell with an optimized CdS buffer layer are displayed in Fig. 4-3. They indicate that the surface of the absorber layer is still rough even though it was improved by high-temperature sulfurization (see Fig. 3-5 in Chapter 3); however, these images also show that the CdS buffer layer covers the whole of the surface of the absorber. Figure 4-4 shows (a) *J*–*V* and (b) EQE characteristics of a Se-free CIGS solar cell with an optimized CdS buffer layer. The V_{oc} and *FF* were both improved because of the good coverage of the CdS buffer layer; the *Eff* consequently reached 15.7%.

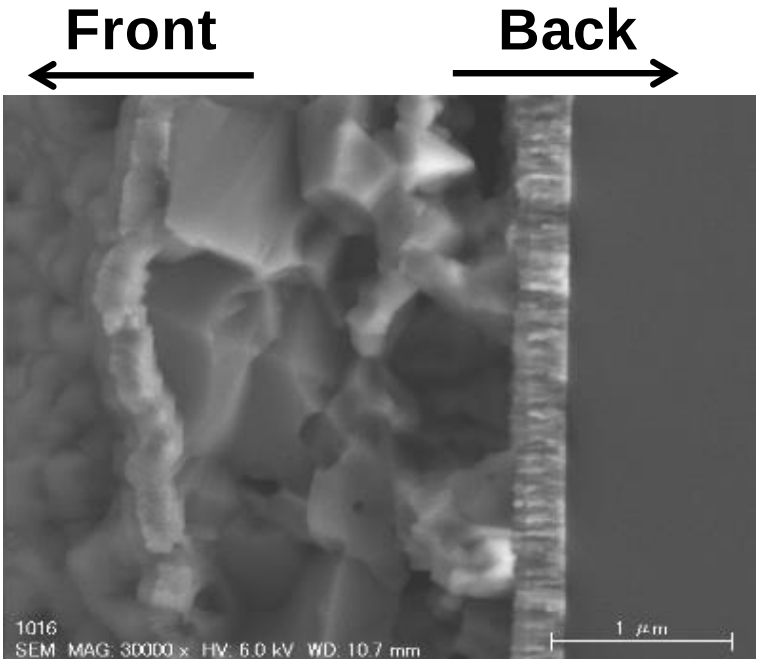

(a)

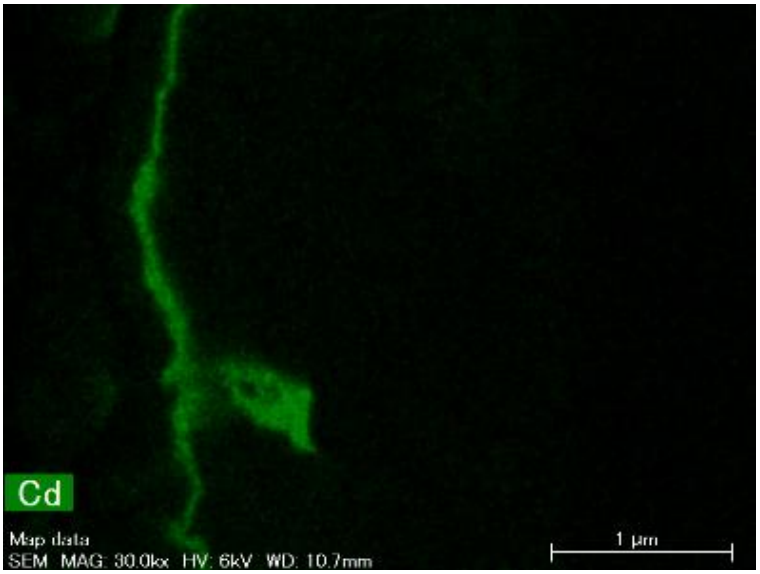

(b)

Fig. 4-3. (a) SEM image and (b) EDX Cd-mapping image of a cross-section of a Se-free CIGS solar cell.

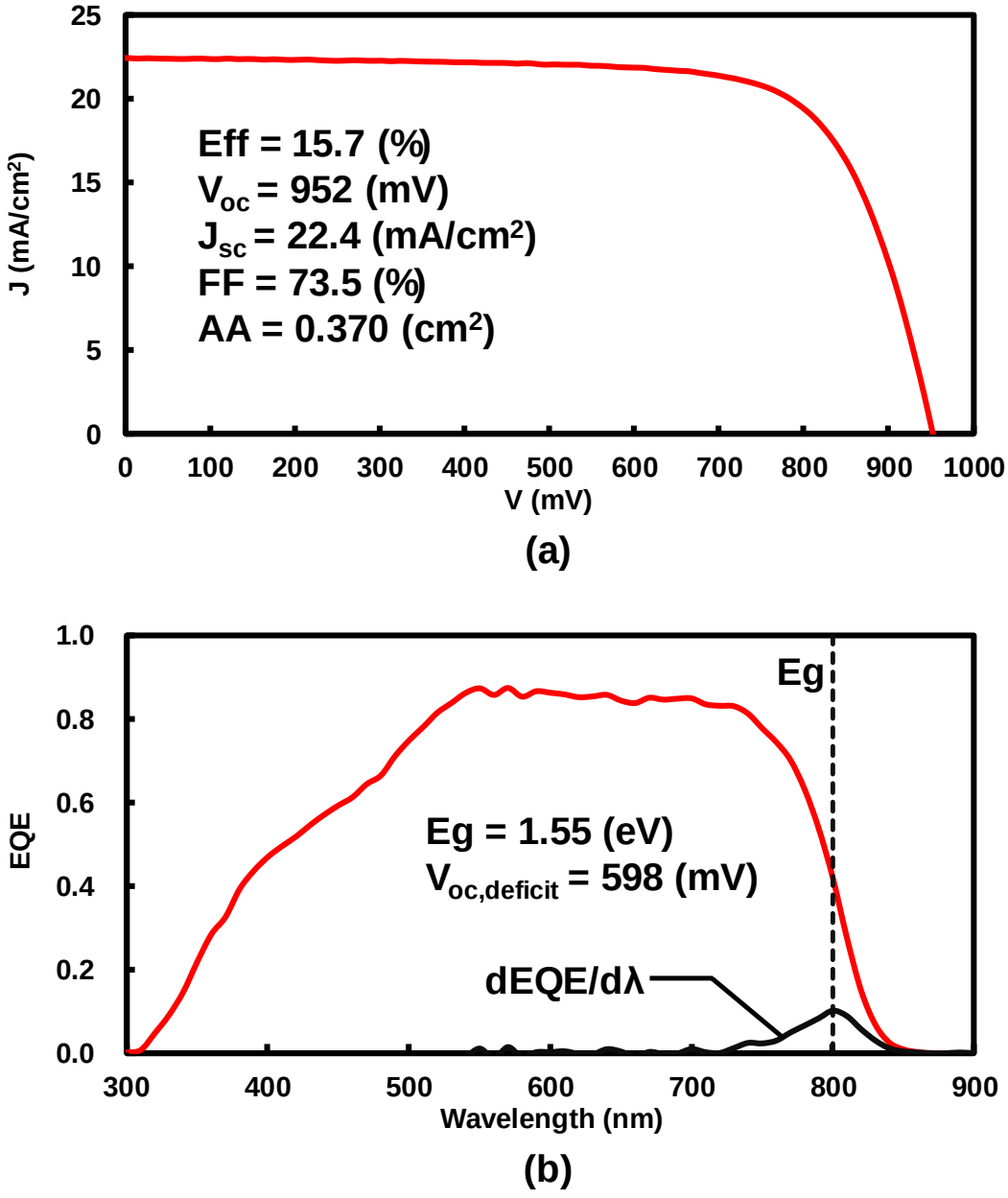

Fig. 4-4. (a) *J*–*V* and (b) EQE characteristics of a Se-free CIGS solar cell with an optimized CdS buffer layer.

4.3 $Zn_{1-x}Mg_xO$ buffer layer

4.3.1 Atomic layer deposition

Atomic layer deposition (ALD) is used to fabricate thin-film layers because of its high level of control and uniform material deposition. The ALD technique has been introduced into photovoltaic applications, especially for depositing buffer layers such as ZnO, MgO, $Zn_{1-x}Mg_xO$, $ZnO_{1-x}S_x$, and ZnSnO. In this study, ZnO and $Zn_{1-x}Mg_xO$ layers were used as the intrinsic and n-type buffer layers on a Se-free CIGS absorber. In this section, the $Zn_{1-x}Mg_xO$ buffer layer is mainly discussed as a Cd-free alternative buffer layer to enhance the *Eff* of Se-free CIGS solar cells compared with the *Eff* achieved with a CdS buffer layer.

$Zn_{1-x}Mg_xO$ layer was deposited by ALD with $(C_2H_5)_2Zn$, $(C_2H_5C_5H_4)_2Mg$ and H_2O. It grows by reacting with ZnO and MgO compounds via the following reactions:

$$(C_2H_5)_2Zn + (C_2H_5C_5H_4)_2Mg + H_2O \rightarrow ZnO + MgO \rightarrow Zn_{1-x}Mg_xO. \quad (4\text{-}3)$$

Both the thickness and the Mg content of the $Zn_{1-x}Mg_xO$ layer are controlled by the count and ratio of $(C_2H_5)_2Zn/N_2/H_2O/N_2$ cycles (for ZnO) and $(C_2H_5C_5H_4)_2Mg/N_2/H_2O/N_2$ cycles (for MgO). In the ALD process, both the thickness and the Mg content, which is defined according to the Mg/(Zn+Mg) ratio, are easily controlled in an excellent manner. The thickness of the $Zn_{1-x}Mg_xO$ buffer layer was approximately 40 nm; in addition, the range of Mg content was $0.1 \leq x \leq 0.5$ in these experiments.

4.3.2 Effects of a wide bandgap

To further improve the J_{sc}, a $Zn_{1-x}Mg_xO$ buffer layer, which exhibits higher transparency than a CdS buffer layer, was used [9]. Fig. 4-5 (a) shows a comparison of the *J–V* characteristics in the Se-free CIGS solar cells with CdS and with $Zn_{1-x}Mg_xO$ buffer layers. The $Zn_{1-x}Mg_xO$ buffer cell demonstrates a higher J_{sc} than the CdS buffer cell. In Fig. 4-5 (b), the $Zn_{1-x}Mg_xO$ buffer layer increases the EQE in the short-wavelength region. The $Zn_{1-x}Mg_xO$ buffer layer is superior to the CdS buffer layer from the viewpoint of environmental and technical requirements for Se-free CIGS solar cells.

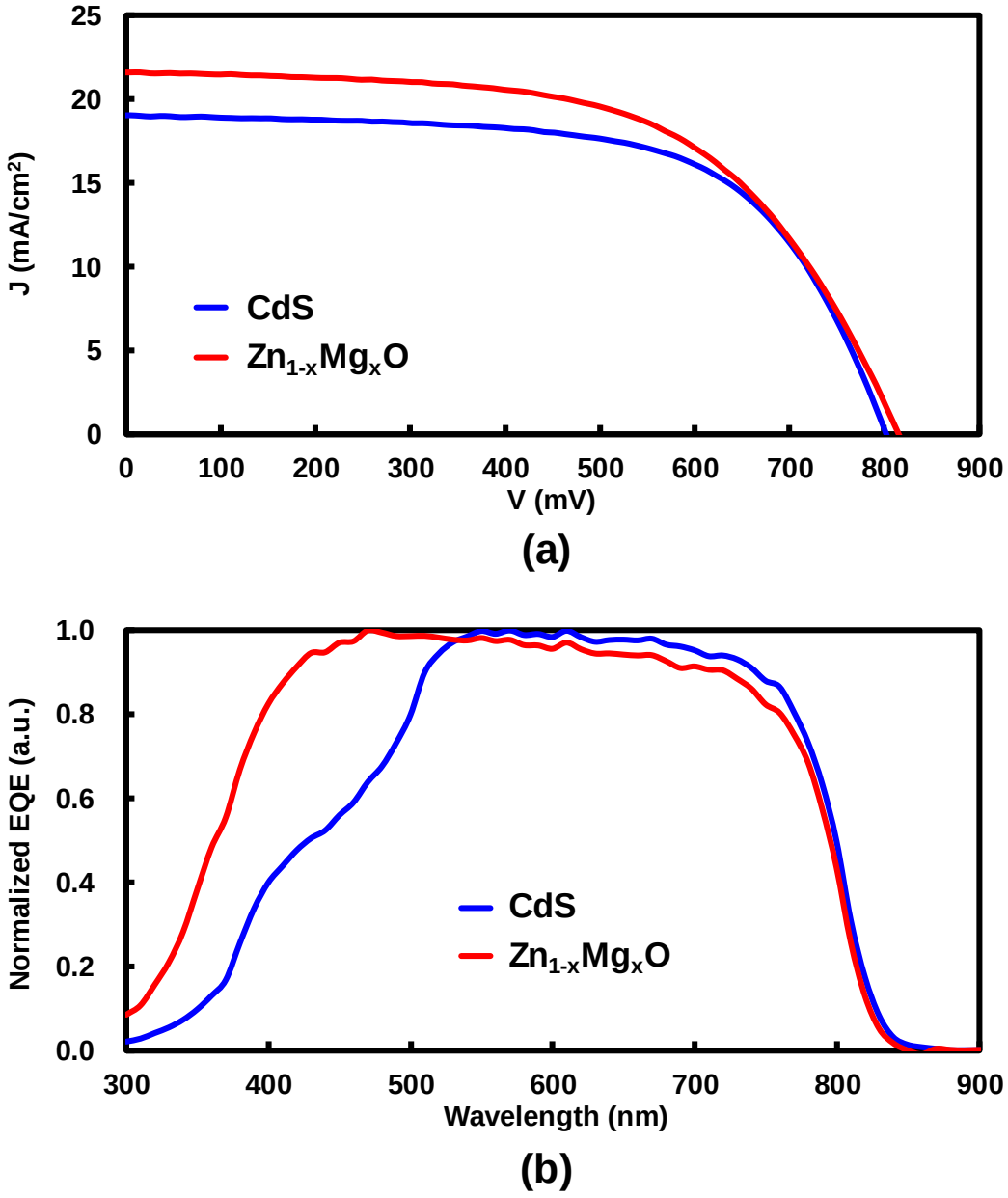

Fig. 4-5. Comparison of (a) the *J*–*V* characteristics and (b) the normalized EQE in the Se-free CIGS solar cells with CdS and with $Zn_{1-x}Mg_xO$ buffer layers.

4.3.3 Dependence of electrical parameters on the Mg content

Although the J_{sc} was improved by the use of a $Zn_{1-x}Mg_xO$ buffer layer, the V_{oc} was still low. The low V_{oc} might be caused by a mismatch of the band offset, especially the conduction band offset (CBO), at the interface of the p-n junction between the absorber and buffer layers. The *Eg* of the $Zn_{1-x}Mg_xO$ buffer layer is known to be controllable via the Mg/(Zn+Mg) ratio [9]. To improve the band offset mismatch, the CBO was adjusted by increasing the Mg content in the $Zn_{1-x}Mg_xO$ buffer layer. In this section, two samples (sample A and sample B) were prepared for comparison; the Zn and Mg contents in these $Zn_{1-x}Mg_xO$ buffer layers were measured by ICP-AES. As shown in Table 4-I, sample B contains less Zn and more Mg compared with sample A. Thus, the relative amount of Mg in the $Zn_{1-x}Mg_xO$ buffer layer, as defined by Mg/(Zn+Mg) was greater. On the basis of this result, sample A and B are represented as $Zn_{1-x}Mg_xO$ (x = 0.19) and $Zn_{1-x}Mg_xO$ (x = 0.24) hereafter.

Table 4-I. Zn and Mg contents in $Zn_{1-x}Mg_xO$ buffer layers.

Sample	Zn (μmol/cm^2)	Mg (μmol/cm^2)	Mg/(Zn+Mg)
A	0.569	0.136	0.193
B	0.481	0.154	0.242

Figure 4-6 shows a comparison of (a) the *J*–*V* and (b) the EQE characteristics between Se-free CIGS cells with $Zn_{1-x}Mg_xO$ (x = 0.19) and $Zn_{1-x}Mg_xO$ (x = 0.24) buffer layers. The cell with the $Zn_{1-x}Mg_xO$ (x = 0.24) buffer layer demonstrated a higher V_{oc} than the cell with the $Zn_{1-x}Mg_xO$ (x = 0.19) buffer layer and accordingly contributed to the

improvement of cell performance. The higher Mg content in the $Zn_{1-x}Mg_xO$ buffer layer modified the CBO between the absorber and buffer layers. To test this hypothesis, band-diagrams for Se-free CIGS solar cells with $Zn_{1-x}Mg_xO$ (x = 0.19) and $Zn_{1-x}Mg_xO$ (x = 0.24) buffer layers were investigated.

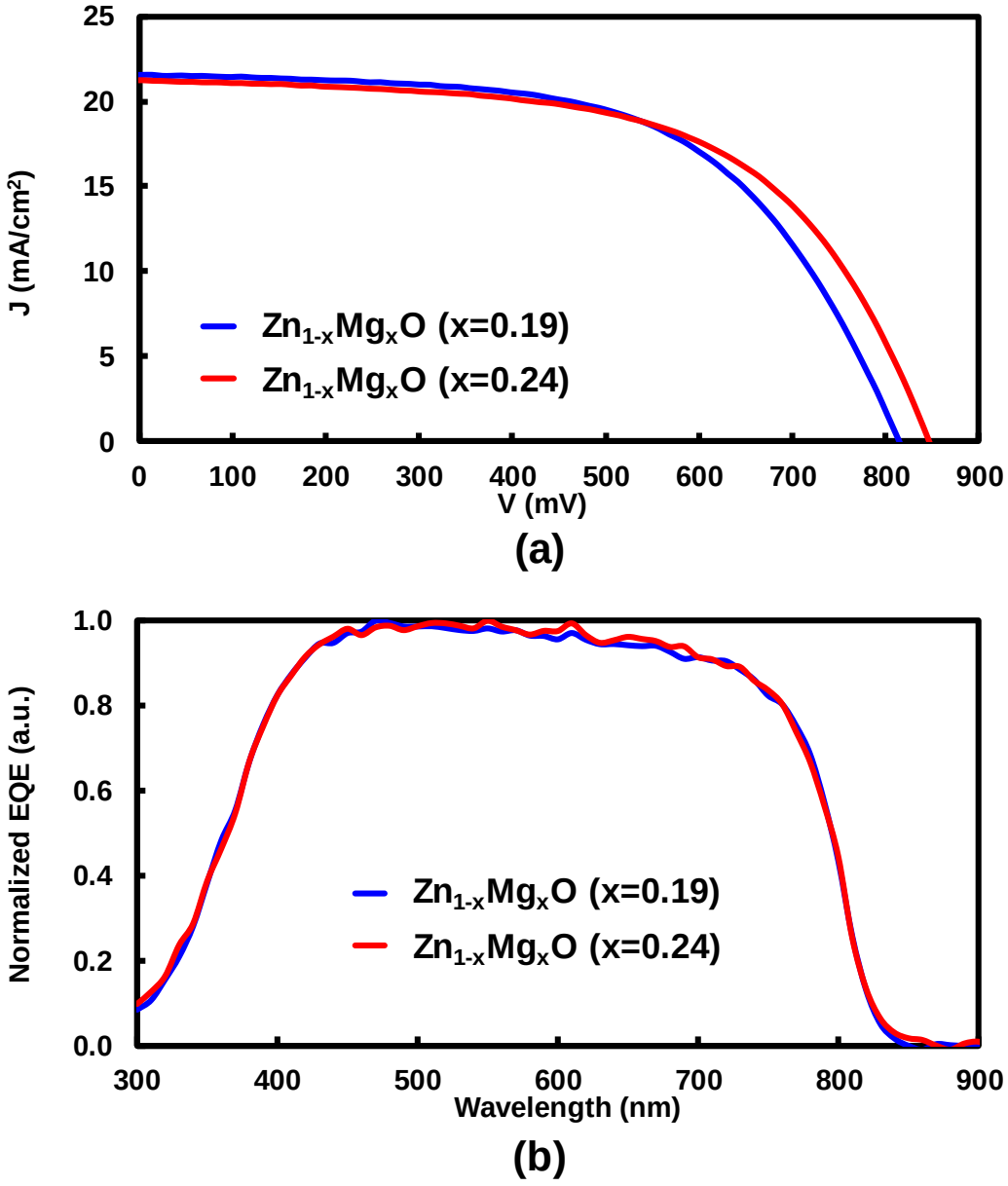

Fig. 4-6. Comparison of (a) the *J-V* and (b) the EQE characteristics in Se-free CIGS solar cells with $Zn_{1-x}Mg_xO$ (x = 0.19) and $Zn_{1-x}Mg_xO$ (x = 0.24) buffer layers.

In this study, the CBO was calculated from the valence-band maximum (VBM) and the conduction-band minimum (CBM). The VBM of the $Zn_{1-x}Mg_xO$ buffer and Se-free CIGS absorber layers was measured via ultraviolet photoelectron spectroscopy (UPS) using a He-I light source (21.22 eV) after deposition of the buffer layer. For the depth-resolved UPS measurements, an Ar^+-ion (3 kV) beam sputtering system equipped in the UPS system was used. The reference level was the Fermi level, and the calibration was performed with Au as a standard sample. The CBM of the $Zn_{1-x}Mg_xO$ (x = 0.19), $Zn_{1-x}Mg_xO$ (x = 0.24), and Se-free CIGS was estimated using *Eg* values of 3.64, 3.75, and 1.55 eV, respectively [9].

Figure 4-7 shows a comparison of the band diagrams for Se-free CIGS solar cells with $Zn_{1-x}Mg_xO$ (x = 0.19) and $Zn_{1-x}Mg_xO$ (x = 0.24) buffer layers. The $Zn_{1-x}Mg_xO$ (x = 0.24) cell shows that the CBM of the buffer layer in the vicinity of the interface can be increased compared with that in the case of the $Zn_{1-x}Mg_xO$ (x = 0.19) cell. This upward shift of CBM is potentially relevant to the V_{oc} improvement. It supports the V_{oc} enhancement of the $Zn_{1-x}Mg_xO$ (x = 0.24) cell with an improved CBO, as shown in Fig. 4-6 (a). Thus, the higher Mg content in the $Zn_{1-x}Mg_xO$ buffer layer clearly resulted in an improved *Eff* as a consequence of the enhanced V_{oc}. However, as shown in Fig. 4-7, the band-diagram of the $Zn_{1-x}Mg_xO$ (x = 0.24) buffer layer cell indicates a negative value of the CBO, which is generally called “cliff.” This cliff leaves room for improving cell performance through enhancement of the V_{oc} by modifying the CBO, especially if it is shifted to “spike,” which is a positive value of CBO, from “cliff” through control of the Mg content in the $Zn_{1-x}Mg_xO$ buffer layer.

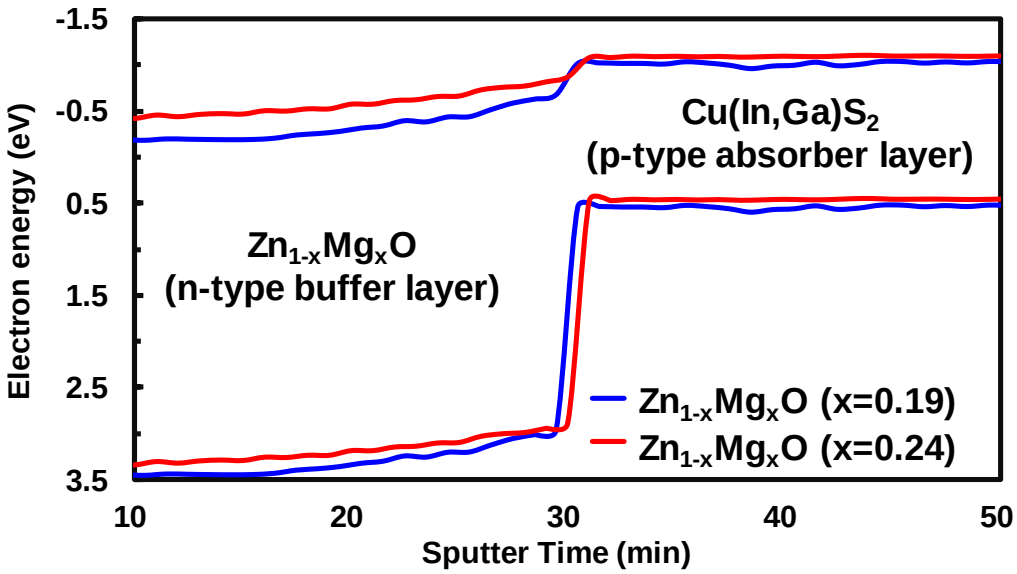

Fig. 4-7. Comparison of the band offset at the interface between the absorber and buffer layers for Se-free CIGS cells with a $Zn_{1-x}Mg_xO$ (x = 0.19) or a $Zn_{1-x}Mg_xO$ (x = 0.24) buffer layer.

For optimization of the $Zn_{1-x}Mg_xO$ buffer layer, $Zn_{1-x}Mg_xO$ compositions with $0.10 \leq x \leq 0.50$ were tested and compared with each other. Figure 4-8 shows the dependence of the Mg contents in the $Zn_{1-x}Mg_xO$ buffer layer on the electrical parameters of Se-free CIGS cells. In the range $0.10 \leq x \leq 0.30$, a higher Mg content improves the *Eff* through improvements in all of the electrical parameters, especially the V_{oc}. However, when the Mg content exceeds 0.30, particularly 0.48, the *Eff* decreases because of degradation of the J_{sc} and the *FF*. Presumably, an excessively high Mg content caused a high *Rs* because of an excessively high CBO. However, the V_{oc} was observed to increase with increasing Mg content. Thus, according to this result, a Mg content greater than 0.30 cannot be concluded to preclude further improvements in cell performance. Specifically, boosting the *Eff* to optimize the Mg content under the conditions of not only an n-type buffer layer but also other layers such as p-type absorber and i-ZnO layers is important.

On the basis of these considerations, the optimum Mg content of the $Zn_{1-x}Mg_xO$ buffer layer is in the range $0.20 \leq x \leq 0.35$.

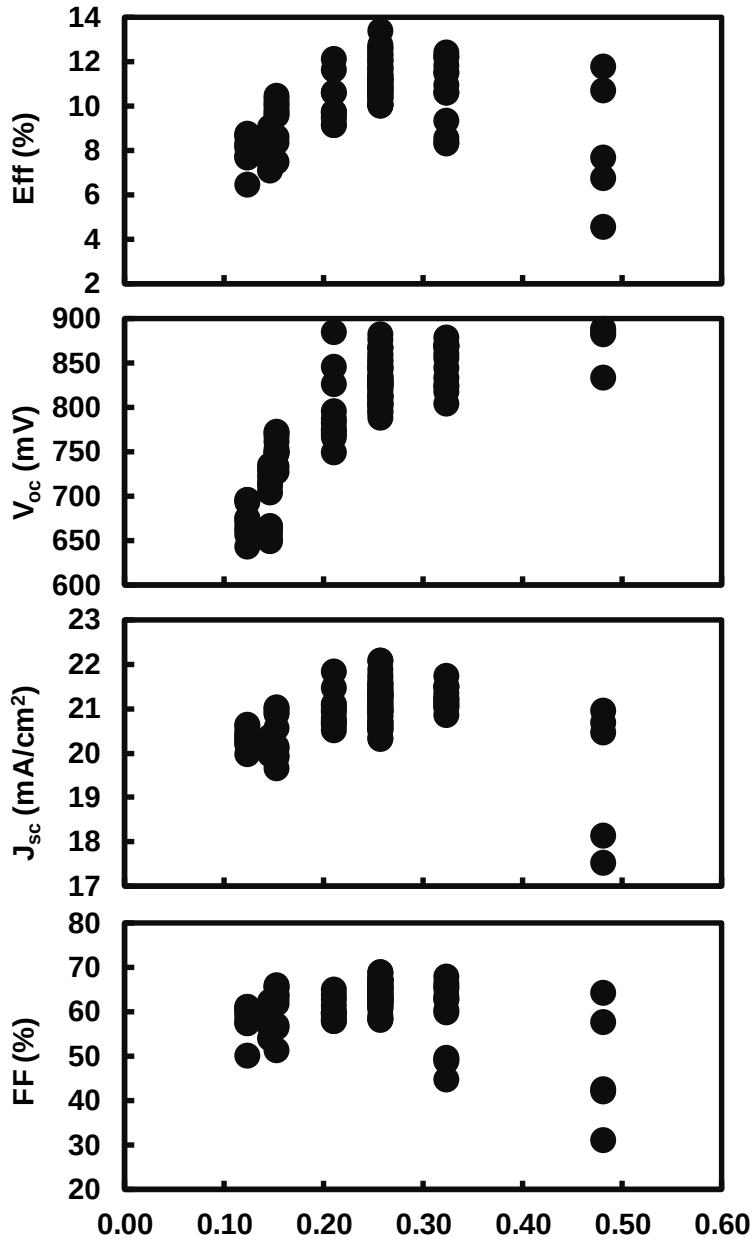

Fig. 4-8. Dependence of the electrical parameters of Se-free CIGS solar cells on the Mg contents in the $Zn_{1-x}Mg_xO$ buffer layer.

4.4 Chapter summary

In this chapter, an evaluation of the influence of a $Zn_{1-x}Mg_xO$ buffer layer on the performance of Se-free CIGS solar cells was presented. From the viewpoints of environmental friendliness and *Eff* improvement, $Zn_{1-x}Mg_xO$ was used as the n-type buffer layer instead of CdS, which is a well-known as a general material for n-type buffer layers. The $Zn_{1-x}Mg_xO$ and CdS buffer layers were also compared on the basis of their transparency in the short-wavelength region of the EQE spectrum. In addition, the dependence of various electrical parameters on the Mg content in $Zn_{1-x}Mg_xO$ buffer layers was shown. The results show that the $Zn_{1-x}Mg_xO$ buffer layer enhanced the J_{sc} of the solar cell because of its wider *Eg* compared with that of a CdS buffer layer; moreover, the V_{oc} was enhanced through optimization of the Mg content. Finally, high cell performance was demonstrated by a Se-free CIGS solar cell with a $Zn_{1-x}Mg_xO$ (Cd-free) buffer layer compared with the performance of previously reported Se-free CIGS solar cells [10]. The development of the $Zn_{1-x}Mg_xO$ buffer layer represents a major step forward in the manufacture of environmentally friendly Se-free CIGS solar cells. However, room still exists for improving the *Eff* because the CBO at the interface of the p-n junction demonstrated cliff behavior and because the Mg content requires further optimization in consideration of the relationship with other layers (e.g., i-ZnO layers). Regarding the other layers, the detail will be shown in next chapter.

References

[1] C. D. Klaassen, J. Liu, B. A. Diwan, *Toxicol. Appl. Pharmacol.* **238** (2009) 215-220.

[2] M. P. Waalkes, *Mutat. Res.* **533** (2003) 107-120.

[3] S. Merdes, R. Mainz, J. Klaer, A. Meeder, H. Rodriguez-Alvarez, H. W. Schock, M. C. Lux-Steiner, R. Klenk, *Sol. Energy Mater. Sol. Cells* **95** (2011) 864-869.

[4] S. Merdes, D. Abou-Ras, R. Mainz, R. Klenk, M. C. Lux-Steiner, A. Meeder, H. W. Schock, J. Klaer, *Prog. Photovolt: Res. Appl.* **21** (2013) 88-93.

[5] Y. Hashimoto, N. Kohara, T. Negami, N. Nishitani, T. Wada, *Sol. Energy Mater. Sol. Cells* **50** (1998) 71-77.

[6] K. L. Chopra, P. D. Paulson, V. Dutta, *Prog. Photovolt: Res. Appl.* **12** (2004) 69-92.

[7] R. H. Bube, *"Photoconductivity" Wiley Encyclopedia of Electrical and Electronics Engineering* (1999).

[8] F. V. Shallcros, *RCA Rev.* **28** (1967) 569.

[9] T. Minemoto, T. Negami, S. Nishiwaki, H. Takakura, Y. Hamakawa, *Thin Solid Films* **372** (2000) 173-176.

[10] S. Merdes, R. Sachez-Aroz, A. Ennaoui, J. Klaer, M. C. Lux-Steiner, R. Klenk, *Appl. Phys. Lett.* **95** (2009) 213502.

5

Investigation of the impact of interfaces

5.1 Introduction

To this point, the development of p-type absorber and n-type buffer layers has been discussed from the viewpoint of improving the conversion efficiency (*Eff*) of Se-free Cu(In,Ga)S_2 (CIGS) solar cells via environmentally friendly and low-cost processes. In this chapter, for further improvement of cell performance, the impact of the other layer at the interface between the back or front electrode and the p-type or n-type layers is investigated. The discussion is focused particularly on MoS_2 and intrinsic-ZnO (i-ZnO) layers, as shown in Fig. 5-1.

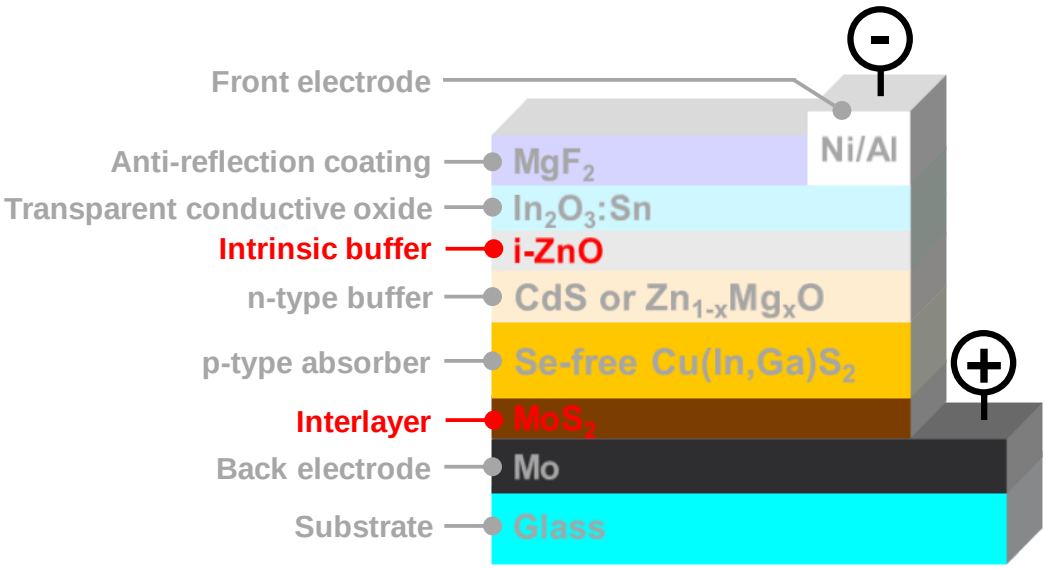

Fig. 5-1. Structure of the Se-free CIGS solar cell.

5.2 Interface between back electrode and p-type absorber

5.2.1 MoS_2 layer

The transition-metal dichalcogenide semiconductor MoS_2 is well known to be an attractive material for the study of fundamental physics in two-dimensional crystals and layered thin-film structures. In addition, MoS_2 is often used for absorber layers in solar cells, as a dry lubricant, in thin-film transistors, and in ultrathin heterostructured memory devices [1-4]. In this section, the role of MoS_2 as an interlayer between Mo back electrode and Se-free CIGS absorber layers is discussed.

5.2.2 Effect of MoS_2 interlayer

In Chapter 3, the Se-free absorber layer was optimized through high-temperature sulfurization and control of the Ga depth-profile; moreover, the thickness of the CdS buffer layer was optimized in Chapter 4. As a result, the *Eff* was drastically improved to greater than 15% from less than 4%, as shown in Fig. 5-2 (details of the electrical parameters for each cell are given in Table 5-I). However, explaining why these optimizations individually increased the cell performance is difficult. Therefore, other factors that might enhance the *Eff* of the Se-free CIGS cell was investigated. Consequently, it is speculated that the MoS_2 layer at the interface between the Mo and Se-free CIGS positively affects cell performance, as follows.

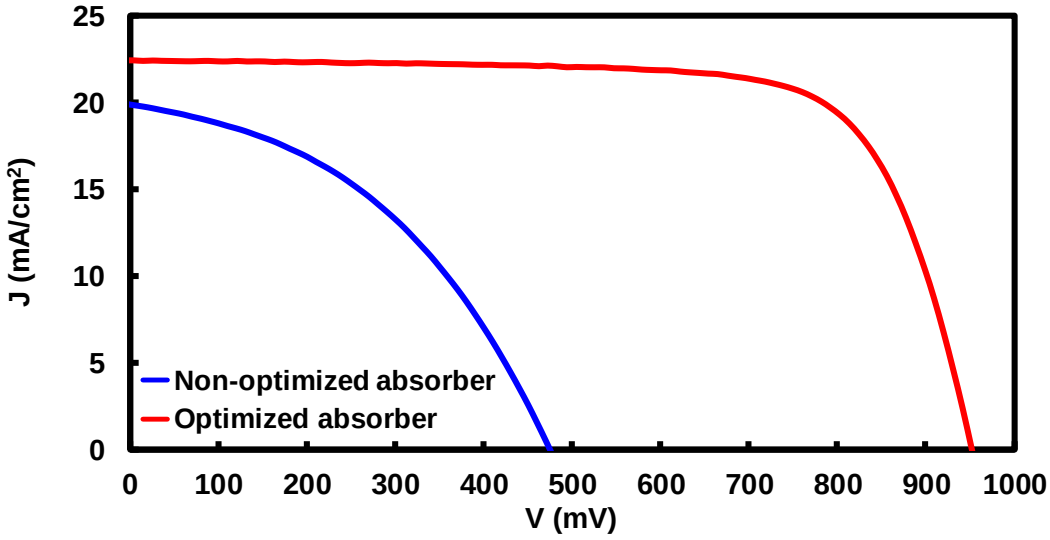

Fig. 5-2. Comparison of the *J–V* curves in Se-free CIGS solar cells with non-optimized and optimized absorber layers. Both cells have CdS buffer layers.

Table 5-I. Electric parameters of Se-free CIGS solar cells with different absorbers.

Sample	Eff (%)	V_{oc} (mV)	J_{sc} (mV)	FF (%)
Non-optimized absorber	3.97	474	19.9	42.2
Optimized absorber	15.7	952	22.4	73.5

Scanning electron microscopy (SEM) and energy-dispersive spectroscopy (EDX) (SEM-EDX) images of cross-sections of the Se-free CIGS solar cell with the optimized CdS buffer layer, which demonstrated an *Eff* of 15.7%, are shown in Fig. 5-3. Figure 5-3 (a) shows a thin layer at the interface between the Mo layer and the Se-free CIGS layer; in addition, Figs. 5-3 (b) and (c) highlight that the thin layer is a compound that consists of S and Mo. Furthermore, secondary-ion mass spectrometry (SIMS) analysis was performed to verify the composition of the thin layer. Figure 5-4 shows the depth profiles of S and Mo in the Se-free CIGS cell; this figure clearly shows a S-rich composition at the surface of the Mo back electrode layer. Thus, a thin layer exists at the interface between the Mo back electrode and the Se-free CIGS absorber layers and it can be regarded as a MoS_2 layer. With respect to the effects of this MoS_2 interlayer, the short-circuit current density (J_{sc}) and open-circuit voltage (V_{oc}) were presumably enhanced because of decrease carrier recombination at the interface. It is also assumed that the fill factor (*FF*) was improved because of the transition from schottky to ohmic contact. On the basis of these effects, the improvement of the cell performance of the Se-free CIGS solar cell resulted not only from high-temperature sulfurization, control of the Ga depth profile, and optimization of the CdS buffer layer thickness, but also from the formation of a MoS_2 interlayer at the interface between the Mo back electrode layer and the p-type Se-free CIGS absorber layer.

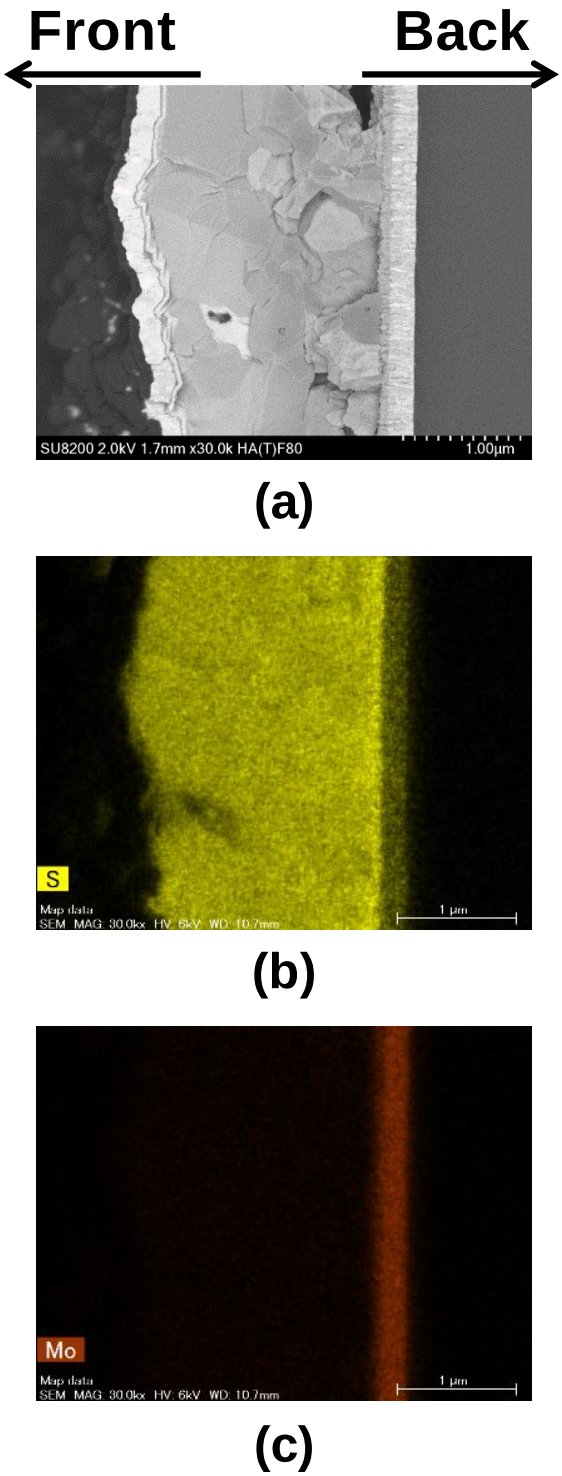

Fig. 5-3. (a) SEM and (b) S and (c) Mo EDX mapping images of a cross-section of the Se-free CIGS solar cell that demonstrated an *Eff* of 15.7%.

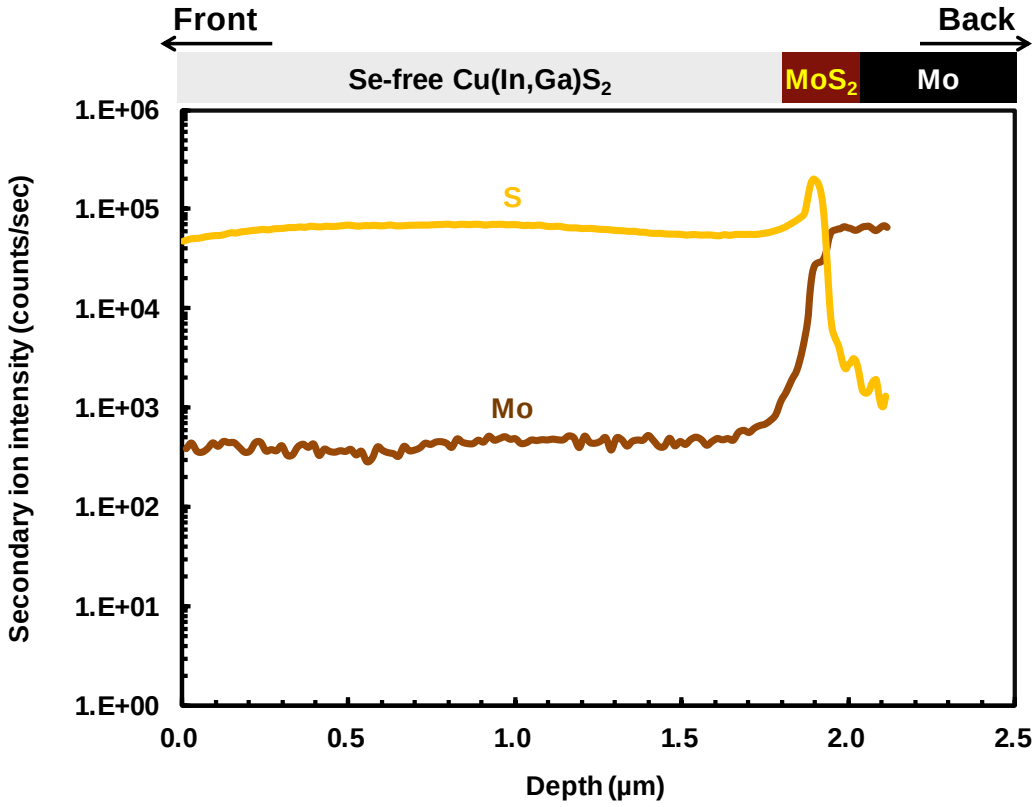

Fig. 5-4. SIMS depth-profiles of S and Mo in a Se-free CIGS solar cell.

5.3 Interface between n-type buffer and front electrode

5.3.1 i-ZnO layer

ZnO is a promising material for many optoelectronic applications, including solar cells and light-emitting diodes, among others, because it has a wide *Eg* with a large excitation binding energy [5-15]. With regards to the application of ZnO in Cu(In,Ga)(Se,S)$_2$ (CIGSeS)-based solar cells, i-ZnO is used as a high-resistivity interlayer for preventing leakage current at the interface between the n-type buffer layer and transparent conductive oxide (TCO) layer; in addition, it protects the p-n junction from sputtering damage during TCO deposition [5-8]. Thus, the i-ZnO layer plays an important role in

the development of Se-free CIGS cells as well as in the development of other CIGSeS-based cells.

5.3.2 Dependence of fill factor on i-ZnO thickness

As mentioned in Chapter 4, the $Zn_{1-x}Mg_xO$ buffer layer was optimized via control of the Mg/(Zn+Mg) ratio. The optimization of the $Zn_{1-x}Mg_xO$ buffer layer enhanced the J_{sc} and the V_{oc}; as a result, the Se-free CIGS solar cell with a $Zn_{1-x}Mg_xO$ buffer layer demonstrated a higher *Eff* compared with that of a Se-free CIGS cell (fabricated using an identical absorber) with a CdS buffer layer. However, as shown in Fig. 5-5, the *FF* was still low because the i-ZnO layer had not been modified. To prevent leakage current caused by shunt-pass at the interface between the $Zn_{1-x}Mg_xO$ buffer and TCO layers, the thickness of the i-ZnO layer (~40 nm) on the $Zn_{1-x}Mg_xO$ buffer layer was set thicker than the i-ZnO layer (~10 nm) on the CdS buffer layer. An excessively thick i-ZnO layer was assumed to have caused a high *Rs* and to have restricted the *FF*. Thus, in this section, the dependence of the thickness of the i-ZnO layer on the *FF* of Se-free CIGS solar cells was investigated for further *Eff* improvement.

Figure 5-6 shows the *FF* and *Eff* on Se-free CIGS cells with four different i-ZnO layers. In this experiment, i-ZnO layers with thickness of 40, 30, 20, and 10 nm were deposited via ALD onto absorbers fabricated using identical processes and their electrical parameters were evaluated. Thinner i-ZnO layers demonstrated higher *FF* and *Eff* values. The *FF* reached 74.5% and the *Eff* was greater than 16% in the case of the Se-free CIGS solar cell with a 10 nm i-ZnO layer. On the basis of these results, a thin i-ZnO layer effectively enhanced the *Eff* by improving the *FF*.

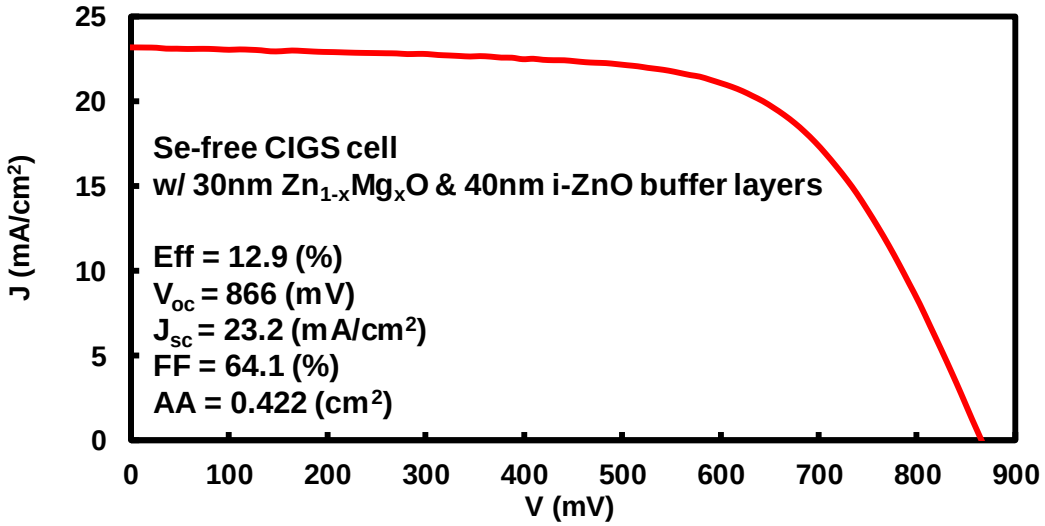

Fig. 5-5. *J–V* curve of a Se-free CIGS solar cell with an optimized $Zn_{1-x}Mg_xO$ buffer layer.

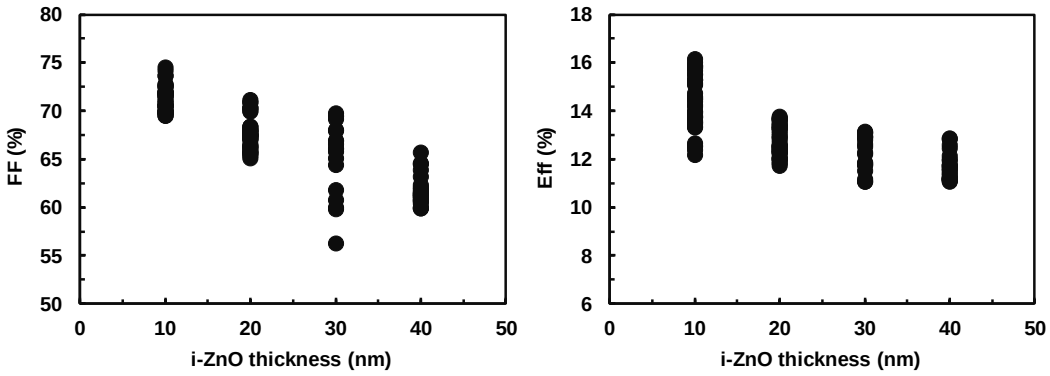

Fig. 5-6. Dependence of the thickness of the i-ZnO layer on the electrical parameters of Se-free CIGS solar cells with 30 nm $Zn_{1-x}Mg_xO$ buffer layers.

5.4 Chapter summary

In this chapter, the influence of two interlayers—a MoS_2 layer (at the interface between the Mo back electrode and the Se-free CIGS absorber layer) and an i-ZnO layer (at the interface between the $Zn_{1-x}Mg_xO$ buffer and TCO layers)— were revealed. MoS_2 layer enhanced the J_{sc} and the V_{oc} by decreasing carrier recombination at the interface; in addition, the *FF* was assumed to have been improved by ohmic contact. However, the influence of the i-ZnO layer on the *FF* was strongly dependent on its thickness. Compared with a thick i-ZnO layer, a thin i-ZnO layer resulted in a higher *FF*. As a result, an *Eff* greater than 16% was obtained, with a *FF* of 74.5%, by introducing a 10 nm i-ZnO layer into the Se-free CIGS solar cell with a $Zn_{1-x}Mg_xO$ buffer layer. This *Eff* is greater than any *Eff* previously reported for a Se-free CIGS cell. The details of this cell, including its *J*–*V* characteristics, are discussed in the next chapter.

References

[1] H. Rashid, K. S. Rahman, M. I. Hossain, N. Tabet, F. H. Alharbi, N. Amin, *Chalcogenide Letters* **11** (2014) 397-403.

[2] K. F. Mak, C. Lee, J. Hone, J. Shan, T. F. Heinz, *Phys. Rev. Lett.* **105** (2010) 136805.

[3] S. Kim, A. Konar, W. S. Hwang, J. H. Lee, J. Lee, C. Jung, H. Kim, J. B. Yoo, Y. M. Jin, S. Y. Lee, D. Jena, W. Choi, K. Kim, *Nature Commun.* **3** (2012) 1011.

[4] M. S. Choi, G. H. Lee, Y. J. Yu, D. Y. Lee, S. H. Lee, P. Kim, J. Hone, W. J. Yoo, *Nature Commun.* 4 (2013) 1624.

[5] S. Chaisitsak, T. Sugiyama, A. Yamada, M. Konagai, *Jpn. J. Appl. Phys.* **38** (1999) 9A.

[6] D. Braunger, D. Hariskos, T. Walter, H.W. Schock, *Sol. Energy Matr. Sol. Cells* **40** (1996) 97-102.

[7] S. Ishizuka, K. Sakurai, A. Yamada, K. Matsubara, P. Fons, K. Iwata, S. Nakamura, Y. Kimura, T. Baba, H. Nakanishi, T. Kojima, S. Niki, *Sol. Energy Matr. Sol. Cells* **87** (2005) 541-548.

[8] U. Rau, M. Schmidt, *Thin Solid Films* **387** (2001) 141-146.

[9] Z. K. Tang, G. K. L. Wong, P. Yu, M. Kawasaki, A. Ohtomo, H. Koinuma, Y. Segawa, *Appl. Phys. Lett.* **72** (1998) 3270.

[10] H. Cao, J. Y. Xu, E. W. Seeling, R. P. H. Chang, *Appl. Phys. Lett.* **76** (2000) 2997.

[11] T. Aoki, Y. Hatanaka, D. C. Look, *Appl. Phys. Lett.* **76** (2000) 3257.

[12] X. L. Guo, J. H. Choi, H. Tabata, T. Kawai, *Jpn. J. Appl. Phys.* **40** (2001) 177.

[13] C. P. Park, I. S. Jeong, J. H. Kim, S. Im, *Appl. Phys. Lett.* **82** (2003) 3973.

[14] P. F. Carcia, R. S. McLean, M. H. Reilly, G. N. Jr, *Appl. Phys. Lett.* **82** (2003) 1117.

[15] A. Tsukazaki, A. Ohtomo, T. Onuma, M. Ohtani, T. Makino, M. Sumiya, K. Ohtani, S. F. Chichibu, S. Fuke, Y. Segawa, H. Ohno, H. Koinuma, M. Kawasaki, *Nat. Mater.* **4** (2005) 42-46.

6

New world record conversion efficiency

6.1 Introduction

Various approaches to improving the cell performance of Se-free CIGS solar cell have been described in the previous chapters. In this chapter, the best conversion efficiency (*Eff*) achieved by combining all of them is demonstrated. There are two results for the *Eff* of optimized Se-free Cu(In,Ga)S_2 (CIGS) solar cells. One is an *Eff* of 15.5%, which was certificated by an external institution; the other is an *Eff* of 16.9%, which was an in-house measurement. Both results were achieved using a Cu-poor absorber and $Zn_{1-x}Mg_xO$ buffer layers, meaning that a new world record *Eff* was achieved with a Se-free CIGS solar cell with components fabricating KCN-free and Cd-free processes, as shown in Fig. 6-1 [1-7]. In addition, to achieve greater than 18% *Eff* in the future, the $V_{oc,deficit}$, which is a key factor in improving the cell performance, is discussed in this chapter.

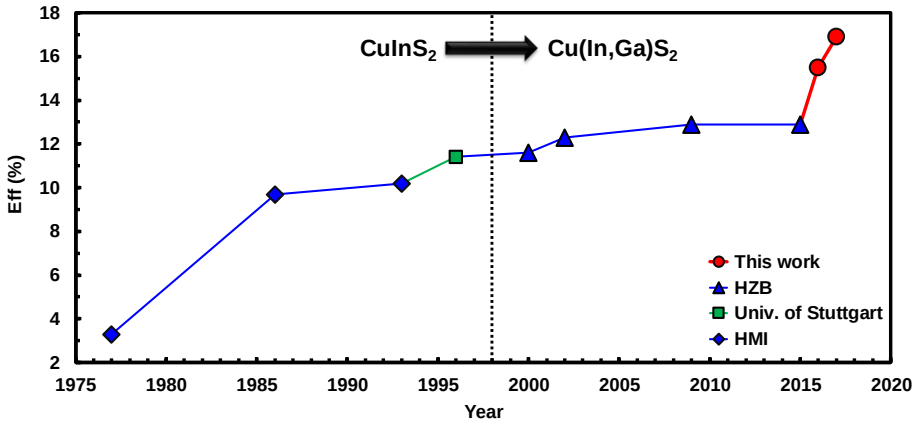

Fig. 6-1. Conversion efficiency trend of Se-free CIGS solar cells.

6.2 Single cell

6.2.1 15.5% efficiency cell (certified)

In the field of Se-free CIGS solar cells, as a world record efficiency, Merdes *et al*. reported an *Eff* of 12.9% for a Se-free CIGS cell fabricated via a KCN-etching process with a CdS buffer layer [7]. This efficiency has not been improved for years. However, the record was broken in this study and a new record exceeded the limit of 15% *Eff* thanks to optimization of each layer composing the Se-free CIGS cell. Furthermore, the absorber layer was fabricated by a KCN-free process, and the buffer layer consisted of Cd-free materials. Figure 6-2 shows the new world record *Eff* of 15.5% which is a number independently certified by an external accredited laboratory. The electrical parameters are as follows: *Eff* = 15.5%, open-circuit voltage (V_{oc}) = 920 mV, short-circuit current density (J_{sc}) = 23.4 mA/cm^2, fill factor (*FF*) = 72.2%, and area = 0.433 cm^2. The measurement was performed at the Fraunhofer Institute for Solar Energy Systems calibration laboratory. It was achieved with a Se-free CIGS solar cell fabricated with a Cu-poor absorber and a $Zn_{1-x}Mg_xO$ buffer layer. This is the highest *Eff* reported for a Se-free CIGS solar cell.

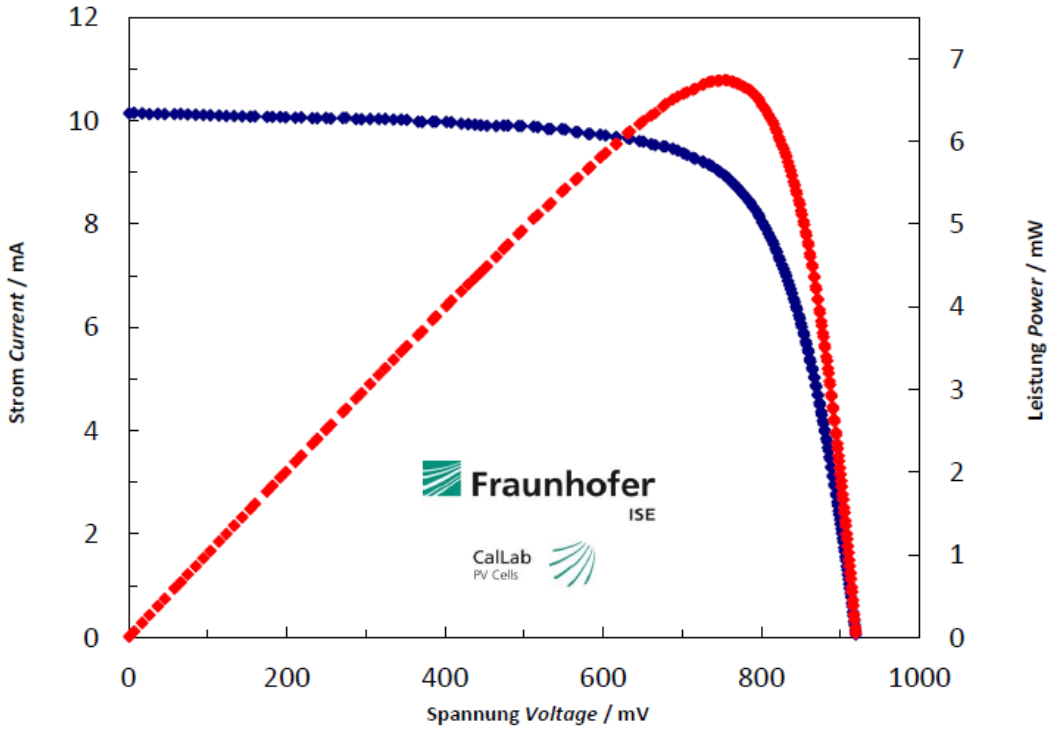

V_{OC}	=	(	920.0	±	3.1	) mV
I_{SC} (Ed.2 - 2008)/3/	=	(	10.15	±	0.19	) mA
J_{SC}	=	(	23.41	±	0.44	) mA/cm²
I_{MPP}	=		8.96			mA
V_{MPP}	=		751.8			mV
P_{MPP}	=	(	6.74	±	0.13	) mW
FF	=	(	72.16	±	0.47	) %
η	=	(	15.54	±	0.33	) %

Fig. 6-2. *J–V* characteristics of the new world record Se-free CIGS solar cell. (© 2015 IEEE.)

6.2.2 16.9% efficiency cell (in-house)

After achieving an *Eff* of 15.5%, the improvement of the *Eff* of the Se-free CIGS cell was continued. When measured in-house, the *Eff* of the Se-free CIGS solar cell fabricated via the KCN-free process and with a $Zn_{1-x}Mg_xO$ buffer layer reached 16.9%. The *J*–*V* and external quantum efficiency (EQE) characteristics of this cell are shown in Fig. 6-3 (a) and (b).

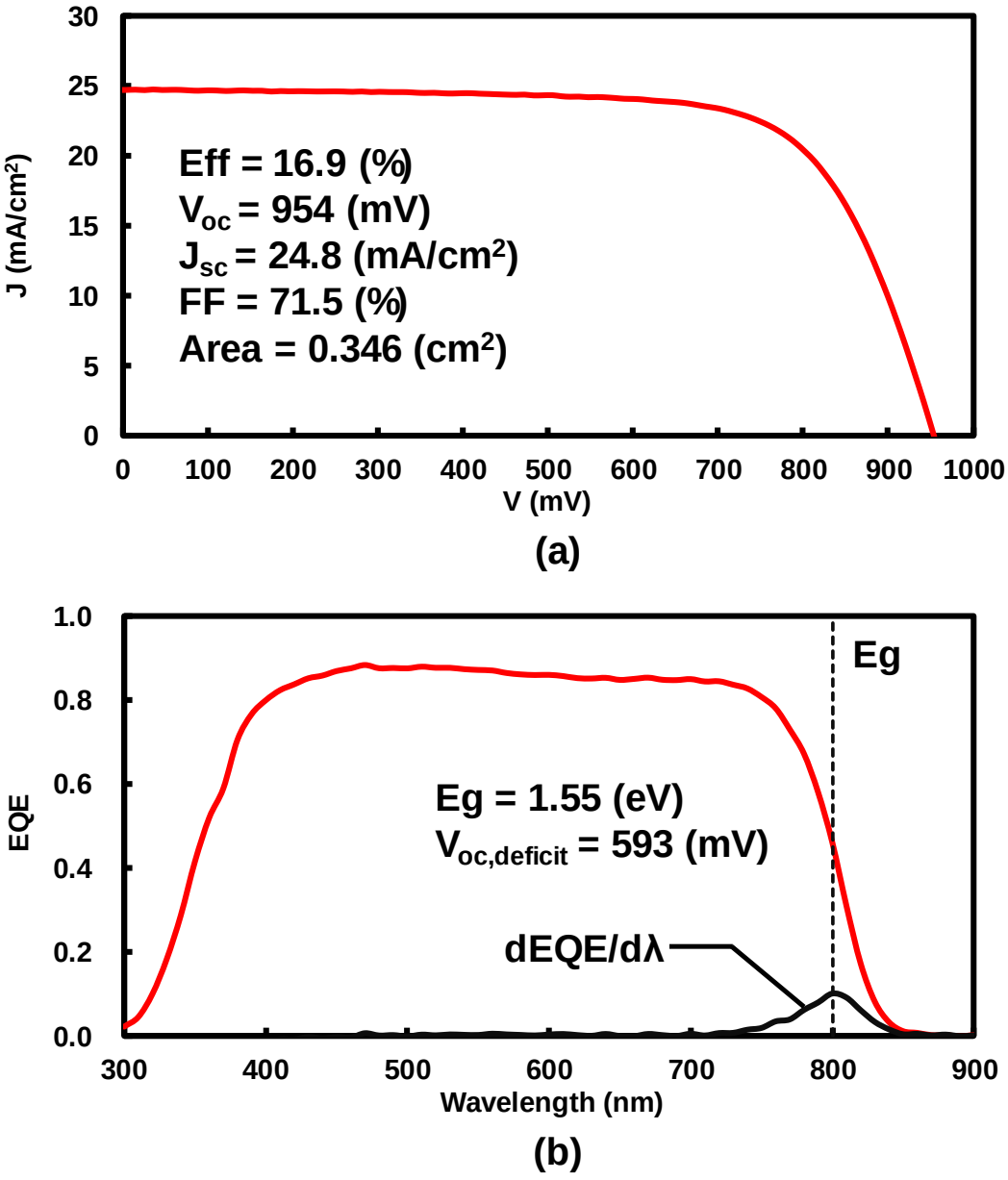

Fig. 6-3. (a) *J*–*V* and (b) EQE curves of the Se-free CIGS cell that demonstrated the *Eff* of 16.9%.

To understand the details of the aforementioned champion cell, all analyses explained and demonstrated in the previous chapters were conducted. As discussed in Chapter 3, optimization of the Ga depth profile can enhance the electrical parameters, especially the J_{sc} and V_{oc}. Figure 6-4 presents the Ga/(Ga+In) (GGI) ratio depth profile of the

champion cell measured by secondary-ion mass spectrometry (SIMS). The absorber of the champion cell had a lower GGI ratio (~5%) at the surface and steeper GGI depth profile gradient (from ~5% to ~70%) than before. In addition, scanning electron microscopy–energy-dispersive X-ray spectroscopy (SEM-EDX) and SIMS analyses were used to investigate the MoS_2 interlayer because the MoS_2 layer existing at the interface between the layer Mo and the Se-free CIGS layer positively influences cell performance, as shown in Chapter 5. Figure 6-5 (a) shows a thin layer at the interface between the Mo layer and the Se-free CIGS layer. Moreover, Fig. 6-5 (b) and (c) highlight that the thin layer is a compound that consists of S and Mo. Figure 6-6 also shows the depth profiles of S and Mo in the Se-free CIGS cell, as measured by SIMS, and it reveals a S-rich composition on the surface of Mo. Collectively, these results indicate that a MoS_2 layer exists at the interface between the Mo layer and the Se-free CIGS layer.

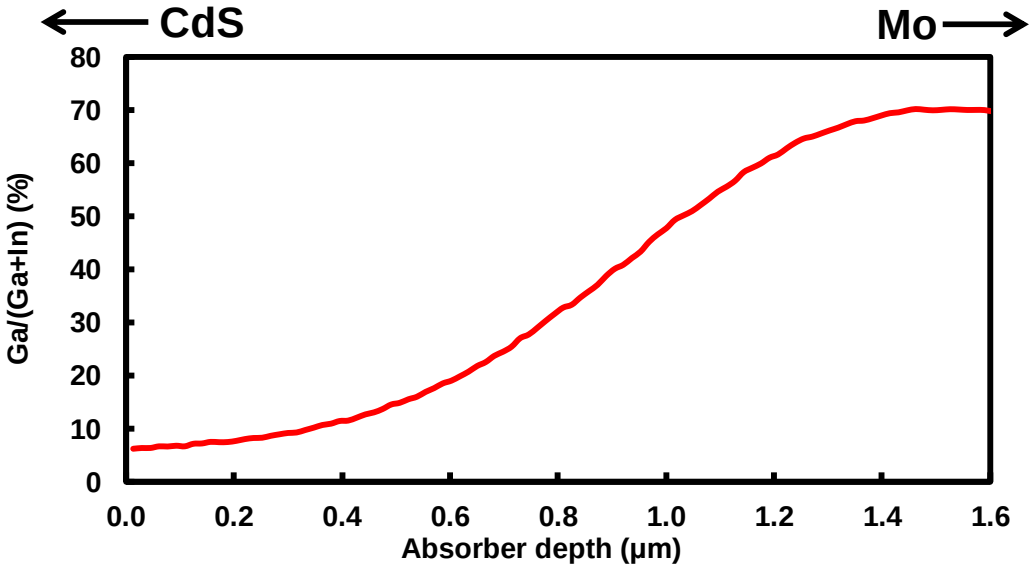

Fig. 6-4. GGI depth profiles of the Se-free CIGS champion cell.

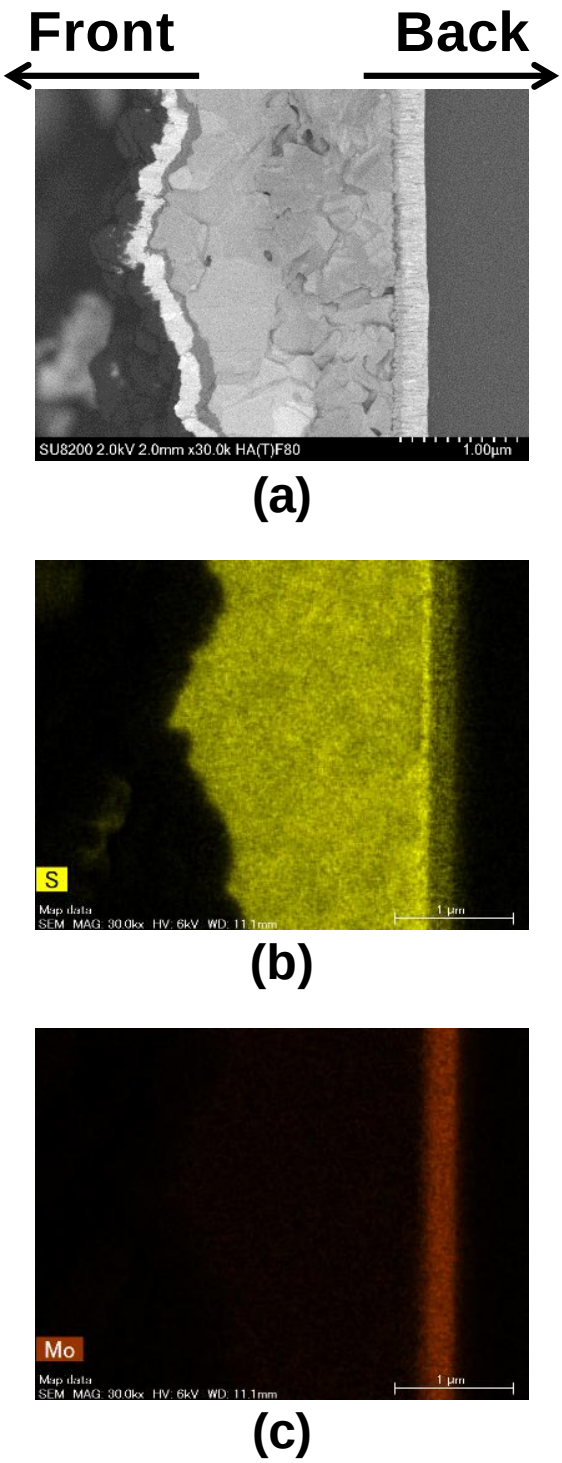

Fig. 6-5. (a) SEM and (b) S and (c) Mo EDX mapping images of the cross section of the Se-free CIGS champion cell.

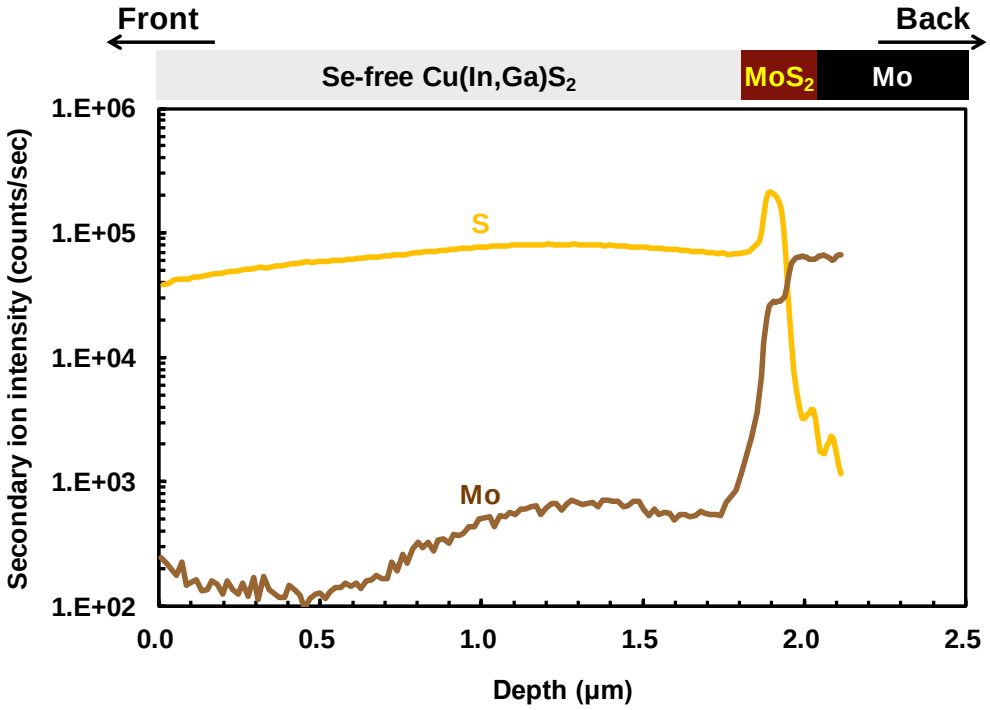

Fig. 6-6. SIMS depth profiles of S and Mo in the Se-free CIGS champion cell.

As previously mentioned, the absorber of the champion cell demonstrated superior performance. The $Zn_{1-x}Mg_xO$ buffer layer was also analyzed to evaluate the coverage and band-diagram between the absorber and buffer layers. SEM-EDX images of the cross section of the Se-free CIGS champion cell with an optimized $Zn_{1-x}Mg_xO$ buffer layer are displayed in Fig. 6-7. They indicate that the $Zn_{1-x}Mg_xO$ buffer layer covers the whole of the surface of the absorber. Figure 6-8 shows the band diagram for the Se-free CIGS champion cell with a $Zn_{1-x}Mg_xO$ (x = 0.34) buffer layer. It indicates that the CBM of the buffer layer in the vicinity of the interface can be increased compared with those of previous cells (see Fig. 4-7 in Chapter 4). This upward shift of the CBM with an increase in the Mg content improved the *Eff*. By combining the optimized absorber layer and optimized buffer layer, an *Eff* of 16.9% was achieved for the Se-free CIGS solar cell.

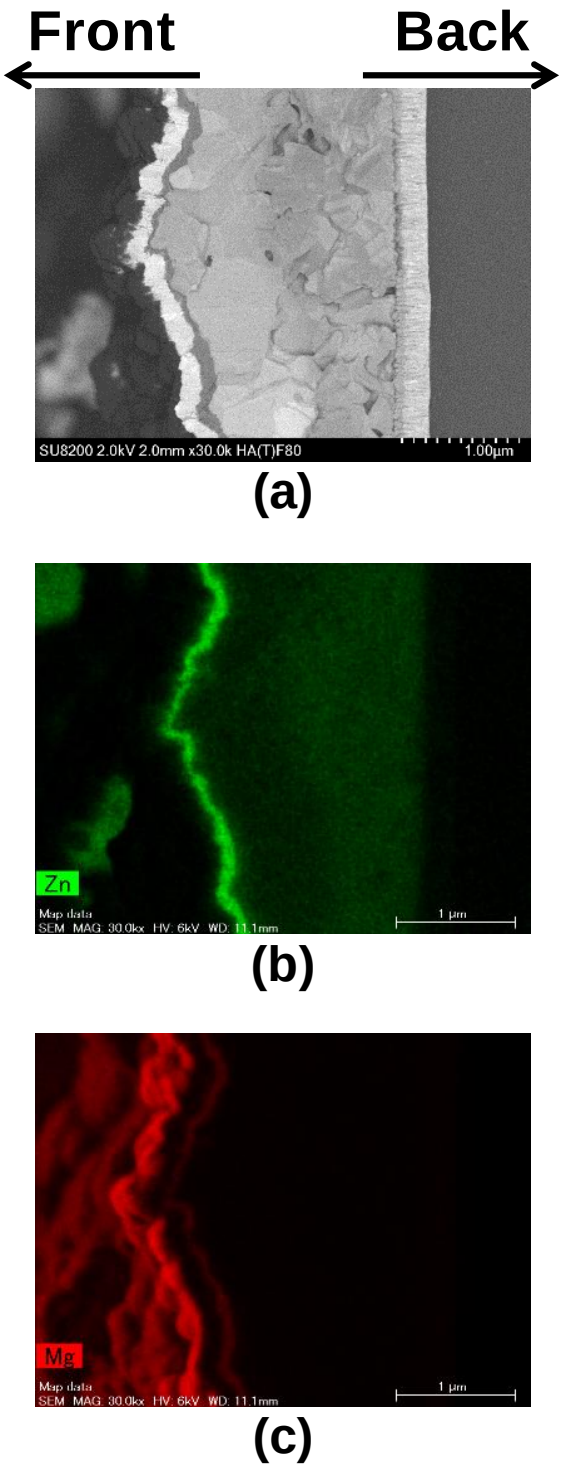

Fig. 6-7. (a) SEM and (b) Zn and (c) Mg EDX mapping images of the cross section of the Se-free CIGS champion cell.

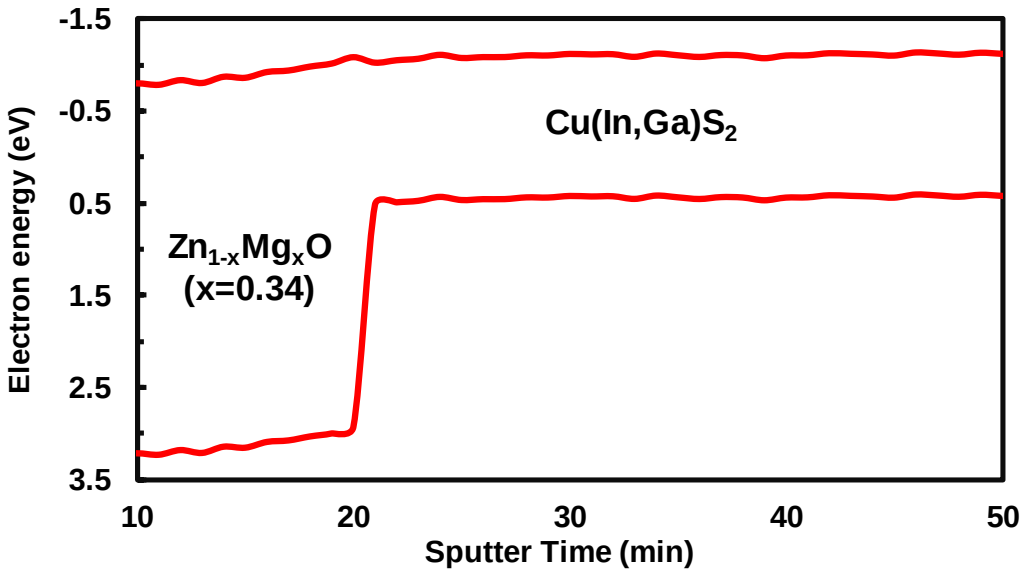

Fig. 6-8. Band diagram corresponding to the interface between the absorber and buffer layers of the Se-free CIGS champion cell.

6.3 Highest open-circuit voltage

To this point, improvements of the *Eff* of Se-free CIGS solar cells was mainly demonstrated. As a result, *Eff* values of 15.5% (certified) and 16.9% (in-house) were attained, which are world records in the field of Se-free CIGS solar cells. However, these *Eff* values are still low compared with those of CIGSe, CdTe and perovskite solar cells [8-10]. One of the major limitations of the *Eff* is assumed to be the V_{oc}, especially the $V_{oc,deficit}$, which is defined by equation (6-1):

$$V_{oc,deficit} = Eg/q - V_{oc} \qquad (6\text{-}1)$$

Figure 6-9 shows the V_{oc} as a function of *Eg* for Se-free CIGS solar cells reported by HZB [11-13]. HZB was a pioneer of Se-free CIGS development, and their cells demonstrated a comparatively high *Eff* of greater than 12%; however, the V_{oc} did not reach 900 mV and $V_{oc,deficit}$ was greater than 0.65 V. This $V_{oc,deficit}$ value is obviously

higher than those reported for other solar cells such, as 0.37 V for a CIGSeS cell and 0.41 V for a perovskite cell [10, 14], both of which easily demonstrated a high *Eff* greater than 20%. (Recently, an *Eff* of 22.8% (in-house) for a CIGSeS-based cell by Solar Frontier K.K. and 22.1% (certified) for a $FAPbI_3$-based perovskite cell by KRICT/UNIST have been reported [10, 14-16].) Thus, to enhance the *Eff* of Se-free CIGS cells, improvement of the $V_{oc,deficit}$ is necessary. In this section, the V_{oc} and $V_{oc,deficit}$ of Se-free CIGS cells fabricated in this work are shown and methods to enhance cell performance in the future are discussed on the basis of the results.

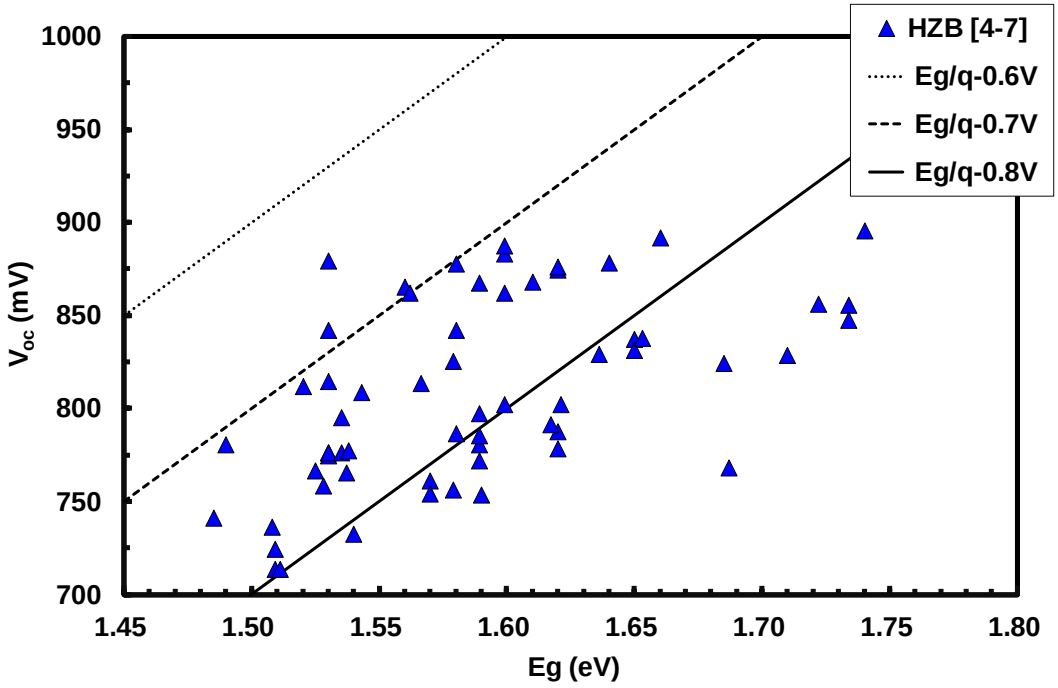

Fig. 6-9. The V_{oc} as a function of the *Eg* for Se-free CIGS solar cells reported by HZB [10-13].

Initially, the Se-free CIGS cell of the first trial showed a $V_{oc,deficit}$ greater than 1.0 V with *Eg* = 1.53 eV; however, it was improved to 0.72 eV with *Eg* = 1.54 eV after crystal

growth was promoted and the Ga grading in the absorber was controlled (see Figs. 3-3 and 3-13 in Chapter 3). Furthermore, the Ga grading was optimized via RTA during sulfurization and a $Zn_{1-x}Mg_xO$ buffer layer was applied via ALD. As Fig. 6-10 indicates, a higher V_{oc} was achieved with a higher ramp rate during sulfurization, with a drastically improved $V_{oc,deficit}$. In addition, the V_{oc} improvement was confirmed by applying a $Zn_{1-x}Mg_xO$ buffer layer. This result suggests that both the absorber quality and the interface between the buffer and the absorber layers are among the key factors influencing the V_{oc}; in addition, the incorporation of a $Zn_{1-x}Mg_xO$ buffer layer into the Se-free CIGS cells is very effective for increasing the V_{oc}. Consequently, a V_{oc} of 973 mV was achieved with an absorber with an Eg of 1.57 eV and the $V_{oc,deficit}$ was reduced to less than 0.60 V.

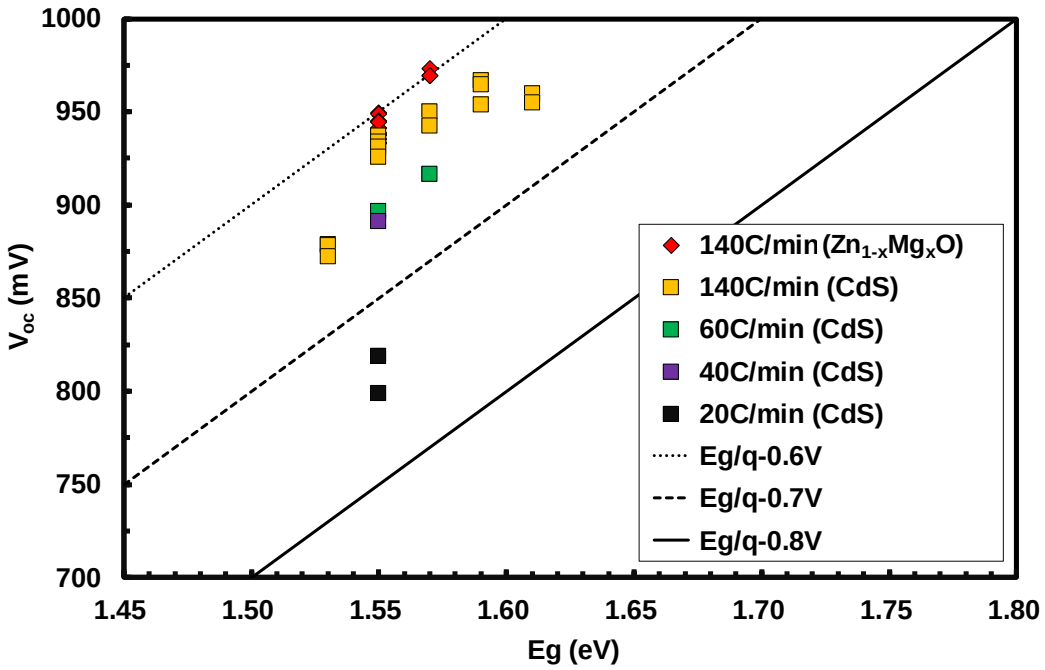

Fig. 6-10. Correlation between the V_{oc} and E_g on Se-free CIGS cells fabricated in this work.

Finally, further improvements of the $V_{oc,deficit}$ for the Se-free CIGS cells were achieved by adjusting the CBO, modifying the i-ZnO condition, fabricating the MoS_2 layer. This is just a result, however, a V_{oc} of 997 mV was achieved with a Se-free CIGS cell with a CdS buffer layer, as shown in Fig. 6-11; its *Eg* was 1.57 eV and its $V_{oc,deficit}$ reached 0.57 V. The V_{oc} of 997 mV is substantially greater than the V_{oc} values of previously reported Se-free CIGS cells in the world. This cell is currently under investigation, and further V_{oc} improvement is expected in the near future when a $Zn_{1-x}Mg_xO$ buffer layer is applied.

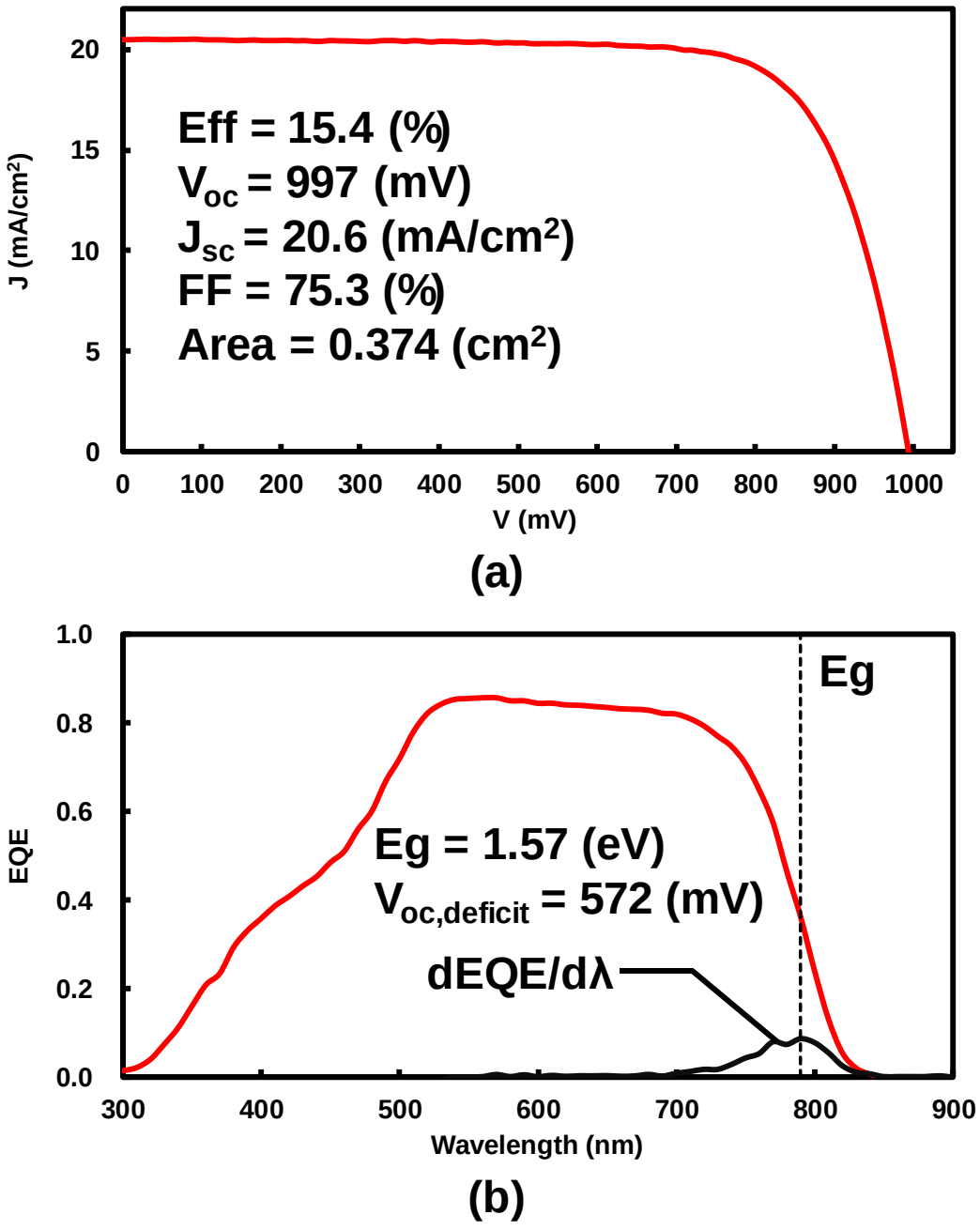

Fig. 6-11. (a) *J*–*V* and (b) EQE characteristics of the highest-V_{oc} Se-free CIGS solar cells.

Figure 6-12 is a $V_{oc,deficit}$ evaluation graph of the V_{oc} and Eg data obtained in this work plotted with the data in Fig. 6-9 (for a comparison of V_{oc} as a function of Eg for Se-free CIGS solar cells between HZB and this work). The V_{oc} values of Se-free CIGS solar cells fabricated in this study were very high, and the $V_{oc,deficit}$ was drastically improved compared to those of previously reported cell. However, the V_{oc} is still lower compared with those of CdTe and perovskite solar cells, which exhibit V_{oc} values greater than 1000 mV with $1.45 \leq Eg \leq 1.60$ eV. Thus, the pursuit of a V_{oc} greater than 1000 mV for Se-free CIGS solar cells will be continued, with the goal of further improving the *Eff*.

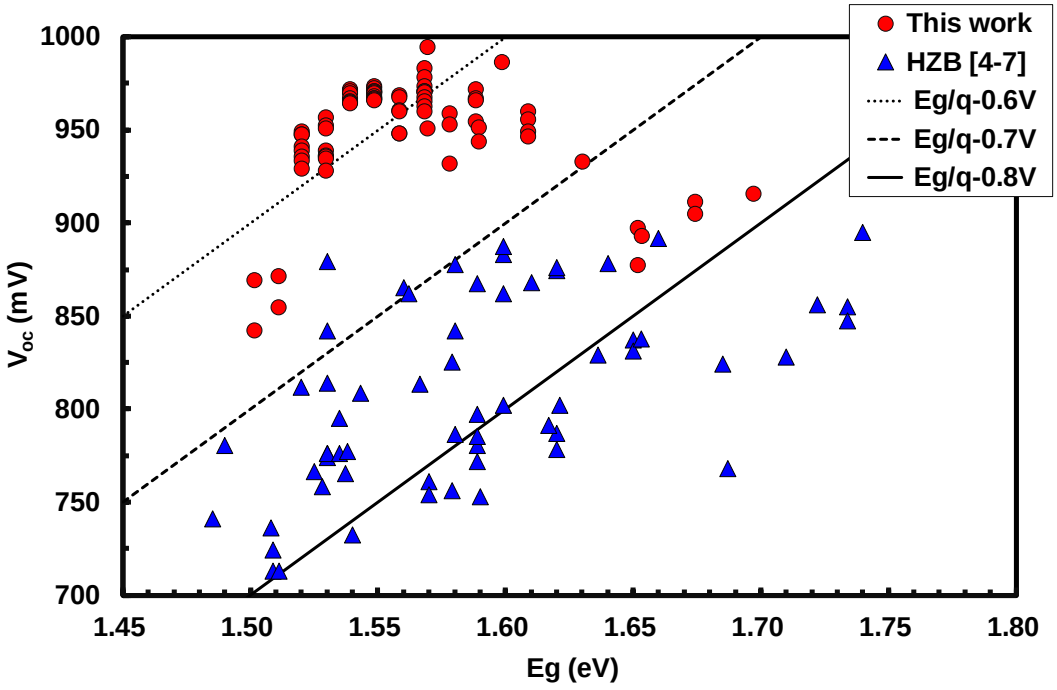

Fig. 6-12. Comparison of the V_{oc} as a function of Eg for Se-free CIGS solar cells between HZB and this work [10-13].

6.4 Chapter summary

In this chapter, the results of a new world record efficiency of 15.5% (certified) and 16.9% (in-house) for Se-free CIGS solar cells were presented. Both cells were fabricated using a Cu-poor absorber layer and a $Zn_{1-x}Mg_xO$ buffer layer. The obtained results mean that the cell performance of Se-free CIGS, which had not been improved for a long time, was enhanced using KCN-free and Cd-free processes. In addition, the highest V_{oc} of 997 mV was obtained with an *Eg* of 1.57 eV ($V_{oc,deficit}$ reached 0.57 V). On the basis of these results, the Se-free CIGS cells have great potential for future development. Thus, pursuit of a Se-free CIGS solar cell with greater than 18% *Eff* and a V_{oc} greater than 1000 mV for future products will be continued.

References

[1] L. L. Kazmerski, G. A. Sanborn, *J. Appl. Phys.* **48** (1977) 3178.

[2] H. J. Lewerenz, H. Goslowsky, K.-D. Husemann, S. Fiechter, *Nature* **321** (1986) 687-688.

[3] R. Scheer, T. Walter, H. W. Schock, M. L. Fearheiley, H. J. Lewerenz, *Appl. Phys. Lett.* **63** (1993) 3294.

[4] D. Braunger, D. Hariskos, T. Walter, H. W. Schock, *Sol. Energy Mater. Sol. Cells* **40** (1996) 97-102.

[5] R. Klenk, J. Klaer, R. Scheer, M. Ch. Lux-Steiner, I. Luck, N. Meyer, U. Ruhle, *Thin Solid Films* **480-481** (2005) 509-514.

[6] R. Klenk, J. Klaer, R. Mainz, M. Schmid, S. Merdes, *34th IEEE Photovoltaic Specialists Conference*, Philadelphia, USA (2009).

[7] S. Merdes, D. Abou-Ras, R. Mainz, R. Klenk, M. C. Lux-Steiner, A. Meeder, H. W. Schock, J. Klaer, *Prog. Photovolt: Res. Appl.* **21** (2013) 88-93.

[8] P. Jackson, R. Wuerz, D. Hariskos, E. Lotter, W. Witte, M. Powalla, *Phys. Status Solidi RRL* **10** (2016) 8, 583-586.

[9] First solar press release. First Solar Achieves yet another cell conversion efficiency world record, 24 February (2016).

[10] W. S. Yang, J. H. Noh, N. J. Jeon, Y. C. Kim, S. Ryu, J. Seo, S. I. Seok, *Science* **348** (2015) 6240, 1234–1237.

[11] S. Merdes, R. Mainz, J. Klaer, A. Meeder, H. Rodriguez-Alvarez, H. W. Schock, M. C. Lux-Steiner, R. Klenk, *Sol. Energy Mater. Sol. Cells* **95** (2011) 864-869.

[12] R. Klenk, S. Bakehe, R. Kaigawa, A. Neisser, J. Reis, M. Ch. Lux-Steiner, *Thin*

Solid Films. **451-452** (2004) 424-429.

[13] S. Merdes, P. Pistor, N. Allsop, R. Saez-Araoz, A. Ennaoui, D. Forster, A. Grimm, D. Kieven, J. Klaer, I. Lauermann, R. Mainz, A. Meeder, H. W. Schock, R. Klenk, M. C. Lux-Steiner, *23rd European PV Solar Energy Conference and Exhibition*, Valencia, Spain (2011).

[14] R. Kamada, T. Yagioka, S. Adachi, A. Handa, K. F. Tai, T. Kato, H. Sugimoto, *Proc., 43rd IEEE Photovoltaic Specialists Conference*, Portland, USA (2016).

[15] M. A. Green, K. Emery, Y. Hishikawa, W. Warta, E. D. Dunlop, D. H. Levi, A. W. Y. Ho-Baillie, *Prog. Photovolt: Res. Appl.* **25** (2017) 3-13.

[16] NREL "Best Research-Cell Efficiencies Chart", Accessed 13. 03. 2016, (2016). (http://www.nrel.gov/ncpv/images/efficiency_chart.jpg).

7

General summary and future prospects

7.1 General summary

In this study, as a next step in the development of Cu(In,Ga)(Se,S)$_2$ (CIGSeS)-based solar cells, increasing conversion efficiency of a Se-free Cu(In,Ga)S$_2$ (CIGS) solar cell fabricated using a KCN-free process was attempted through numerical and experimental evaluation. In addition, from the viewpoint of environmental conservation, a Cd-free process was also developed. Various approaches were used to enhance cell performance. As a result, the conversion efficiency (*Eff*), which had not been improved for an extended period, was enhanced.

A method to construct a KCN-free process via an absorber with a Cu-poor composition (CGI < 1.0) and fabricated from a Cu-poor precursor was proposed in Chapter 3. To solve the problem of poor crystallinity that is particular to Cu-poor absorbers, high-temperature sulfurization was introduced. Furthermore, the effects of Ga grading in a Se-free CIGS absorber was revealed and the Ga depth-profile was optimized via RTA during sulfurization. These techniques demonstrated that a high-quality absorber could be fabricated by a KCN-free process despite the use of Cu-poor absorber. As a result, cell performance was drastically improved.

In Chapter 4, a $Zn_{1-x}Mg_xO$ buffer layer was proposed as a Cd-free buffer layer instead of the commonly used CdS buffer layer. The $Zn_{1-x}Mg_xO$ buffer layer had the advantage of a wider bandgap (*Eg*) than a CdS buffer layer, and it positively affected the transparency toward short-wavelength radiation in the EQE spectrum. Additionally, an

increase in the Mg content in $Zn_{1-x}Mg_xO$ buffer layer modified the conduction-band offset (CBO) at the interface between the absorber and buffer layers (p-n junction). Because of these merits, the $Zn_{1-x}Mg_xO$ buffer layer further improved the *Eff*. The fabricated Se-free CIGS solar cell thus showed enhanced the conversion efficiency with a Cd-free buffer layer.

In Chapter 5, investigation of the impact of the MoS_2 layer at the interface between the Mo and absorber layers was detailed; moreover, the optimum conditions for deposition of the intrinsic-ZnO (i-ZnO) layer at the interface between the buffer and transparent conductive oxide (TCO) layers were proposed. The MoS_2 layer enhanced the short-circuit current density (J_{sc}) and the open-circuit voltage (V_{oc}) by decreasing carrier recombination at the interface; in addition, the fill factor (*FF*) was assumed to have been improved by ohmic contact. However, the *FF* was strongly dependent on the thickness of the i-ZnO layer. By reducing the thickness of the i-ZnO from 40 nm to 10 nm, the *Eff* was enhanced because of the improvement of the *FF* on the Se-free CIGS cell with a $Zn_{1-x}Mg_xO$ buffer layer.

In Chapter 6, new world records—*Eff* values of 15.5% (certified) and 16.9% (in-house)—achieved by combining all of the approaches described in this thesis to optimize cell performance were reported. Both of the champion cells were fabricated with Cu-poor absorber and $Zn_{1-x}Mg_xO$ buffer layers, which is why, in this study, a new world record *Eff* for a Se-free CIGS solar cell was achieved with KCN-free and Cd-free processes. Furthermore, a V_{oc} of 997 mV was obtained with an *Eg* of 1.57 eV ($V_{oc,deficit}$ reached 0.57V), demonstrating the limitless possibilities for Se-free CIGS solar cells.

All the aforementioned results revealed that Se-free CIGS has strong potential for future development. The pursuit of higher-potential Se-free CIGS solar cells will be

continued to enable the future development of outstanding products.

7.2 Future prospects

In this study, the potential of Se-free CIGS single cells was revealed; however, looking forward, the development of not only single cells but also mini-modules of Se-free CIGS is needed. Thus, the development of a Se-free CIGS mini-module is described at the end of this thesis.

Figure 7-1 shows schematic images of a Se-free CIGS single cell and a mini-module for comparison. Basically, they were fabricated via the same process. The details of the fabrication process and the device structure are described in Figs. 7-2 and 7-3. First, Mo back electrode, Cu, Ga, and In metal-stack precursor layers were deposited by DC-sputtering onto a glass substrate with the first pattern (P1) for interconnections. The precursor layer was sulfurized with H_2S gas in a furnace to form a Se-free CIGS absorber layer. A buffer layer was deposited onto the absorber layer by chemical bath deposition (CBD) or atomic layer deposition (ALD). i-ZnO and TCO layers were then deposited with the second and third patterns (P2 and P3). Finally, a MgF_2 anti-reflective layer was deposited by electron-beam evaporation. The glass substrate dimensions and the aperture area were 5×3 cm^2 and 10.6 cm^2, respectively. A monolithically integrated structure with seven series connections was introduced by laser and mechanical patterning.

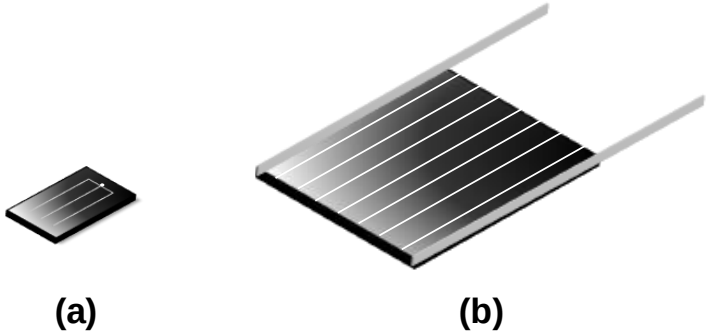

Fig. 7-1. Schematics of Se-free CIGS: (a) single cell and (b) mini-module.

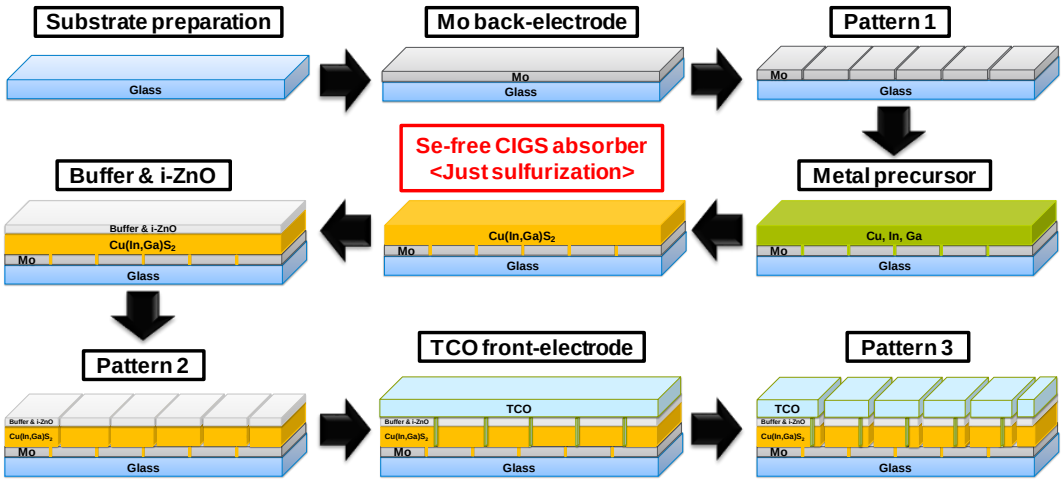

Fig. 7-2. Fabrication process of the Se-free CIGS mini-module.

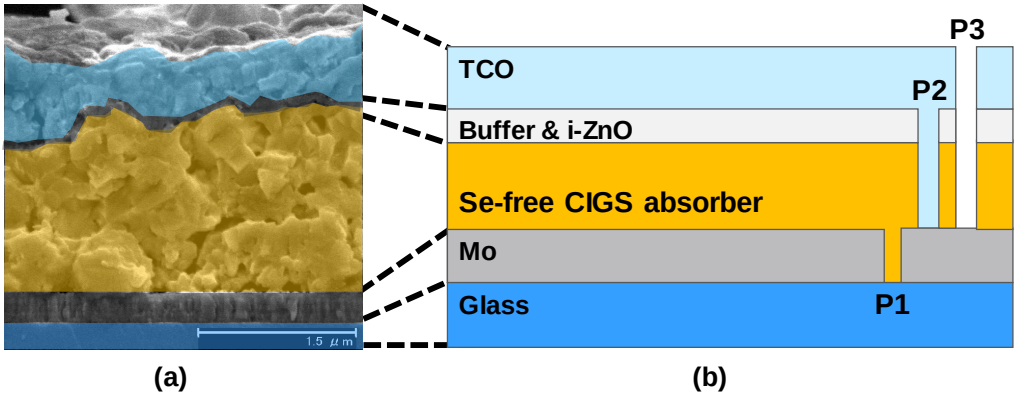

Fig. 7-3. (a) SEM image and (b) schematic of the cross section of the Se-free CIGS mini-module.

In Fig. 7-4, a photograph of a completed Se-free CIGS mini-module is shown, along with its *J*–*V* characteristics. The first mini-module demonstrated an *Eff* of 13.2% with a V_{oc} of 850 mV. Figure 7-5 shows a comparison of the *J*–*V* curves for a Se-free CIGS mini-module and a single cell that was fabricated from an identical absorber. The detailed electrical parameters for both devices are given in Table 7-I. The single cell demonstrated an *Eff* of 14.4% with a V_{oc} of 903 mV. A comparison between the mini-module and single cell indicated that the dominant issue for the mini-module was the considerably low V_{oc} and poor *FF* due to a low R_{sh}, which was assumed to have caused V_{oc} variation in each cell in the mini-module.

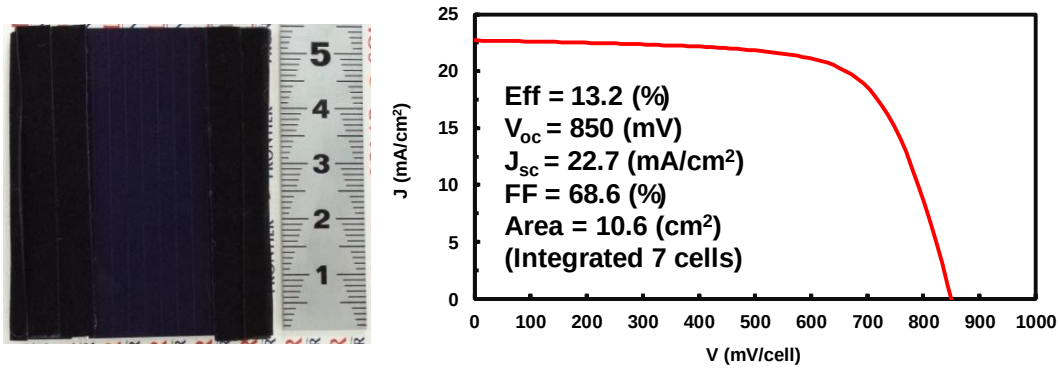

(a) **(b)**

Fig. 7-4. Comparison of the *J*–*V* curves in a Se-free CIGS mini-module and a single cell.

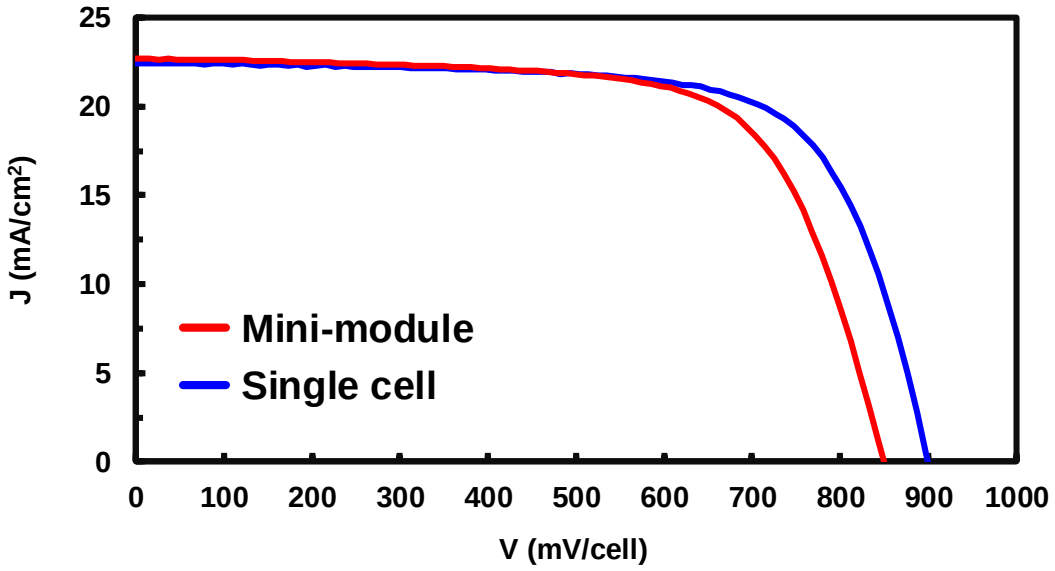

Fig. 7-5. Comparison of the *J–V* curves for a Se-free CIGS mini-module and a single cell.

Table 7-I. Electric parameters of the Se-free CIGS mini-module and a solar cell.

Sample	Eff (%)	V_{oc} (mV/cell)	J_{sc} (mA/cm^2)	FF (%)	Area (cm^2)
Mini-module	13.2	850	22.7	68.6	10.6
Single cell	14.4	903	22.6	70.7	0.521

To evaluate the uniformity of the large-area absorber and to investigate the problem responsible for the low performance of the mini-module compared with that of a single cell, the circuit uniformity of the Se-free CIGS mini-module was diagnosed through electroluminescence (EL) imaging with a charge-coupled device camera. The EL imaging technique is widely accepted as being a useful tool for analyzing solar modules [1-3]. EL mapping showed the light emission intensity distribution on the pure-sulfide CIGS submodule, as shown in Fig. 7-6 (b). The CdS buffer layer may have been non-uniform because of absorber roughness, as suggested by the SEM image as shown in

Fig. 7-3, which indicated high roughness of the Se-free CIGS absorber. This roughness presumably caused the degradation of the V_{oc} and *FF* due to a low R_{sh}.

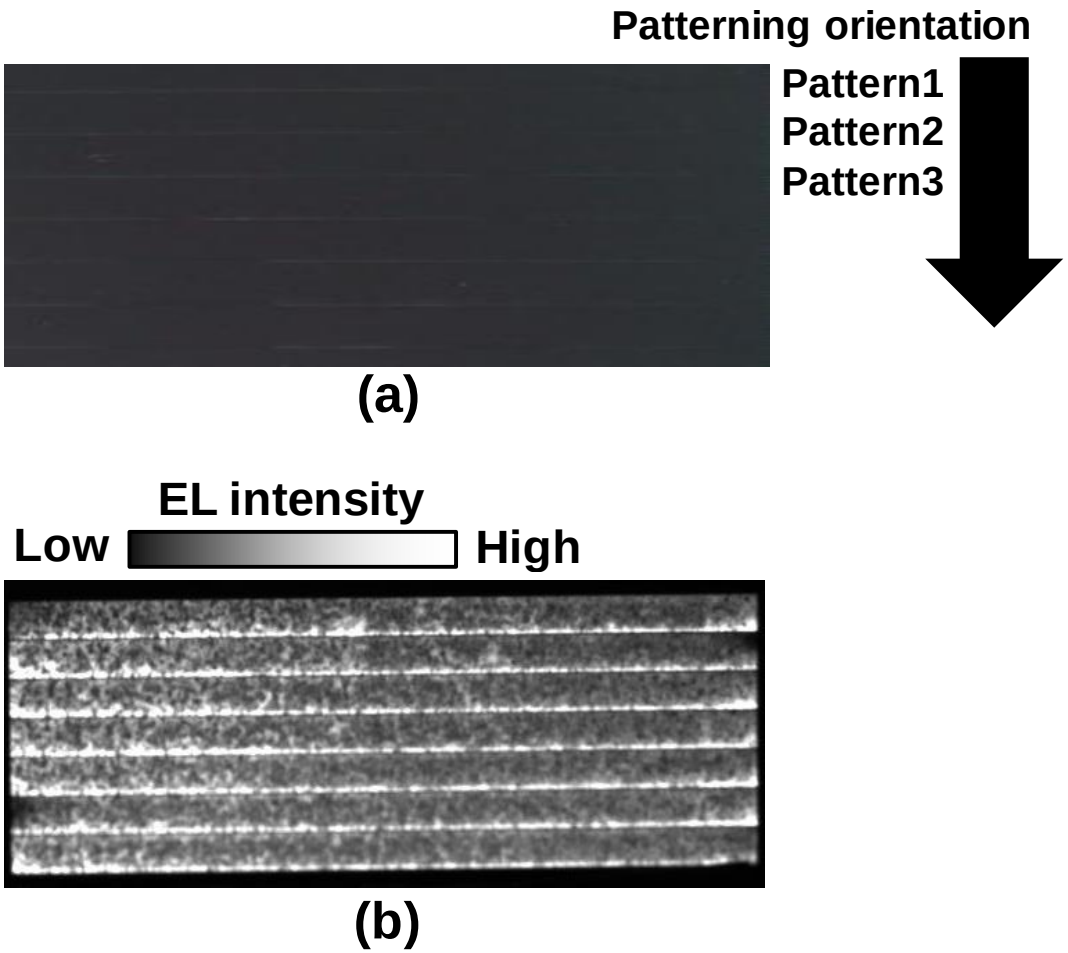

Fig. 7-6. (a) Photograph and (b) EL intensity image of the Se-free CIGS mini-module.

As with a single cell, a $Zn_{1-x}Mg_xO$ buffer layer was incorporated into a mini-module. With the exception of the buffer layer, the structure was mainly the same as that of the previously mentioned mini-module with a CdS buffer layer. Figure 7-7 shows (a) a schematic of the cross section and (b) the *J*–*V* characteristics of the Se-free CIGS mini-module with a $Zn_{1-x}Mg_xO$ buffer layer (aperture area of 10.6 cm^2 with integrated 7 cells). As a result, an *Eff* of 12.2% and a V_{oc} of 907 mV were achieved with the

$Zn_{1-x}Mg_xO$ buffer mini-module. Compared with the V_{oc} and J_{sc} of the CdS buffer mini-module, the V_{oc} and J_{sc} of $Zn_{1-x}Mg_xO$ buffer mini-module were enhanced; however, the *FF* was very low. The current $Zn_{1-x}Mg_xO$ buffer layer is still not suitable for use in mini-modules. Thus, modification and optimization of each layer in a Se-free CIGS mini-module are needed for further improvement of mini-module performance. On the basis of these results, numerous experiments to improve the *Eff* are being conducted through repetitive trial and error. In the near future, outstanding Se-free CIGS-based products will be introduced worldwide.

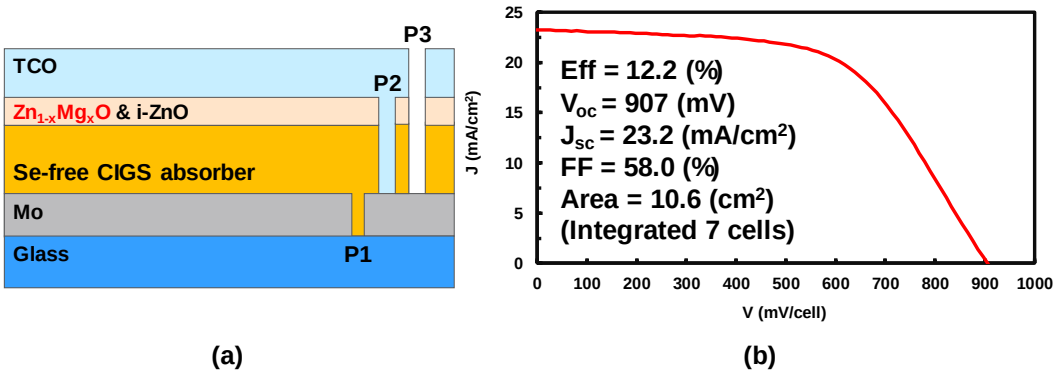

Fig. 7-7. (a) Schematic of the cross section and (b) *J-V* characteristic of a Se-free CIGS mini-module with a $Zn_{1-x}Mg_xO$ buffer layer (aperture area of 10.6 cm^2 with integrated 7 cells).

References

[1] F. J. Pern, F. Yan, L. Mansfield, S. Glynn, M. Rekow, R. Murison, *Proc., 43rd IEEE Photovoltaic Specialists Conference*, Seattle, USA (2017).

[2] U. Raw, T. Kirchartz, A. Helbig, B. E. Pieters, *Proc., Materials Research Society,* **1165** (2009) M03-04.

[3] T. Fuyuki, H. Kondo, T. Yamazaki, Y. Takahashi, Y. Uraoka, *Appl. Phys. Lett.* **86** (2005) 262108.

Appendix

Single-junction solar cells

The cell performance of a single-junction solar cell is evaluated on the basis of its conversion efficiency (*Eff*). The *Eff* of a solar cell depends on the bandgap (*Eg*) of an absorber layer because the transmission of photons with lower energy than the *Eg* of the absorber occurs. In addition, the energy generated by photon absorption by electron–hole pairs is released as thermal energy into the semiconductor lattice. Because of these two principal loss mechanisms, the *Eff* of solar cells is restricted, as shown in Fig. 1-6 [1]. Here, the *Eff* of solar cells is defined as follows:

$$Eff = \frac{P_{max}}{P_{in}} = \frac{J_{sc} \times V_{oc} \times FF}{P_{in}} \quad (1\text{-}1)$$

where P_{max} and P_{in} are the maximum power generated by a solar cell and the incident power, respectively. Additionally, J_{sc} and V_{oc} are the short-circuit current density and the open-circuit voltage, respectively. *FF* is the fill factor, which is given by

$$FF = \frac{J_{sc} \times V_{oc}}{J_{max} \times V_{max}} \quad (1\text{-}2)$$

where J_{max} and V_{max} are the current density and voltage at P_{max}, as shown in Fig. 1-7. The *FF* can be approximated empirically as follows:

$$FF = \frac{V_{oc} - log(V_{oc}+1)}{V_{oc}+1} \quad (1\text{-}3)$$

This equation means that the *FF* depends on the V_{oc}. Generally, the V_{oc} increases with increasing *Eg* because an increase of *Eg* increases the potential energy of generated

electrons. However, J_{sc} increases with decreasing *Eg* because a narrower *Eg* can absorb more photons. Thai is, J_{sc} and V_{oc} exhibit a trade-off relationship.

On the basis of the aforementioned physical and electrical characteristics of solar cells, in order to attain higher efficiency, deducing the best conditions that optimize each electrical parameter of a solar cell is important.

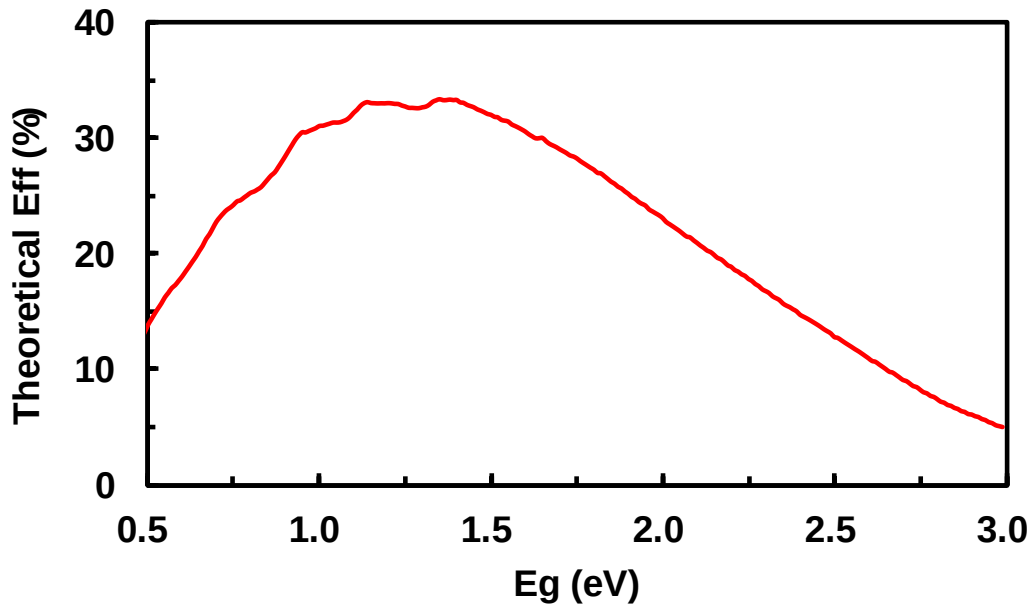

Fig. A-1. Dependence of the theoretical *Eff* of solar cells on *Eg*. (Referenced from "The Shockley-Queisser limit. [1]")

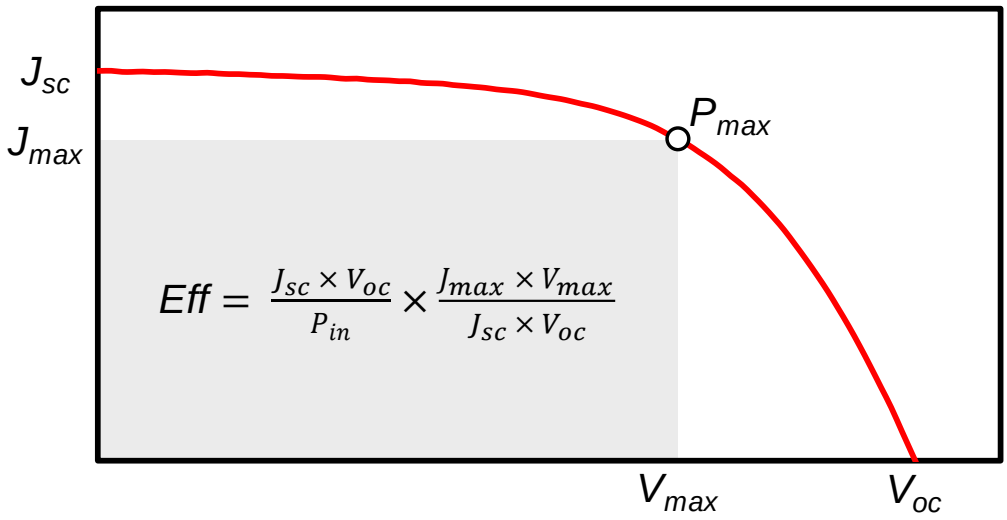

Fig. A-2. Conversion *Eff* of a solar cell (*J*–*V* curve).

References

[1] W. Shockley, H. J. Queisser, *J. Appl. Phys.* **32** (1961) 510-519.

Acknowledgements

The author would like to express deepest appreciation to Professor Akira Yamada, whose warm encouragement allowed the author to complete this study. His unfailing scientific judgment and leadership allowed me to find better solutions to the unexpected problems encountered in this research and provided me with the proper direction to proceed successfully with the study.

The author is indebted to Dr. Hiroki Sugimoto for his constant guidance, constructive advice, and critical comments throughout the study.

The author would like to express special gratitude to Associate Professor Shinsuke Miyajima for his invaluable advice and encouragement throughout the study.

The author is also grateful to Mr. Yasuaki Iwata and Ryo Matsumoto for his gracious technical support.

The author would like to thank his peers: Takeshi Umehara, Takahito Nishimura, Yuki Takiguchi, Adiyudha Sadono, Naoki Suyama, Kazuyoshi Nakada, Kanta Sugimoto, Souma Toki, Motoki Watanabe, and Tomohiro Ogiwara for kind advice and their encouragements.

The author would also like to thank all of the members of the Yamada and Miyajima Laboratory, especially the members of the CIGS thin film solar cell group.

Thanks are extended to secretaries Ms. Kimiko Furukawa and Ms. Eri Mikado for their kind assistance and encouragements.

This work was partly supported by Showa Shell Sekiyu K.K. and Solar Frontier K.K.

Finally, a special word of thanks must be given to my wife, Ayako Hiroi, father, Hiroomi Hiroi, and mother, Eiko Hiroi. Without their help, contribution, and encouragement, the

author could not have finished this doctoral thesis.

Thank you very much once again for all of the above.

Homare Hiroi

June 2017

List of publications

Papers

①**Homare Hiroi**, Yasuaki Iwata, Hiroki Sugimoto, Akira Yamada, *"Progress Toward 1000-mV Open-Circuit Voltage on Chalcopyrite Solar Cells," IEEE Journal of Photovoltaics*, **vol. 6,** no. 3 (2016) 1630-1634.

②**Homare Hiroi**, Yasuaki Iwata, Shunsuke Adachi, Hiroki Sugimoto, Akira Yamada, *"New World-Record Efficiency for Pure-Sulfide Cu(In,Ga)S_2 Thin-Film Solar Cell With Cd-Free Buffer Layer via KCN-Free Process," IEEE Journal of Photovoltaics*, **vol. 6,** no. 3 (2016) 760-763.

③**Homare Hiroi**, Yasuaki Iwata, Kyouhei Horiguchi, Hiroki Sugimoto, *"960-mV Open-Circuit Voltage Chalcopyrite Solar Cell," IEEE Journal of Photovoltaics*, **vol. 6**, no. 1, (2015) 309-312.

Think piece

①**廣井誉**, "セレンフリー硫化物系 CIGS 太陽電池", テクノロジートレンド, OITDA オプトニューズ Vol.12, No.2 (2017)

International conferences

①**(Invited) Homare Hiroi**, Akira Yamada, *"Over 16% Se-free Cu(In,Ga)S_2 solar cell,"* The 2017 European Materials Research Society Spring Meeting and Exhibit (The 2017 EMRS Spring Meeting), May. 2017.

②**(Invited) Homare Hiroi**, Yasuaki Iwata, Kyouhei Horiguchi, Hiroki Sugimoto, Akira Yamada, *"New Challenge in Se-free Cu(In,Ga)S_2 Solar Cells,"* The 26th International

Photovoltaic Science and Engineering Conference (PVSEC-26), Oct. 2016.

③**(Oral)** **Homare Hiroi**, Yasuaki Iwata, Hiroki Sugimoto, Akira Yamada. *"Investigation of Se-free (Ag,Cu)(In,Ga)S_2 solar cells,"* 20th International Conference on Ternary and Multinary Compounds (ICTMC-20), Sep. 2016.

④**(Oral)** **Homare Hiroi**, Yasuaki Iwata, Hiroki Sugimoto, Akira Yamada, *"Progress Toward 1000mV Open-Circuit Voltage on Chalcopyrite Solar Cells,"* 43rd IEEE Photovoltaic Specialists Conference (IEEE PVSC-43), Jun. 2016.

⑤**(Invited)** **Homare Hiroi**, Yasuaki Iwata, Hiroki Sugimoto, Akira Yamada, *"High efficiency pure-sulfide Cu(In,Ga)S_2 solar cells with Cd-free buffer layer,"* The 2016 European Materials Research Society Spring Meeting and Exhibit (The 2016 EMRS Spring Meeting), May. 2016.

⑥**(Oral)** **Homare Hiroi**, Yasuaki Iwata, Kyouhei Horiguchi, Noriyuki Sakai, Hiroki Sugimoto, *"15.2% efficiency on pure-sulfide $CuInGaS_2$ solar cell,"* The 26th International Photovoltaic Science and Engineering Conference (PVSEC-26) / Global Photovoltaic Conference (GPVC), Nov. 2015.

⑦**(Poster)** **Homare Hiroi**, Yasuaki Iwata, Shunsuke Adachi, Hiroki Sugimoto, *"High Open Circuit Voltage Pure Sulfide $CuInGaS_2$ Submodule,"* 31st European Photovoltaic Solar Energy Conference and Exhibition (EU PVSEC 2015), Sept. 2015.

Domestic conferences

①**（招待講演）** **廣井 誉**, "企業若手研究者によるパネルディスカッション", 第 14 回 「次世代の太陽光発電システム」シンポジウム（名古屋大学）, 2017 年 7 月.

②**（招待講演）** **廣井 誉,** 山田明, *"Se フリーCIGS 太陽電池の実用化に向けた研究,"* 第 1 回 フロンティア太陽電池セミナー（京都大学）, 2016 年 11 月.

③（招待講演） 廣井 誉, 岩田 恭彰, 杉本 広紀, 山田 明, *“セレンフリー Cu(In,Ga)S_2 薄膜太陽電池の変換効率改善,”* 第 77 回 応用物理学会秋季学術講演会, 2016 年 9 月.

④（招待講演） 廣井 誉, 山田明, “セレンフリーCIGS 太陽電池の現状と課題”, 第 45 回 太陽光発電プロジェクト講演会（宮崎大学）, 2016 年 8 月.

⑤（ポスター発表） 廣井 誉, 岩田 恭彰, 杉本 広紀, 山田 明, *“高速昇温硫化による Se フリーCu(In,Ga)S_2 薄膜太陽電池の変換効率改善,”* 第 13 回 「次世代の太陽光発電システム」シンポジウム, 2016 年 5 月.

⑥（口頭発表） 廣井 誉, 岩田 恭彰, 杉本 広紀, 山田 明, *“$Zn_{1-x}Mg_xO$ バッファー層による Cu(In,Ga)S_2 薄膜太陽電池の変換効率改善,”* 第 63 回 応用物理学会春季学術講演会, 2016 年 3 月.

⑦（招待講演） 廣井 誉, 山田明, *“Cu(In,Ga)S_2 薄膜太陽電池の研究開発,”* 第 6 回 「化合物薄膜太陽電池分科会」研究会, 2016 年 1 月.

Awards

①廣井 誉, 応用物理学会講演奨励賞, （応用物理学会）, 2016 年 9 月.

②廣井 誉, イノベイティブ PV 奨励賞, （日本学術振興会第 175 委員会）, 2016 年 5 月.